INNOWACYJNA GOSPODARKA
NARODOWA STRATEGIA SPÓJNOŚCI

UNIWERSYTET JAGIELLOŃSKI W KRAKOWIE

FNP
Fundacja na rzecz Nauki Polskiej

UNIA EUROPEJSKA
EUROPEJSKI FUNDUSZ ROZWOJU REGIONALNEGO

Investigation of Deuteron Disintegration

A doctoral dissertation submitted to the Faculty of Physics, Astronomy and Applied Computer Science of the Jagiellonian University
by

Ghanshyambhai Khatri

Thesis Promotor
Prof. dr hab. Stanisław Kistryn
Co-promotor
dr Izabela Ciepał

Kraków, September 1, 2015

Wydział Fizyki, Astronomii i Informatyki Stosowanej

Uniwersytet Jagielloński

Oświadczenie

Ja niżej podpisany *mgr Ghanshyambhai Khatri* doktorant (nr indeksu: 1096761) Wydziału Fizyki, Astronomii i Informatyki Stosowanej Uniwersytetu Jagiellońskiego oświadczam, że przedłożona przeze mnie rozprawa doktorska pt. "***Investigation of Deuteron Disintegration***" jest oryginalna i przedstawia wyniki badań wykonanych przeze mnie osobiście, pod kierunkiem Prof. dr hab. *Stanisława Kistryna*. Pracę napisałem samodzielnie.

Oświadczam, że moja rozprawa doktorska została opracowana zgodnie z Ustawą o prawie autorskim i prawach pokrewnych z dnia 4 lutego 1994 r. (Dziennik Ustaw 1994 nr 24 poz. 83 wraz z późniejszymi zmianami).

Jestem świadom, że niezgodność niniejszego oświadczenia z prawdą ujawniona w dowolnym czasie, niezależnie od skutków prawnych wynikających z ww. ustawy, może spowodować unieważnienie stopnia nabytego na podstawie tej rozprawy.

Kraków, dnia ....

podpis doktorant

Dedicated to my loving
parents

Abstract

The Kraków-Katowice-KVI Few-Body Collaboration has provided large database of the cross sections and analyzing powers in the sector of three-nucleon (3N) systems. In this work, taking a step forward into the system composed of four nucleons (4N), the experiment was performed with the BINA detector at KVI Groningen. The data were obtained in deuteron-deuteron collisions at 160 MeV energy. The data were firstly pre-analyzed, then the energy calibration, particle identification and track reconstructions procedures were performed. Various two- and three-body channels were identified. For the first time a detailed analysis of the data collected in the ball — the backward part of the BINA — was performed with respect to energy and angular resolution and detection efficiency. The three body $dd \rightarrow dpn$ breakup reaction was extensively studied in the forward part of BINA. The differential cross section of the breakup reactions were obtained within the quasi-free scattering (QFS) region for about 150 angular configurations. The results have been compared to the very first calculations based on the CDBonn+Δ potential in a single-scattering approximation (SSA). Shape of the cross-section distributions for ϕ_{dp}=160° and ϕ_{dp}=180° is quite well reproduced by the theoretical predictions. The results , significantly enriching the 4N database, are very important for the development of theoretical description of the 4N systems dynamics.

Streszczenie

Pomiary grupy Kraków-Katowice-KVI dostarczyły obszernej bazy danych przekrojów czynnych i zdolności analizujących w sektorze układów trójnukleonowych (3N). Niniejsza praca stanowi rozszerzenie tych badań na system złożony z czterech nukleonów (4N), opisując eksperyment przeprowadzony w laboratorium KVI Groningen z użyciem układu detekcyjnego BINA. Dane zostały zebrane dla zderzeń deuteron-deuteron przy energii 160 MeV. Po wstępnej preselekcji zdarzeń, wykonane zostały kalibracja energetyczna, identyfikacja cząstek oraz przygotowane zostały procedury służące rekonstrukcji trajektorii cząstek naładowanych w kanale wyjściowym. Zidentfikowane zostały różne 3- i 4-ciałowe kanały reakcji w zderzeniach deuteron-deuteron. W tym eksperymencie po raz pierwszy wykonana została kompleksowa analiza danych zarejestrowanych w detektorze Ball (rejestrującym cząstki rozproszone pod dużymi kątami) z uwzględnieniem wydajności detektora oraz jego energetycznej i kątowej zdolności rozdzielczej. Wyniki ilościowe otrzymano dla trzyciałowej reakcji rozszczepienia deuteronu $dd \rightarrow dpn$, której produkty były rejestrowane w przedniej części detektora BINA. Przekroje czynne na tę reakcję zostały uzyskane dla obszaru quasi-swobodnego rozpraszania, dla około 150 konfiguracji kinematycznych. Wyniki eksperymentalne zostały porównane z pionierskimi obliczeniami teoretycznymi bazującymi na potencjale CDBonn+Δ, w przybliżeniu jednokrotnego rozpraszania (Single Scattering Approximation, SSA). Kształt uzyskanych rozkładów przekroju czynnego dla ϕ_{dp}=160° oraz ϕ_{dp}=180° jest dobrze odtwarzany przez obliczenia teoretyczne. Wyniki te w znaczący sposób wzbogaciły bazę danych dla układów 4N, co jest niezwykle ważne dla rozwoju modeli teoretycznych opisujących dynamikę oddziaływania w układach 4N.

Contents

1 Introduction **6**

2 Theoretical background **11**
2.1 NN and 3N interactions 11
2.1.1 Realistic NN potentials 12
2.1.2 Chiral perturbation theory (ChPT) 13
2.1.3 Coupled-channel potentials (CCP) 14
2.2 4N interactions - a step forward 14
2.3 Reaction kinematics 16
2.3.1 Elastic and quasi-free (QFS) scattering 16
2.3.2 Three-body breakup 18
2.3.3 Transfer channels 20

3 Experiment **21**
3.1 AGOR cyclotron and beam lines 21
3.2 The BINA detector 21
3.2.1 Forward wall 24
3.2.2 Backward ball 27
3.2.3 Electronics 31
3.3 Target system 32
3.4 Beam intensity monitor 34

4 Data Analysis **35**
4.1 Framework 35
4.2 Pre-analysis of raw data and event selection 35
4.2.1 Time information 36
4.2.2 Track reconstruction 37
4.3 Particle identification 39
4.4 Energy calibration 40
4.4.1 Wall scintillators 40
4.4.2 Ball scintillators 45
4.5 Discrimination of reaction channels 51
4.6 Detector efficiency 53
4.6.1 MWPC efficiency 53
4.6.2 ΔE scintillators: 54
4.6.3 E scintillators: 55
4.6.4 Ball efficiency 56

4.7 Analysis of elastic scattering process 58
4.7.1 Background subtraction and calculation of normalization factor 58
4.7.2 Cross-section scaling 59
4.8 Breakup reaction analysis 61
4.8.1 Evaluation of breakup coincidences 61
4.8.2 Three-body breakup cross-section 63
4.9 Possible sources of uncertainty 64

5 Results and Discussion **70**

6 Summary, Conclusion and Outlook **74**

Appendix **74**

A List of ball elements **75**

B Formula for differential cross section **79**

C Breakup Cross Section Results **80**

Bibliography **88**

Acknowledgments **91**

Chapter 1

Introduction

The work presented in this thesis addresses one of the fundamental questions of physics, the nuclear forces that hold the protons and neutrons together in atomic nuclei. It has been a long-standing problem to understand the exact nature of nuclear forces. Yukawa, in 1934, gave an idea of how the force between two nucleons could look like [1]. He used the analogy of the Coulomb interactions where a quantum of electromagnetic radiation (photon) is exchanged between two charged particles, mediating the interaction between them. In case of the nuclear forces, there should also be a particle (boson) governing the short range nuclear interactions. Taking the internuclear distance r $\approx$ 2 *fm* he predicted the mass of such a particle about 200 times the mass of an electron. Having mass greater than electron but smaller than mass of a nucleon, Yukawa called it a "heavy quanta" or a "U-quanta". And the term "meson" was first used by an Indian physicist Bhabha [2]. After more than a decade, in 1947, Powell and his team discovered experimentally the heavy type of particles, predicted by Yukawa. These were called the pions [3].

After Yukawa's meson-exchange theory and discovery of pions, tremendous amount of efforts have been made to understand the force between two nucleon (2NF). The most basic properties of the nuclear forces have been explored via nucleon-nucleon (NN) and nucleon-deuteron (Nd) scattering experiments; these can be listed as (1) the nuclear force acts within a finite short range, (2) within this finite range it has an attractive and a repulsive part, (3) it is spin dependent, (4) contains non-central part (tensor forces), (5) almost independent of the electric charge, i.e. the nuclear force is of the comparable magnitude between neutron-neutron, neutron-proton and proton-proton pairs.

Later on it was realized that the nuclear force can include not only a pion but also heavier mesons and multiple pions. Work of Taketani et al. [4] showed that depending on the internuclear distance, the type of mesons involved in reaction can be different. At the range of about 2 *fm*, mainly the pions are involved. The intermediate range, between 0.7 - 2 *fm*, is governed by two-pions exchange and heavier mesons such as ρ. The smallest range below 0.7 *fm* can be due to even more heavier mesons such as ω and multi-meson exchange. Modern potential are, however, based on phenomenological description of the short-range part.

Various theoretical approaches have been developed to describe the exact form of NN interaction. Today there exist the so-called realistic potentials based on "meson exchange" theory, few of the most commonly used potentials are Nijmegen-I, Nijmegen-

II [5], Argonne-V18 (AV18) [6], and CDBonn [7]. However, it is important to note that the pion-nucleon coupling constant can not be predicted by these theories. The constant is extracted from the experimental NN scattering database, using phase-shift analysis. The coupling constants of the other mesons with nucleon are left as free parameters. Each of the above mentioned potentials have about 40 or so free parameters and in general the NN scattering observables obtained using different potential agree well with each other. The quality of obtained potentials is usually found with $\chi^2/d.o.f. \approx 1.$ when fitted to the NN scattering data.

Today, according to the standard model of the particle physics, the nuclear forces are understood as the residual of the strong interactions between the constituent quarks of a nucleon. In order to describe the strong interaction between quarks, the theoretical framework of quantum chromodynamics (QCD) is utilized, yet not directly applicable, at low energies, such as in this work, since the quarks are confined within hadrons. Therefore a new theoretical approach, called chiral perturbation theory (ChPT), has been introduced: the effective field theory, consistent with the symmetries of QCD, relevant for the low-energy NN interaction. The NN scattering observables calculated within ChPT are also of good quality and are comparable to those obtained using earlier mentioned meson-exchange potentials [10, 11].

All the above mentioned NN potentials are able to describe the interaction between two nucleons exactly, including the binding energy of a deuteron. The ultimate goal is to have theoretical description of the systems composed of a large number of nucleons - at the heart of which lies the basic NN potentials.

However all the NN potentials fail even to describe the simplest three-nucleon systems, e.g. nucleon-deuteron (Nd) scattering observables or the binding energy of triton

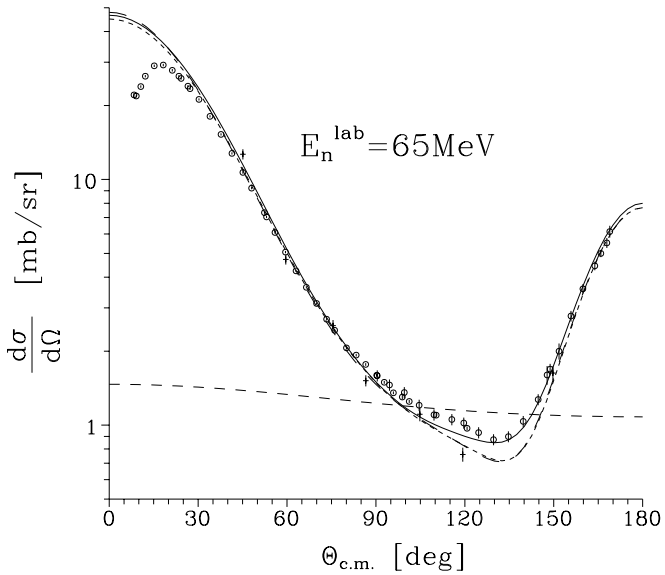

FIGURE 1.1: The Nd elastic cross section is presented in comparison with theoretical predictions. The long-dashed curve presents the calculation based on NN potential whereas the solid curve is the predictions based on NN potential combined with the 3NF effect. The short-dashed line presents the contribution of 3NF effect. Figure adapted from [8].

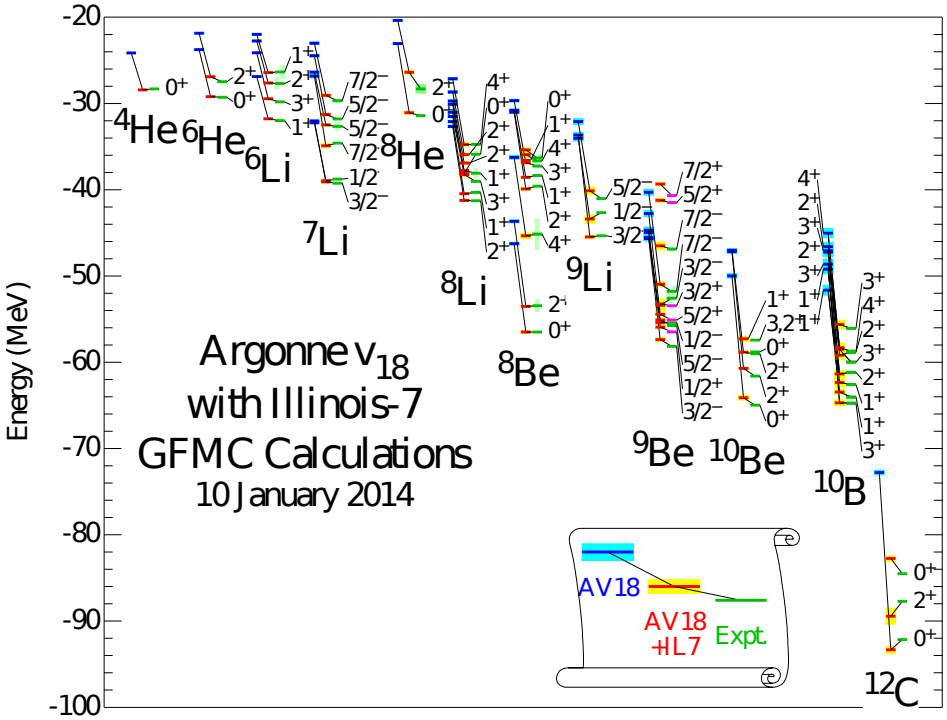

FIGURE 1.2: Experimental binding energies of light nuclei are compared using Green's function Monte Carlo calculations obtained with only a two-nucleon potential (AV18, blue/dark gray) and with the addition of a three-nucleon potential (IL7, yellow/light gray). Figure adapted from [9].

or ^{3}He. It was soon realized that there are still some dynamical ingredients missing in the theory - one of them is the so-called three-nucleon force (3NF) [12]. Adding 3NF brings the theoretical predictions closer to the experimentally determined Nd elastic cross section [8] (see Fig.1.1) as well as binding energies of light nuclei (see Fig.1.2). The 3NF comes into action when there are three or more nucleons but not when there are only two nucleons interacting. Existence of 3NF is due to the fact that the nucleons themselves are not point-like objects but having an internal structure, as they are made of the *up* and *down* quarks.

In fact the first 3NF, based on two-pion exchange, was already described by Fujita-Miyazawa in 1957 [12], see Fig. 1.3. However the 3NF became a hot-topic in the nuclear physics in last two decades. Various approaches (theoretical models) have been developed to account for the 3NF effects (see Section 2.1.1), which are used together with their compatible NN potentials. There are also other approaches to treat the 3NF in a consistent way with the 2NF; one is the ChPT which accounts for the 3NF via including higher order expansion terms in the calculations, and the other is so-called the explicit Δ-isobar excitation 3NF which is combined with CDBonn NN-potential.

The 3NF effect can be very subtle depending on the studied phase-space of the scattering kinematics. Therefore one needs a high precision data to trace it. The importance of 3NF effects in nucleon-deuteron elastic scattering was studied in detail in many experiments [13–28]. It turned out, that the complementary (to the elastic scattering) study of the deuteron breakup (N+d$\rightarrow$N+n+p) in collision with a nucleon allows to investigate the reaction dynamics with a great detail. The Kraków-Katowice-

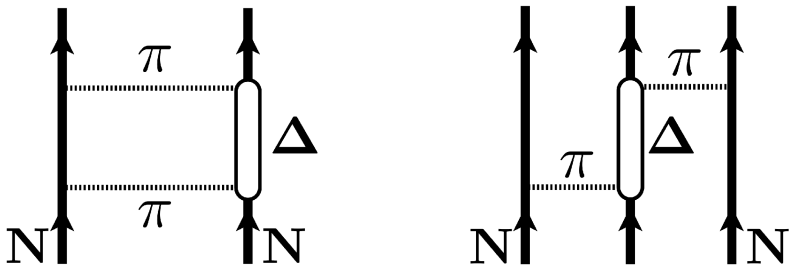

FIGURE 1.3: An illustration of two-pion exchange mechanism involving a virtual N→ Δ →N transition. Left: for two-nucleon, and Right: three-nucleon interaction. Figure adapted from [32]

KVI collaboration have provided a large sets of Nd scattering experimental data with a very high precision using the dedicated detection systems — namely SALAD and BINA detectors [29–31].

Adding 3NF improves the overall description of the data by the theoretical calculations, however, certain discrepancies remain, even in description of the differential cross section [33, 34]. In recent years, there have been attempts to resolve part of the discrepancies, mainly the relativistic [35–37] and the Coulomb effects [28,38]. However these two effects are encountered in a limited regions of the phase-space, the questions still remain whether we really understand the role of 3NF ? or are there other dynamical effects ?

This work is a continuation of the previous systematic studies of few-nucleon scattering by the Kraków-Katowice-KVI collaboration, with a step forward into larger system of four nucleons (4N). The present status of 4N studies is poor, theoretically as well as experimentally. All 4N data that exist are mostly at low energy (see Fig.1.4) in the dd elastic scattering domain [42, 43] and the database in breakup sector is scarce [44]. It is expected to have larger contribution of 3NF effect in 4N system than in the 3N systems. On the other hand, theoretically the 4N system is extremely difficult and challenging, both technically as well as computationally. Before the rigorous calculations available for the 4N system, one may compare the quasi-free scattering (QFS) data within $dd \rightarrow dpn$ breakup (neutron acting as a spectator) with the predictions for the dp elastic scattering [41].

The outline of the thesis is as following. In the Chapter 2, theoretical aspects of studies of a few-nucleon systems are presented briefly: approaches to describe NN and 3N interactions, the theoretical formalism including so-called Faddeev-Yakubowsky equation; current status of calculations for 4N systems and, finally kinematic relations for various reactions involved in the experiment. In the chapter 3, BINA experimental setup is described . The chapter 4 covers details of the data analysis of $dd \rightarrow dpn$ breakup reaction, starting from the preliminary analysis through various steps such as energy calibration, particle identification, cross section normalization to the final breakup cross section. The last chapter will be devoted to discussion of the obtained results and their comparison with the "QFS calculations".

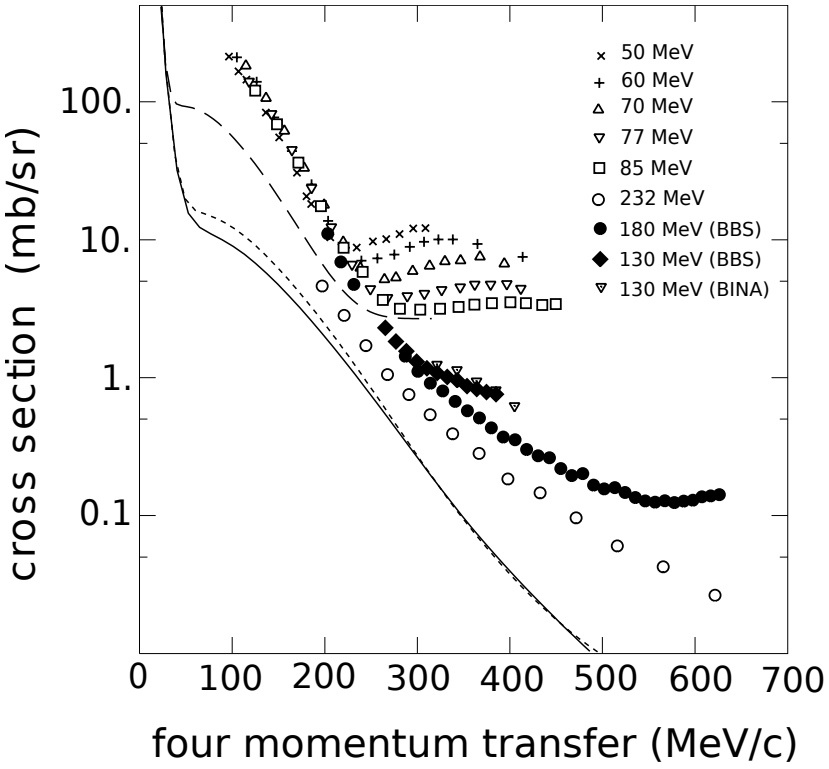

FIGURE 1.4: Cross section of dd elastic at various energies presented as a function of the four-momentum transfer. The data presented with empty circles are from IUCF [39]. The BBS data are from [40] and the BINA data are from [41]. Other data below 100 MeV are from Alderliesten [42]. The calculations from A. C. Fonseca were made at 231.8 MeV (solid), 191 MeV (short-dashed), and 52 MeV (long-dashed). Figure adapted from [40].

Chapter 2

Theoretical background

This chapter gives a very short overview of the tools to describe the quantum mechanical few-body (more precisely two, three and four nucleon) systems. Since the objective of the presented work is an *experimental investigation*, a comprehensive coverage of all the theoretical grounds is beyond the scope.

First, the theoretical tools to study the nucleon-nucleon (NN) and three-nucleon (3N) systems will be presented. This includes the Lippmann-Schwinger equation for the scattering problem and the Faddeev-formalism for exact treatment of the three-nucleon problems. It is followed by discussion of the existing realistic models of NN potential and three-nucleon force (3NF). Next, the recent progress towards the description of the four nucleon (4N) system is presented. The last section will be devoted to discuss kinematics of various outgoing channels in the dd collision in order to have an idea of what part of the phase space (and detector acceptance) is of interest for a particular final channel.

2.1 NN and 3N interactions

Interactions between subatomic particles, such as nucleons, are studied via the quantum mechanical scattering problem, with the aim to describe the cross-section of the scattering process, which is related directly to the transition operator (t). The t provides a link between a free asymptotic 2N state (i.e. free plane wave states in a wave packet at a large distance from the interaction point) and the 2N scattering state. The starting point is to look at the problem of a free particle, with initial quantum state $|\phi\rangle$ coming from an infinite distance in space to the vicinity of a potential V. The particle scatters due to the potential and continues to move away from V with a full scattering state $|\psi\rangle$. At large distances $|\psi\rangle$ has asymptotics of free incoming wave $|\phi\rangle$ + outgoing (scattered) spherical wave. The Lippmann-Schwinger (LS) equation is most extensively used tool to study such a problem, and it is given as follows [45]:

$$|\psi\rangle = |\phi\rangle + \frac{1}{E - H_0 + i\epsilon} V|\psi\rangle \tag{2.1}$$

where E is the energy and H_0 Hamiltonian of the incoming particle, and one takes limit $\epsilon \to +0$. One may formulate the LS equation in the form of transition operator, t, satisfying:

$$t = V + VG_0t \tag{2.2}$$

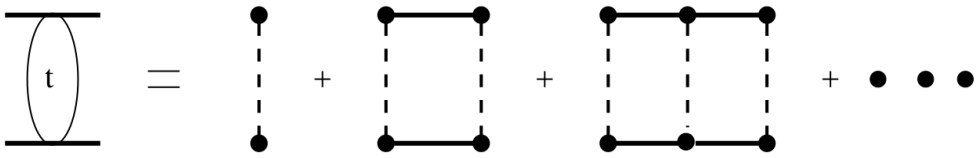

FIGURE 2.1: Visualization of the multiple scattering series presented in Eq. 2.4. The dashed lines shows the potential V and two horizontal solid lines are for the free propagator G_0 between two interaction. Figure adapted from [48].

where G_0 is the free propagator (or the Green's operator for the non-interacting system) and is given as follows:

$$G_0 = \frac{1}{E - H_0 + i\epsilon} \tag{2.3}$$

Note that t is a fundamental object for calculating scattering observables [45]. The above presented LS equations are formulated for NN scattering. However, for the case of three nucleons (3N), a different set of equations known as the Alt-Grassberger-Sandhas (AGS) equations are used — these are generalized form of the Faddeev equations [46, 47].

In Eq. 2.2 t is on both sides of the equation and can be self-substituted, the iteration will result in a so-called Born-series expansion as follows:

$$\begin{aligned} t &= V + VG_0(V + VG_0t) \\ &= V + VG_0V + VG_0VG_0V + VG_0VG_0VG_0V + \ldots \end{aligned} \tag{2.4}$$

Each term in Eq. 2.4 consist of a sequence of V and G_0, what is a general structure of interaction valid for any number of particles as presented in the Fig. 2.1. A further and detailed description of the theoretical tools can be found in references [45, 49, 50].

With the technical advancement in solving NN and 3N scattering problems and in availability of the computational power, it has became possible to exactly calculate the scattering observables in few-nucleon systems. The NN potential, input to the scattering theory of NN and 3N systems, is derived in three different approaches: (1) "the realistic potentials" — they are semi-phenomenological and are based on meson-exchange mechanism, (2) models which origin in Chiral perturbation theory (ChPT) — an equivalence of QCD for the low energy interaction, and (3) the coupled channel approach — where one induces Δ isobar excitation of the nucleons.

2.1.1 Realistic NN potentials

There exists many models of NN potential that can accurately describe the interaction between two nucleons — some of the most commonly used are the Nijm-I and Nijm-II [5], Charge-Dependent (CD) Bonn [7], Argonne-18 (AV18) [6]. The main difference between all these potentials lies in the method how they incorporate the off-shell behavior of the NN interactions. Note that all the NN potential models have about 45 free parameters that are fitted to high precision NN scattering data with reduced χ^2 close to 1, at the energy scale below pion production. In order to treat a 3N system, one needs to combine these NN potentials with the three-nucleon force (3NF) models, for example a 2π-exchange based 3NF, Tucson Melbourne-99 (TM99) model. It has a

cutoff parameter Λ_{TM} (in the units of pion mass m_π) which can be adjusted, for the NN potential, to reproduce the triton binding energy. There are also other models of 3NF, for example Urbana-IX [51] and Illinois [9] which are used in combination with the AV18 NN potential. An overview with a brief history of various models NN potential can be found in [52]. NN potentials in combination with the 3NF models, have also been used to perform an *ab initio* calculations to describe the properties of light nuclei [51, 53].

2.1.2 Chiral perturbation theory (ChPT)

The nuclear forces, according to the Standard Model, are understood as the residual of the strong interaction between quarks inside nucleons, and the associated dynamics is governed by quantum chromodynamics (QCD). However at low energy, the QCD becomes non-perturbative. In other words, due to confinement, the quarks and gluons are no longer the relevant degrees of freedom. In 1990, Weinberg suggested that an effective field theory (EFT), with nucleons and pions as the effective degrees of freedom, can be derived in such a way that terms in Lagrangian are consistent with the (broken) chiral symmetry (and in fact all the other symmetries) of QCD. This approach is known as ChPT. Applying the ChPT Lagrangian to NN scattering results in an infinite number of Feynmann diagrams. However, taking a systematic expansion in terms of $(\mathrm{Q}/\Lambda_\chi)^\nu$, — where Q is the typical momentum of the nucleons, $\Lambda_\chi \approx 1$ GeV is the chiral symmetry breaking scale, and $\nu \geq 0$ is the order of expansion — allows to point a finite number of diagrams at given order. One can describe the underlying interaction mechanism, schematically for each expansion order, via diagrams presented in Fig. 2.2. The detail description of ChPT can be found in references [54–57].

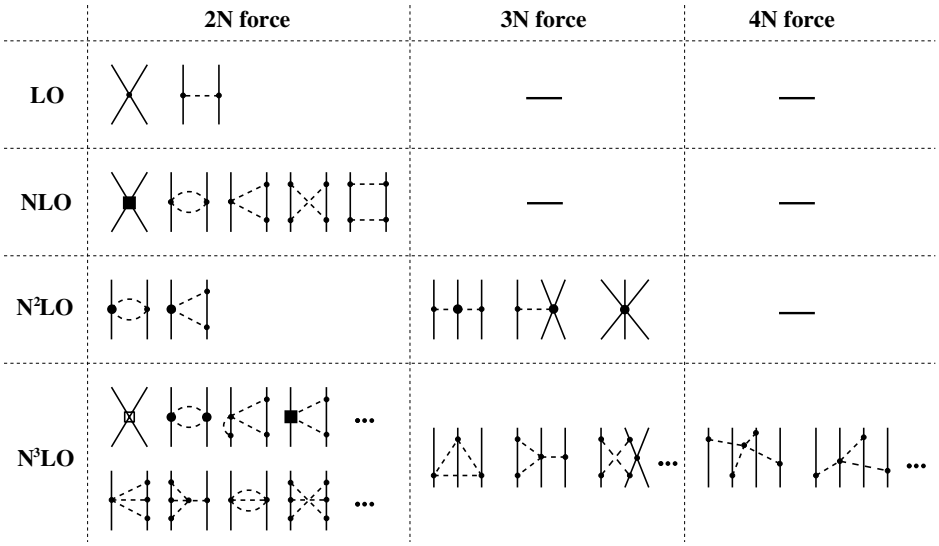

FIGURE 2.2: Hierarchy of nuclear forces in ChPT. Solid and dashed lines denote nucleons and pions, respectively. Solid dots, filled circles and filled squares refer, respectively, to the leading, subleading and sub-subleading vertexes in the effective Lagrangian. The crossed square denotes 2N contact interactions with 4 derivatives. Figure adapted from [29].

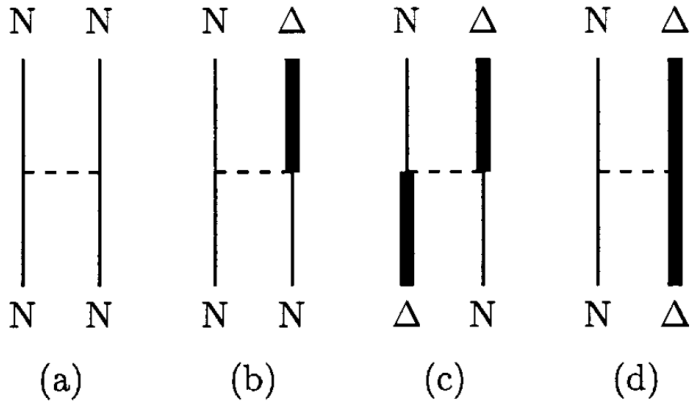

FIGURE 2.3: Two-baryon coupled-channel potential. A thin vertical line denotes a nucleon, a thick vertical line a Δ isobar, and a dashed horizontal line the meson exchange. Figure adapted from [58].

The Leading Order (LO) and Next-to-Leading Order (NLO) covers only the two nucleon (2N) force. As the order of expansion increases, the 3NF and 4NF emerge. Advantages of the ChPT are: (1) the 3NFs are derived and taken into account in a consistent way, i.e. they emerge naturally in higher order expansion and, (2) it allows a good control over systematic uncertainties of the predictions. Similar to the case of NN potentials, in ChPT also there are certain free parameters, known as the low energy constants (LECs) which values are taken from the π-N and NN scattering data. So far the ChPT allows to study 3N dynamics up to N^2LO.

2.1.3 Coupled-channel potentials (CCP)

The Lisbon-Hannover theory group have developed a coupled-channel potential by including a virtual Δ isobar excitation of a single nucleon in the CD Bonn NN potential [58], see Fig. 2.3. The Δ is considered as a stable baryon. This approach of NN interaction is valid for energy scale well below the pion production and it is based on exchange of all types of mesons, i.e. π, ρ, σ and ω. Similar to the ChPT approach, the advantage of CCP is that it treats the 3NF in consistent way along with the NN interaction via including the short-range (heavier mesons and multi-pion exchange). Within CCP approach, the Lisbon-Hannover group managed to include, for the first time, the (shielded) Coulomb interaction into the calculations of 3N systems [59]. The predictions obtained for the *dp* quasi-free scattering (QFS) withing the three-body $dd \rightarrow dpn$ breakup process are based on the CCP approach, see Chapter 5.

2.2 4N interactions - a step forward

As compared to the 3N systems, the 4N systems have richer structure. Study of 4N system opens possibility to study new dynamical effects such as four nucleon force (4NF), though the ChPT theory predicts a hierarchy as 2NF $\gg$ 3NF $\gg$ 4NF. On the other side, the effect of 3NF are predicted to be enhanced in 4N systems in comparison with the 3N system.

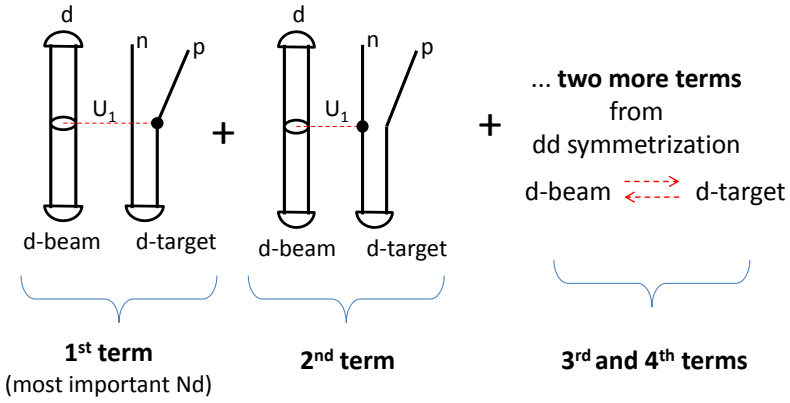

FIGURE 2.4: The $dd \rightarrow dpn$ breakup diagram under the Nd single-scattering approximation. The operator U_1 stands for the full Nd transition operator. Figure made from private communication with A. Deltuva.

Technically, the 4N system can be divided into two types of cluster, 2+2 and 3+1. The cluster of 3+1 can be further divided as (2+1)+1, thus in total it sums up with all possible permutations of the involved nucleons into 18 structures. This indicates that the problem of describing the 4N system interaction is even more difficult than the 3N system interactions, both technically as well as computationally. The mathematical tools to study the 4N interaction is the generalized form of the Faddeev formalism to the A≥4 number of particles, known as the Faddeev-Yakubowsky equations [60]. The exact treatment of the interaction in 4N system was not possible until now when the calculations at low energies became feasible [61–63]. Recently, the exact calculations were performed for two-body final channels in dd scattering at low energy, above the breakup threshold [64]. As one goes towards higher energy, such as the work described in this thesis, the number of partial waves needed for the convergence increases precluding so far to perform exact calculations. However, a simplified method can be applied for $dd \rightarrow dpn$ reaction near the so-called quasi-free (QFS) dp scattering.

Basing on the expectation that the Nd single-scattering approximation (SSA) may be reasonable near QFS conditions, a very first SSA calculations were prepared by A. Deltuva for the experiment described in this thesis [65]. The largest contribution to the dp QFS process was taken via *one-term calculation*, that is, the target deuteron breaks and its proton is undergoing all sorts of interactions (for example exchange of protons between p and d) with the beam deuteron, while its neutron is acting as a spectator, see 1^{st} term diagram in Fig. 2.4. Note that the CD Bonn + Δ potential was taken into the calculations with enough partial waves ($j_{2N} <= 5$, $j_{3N} <= 27/2$), however, without inclusion of Coulomb effects. The calculations were also performed by including all four terms (all 4 diagrams in Fig. 2.4), let's call it *four-term calculation* and the comparison of these two version of calculations, with the data, are presented in Ch. 5.

2.3 Reaction kinematics

In the deuteron-deuteron (dd) collision at energies below the pion production threshold, various channels can be identified on the basis of particle identification and kinematic relations. The possible reactions, with a pure hadronic signature, are as follows:

(1) d+d→d+d ... elastic scattering

(2) d+d→d+p+n ... three-body breakup

(3) d+d→d+p+$n_{spectator}$ ... breakup: quasi-free scattering (QFS) configuration

(4) d+d→^{3}H+p ... neutron transfer

(5) d+d→^{3}He+n ... proton transfer

(6) d+d→p+p+n+n ... four-body breakup

The first three channels are of a special interest for the presented work. In the case of the transfer channels, only the identification was performed with the purpose of future interest in a data analysis. The four-body breakup reaction $dd \rightarrow ppnn$ is out of the scope of this thesis and therefore will not be discussed. The kinematical relations for various channels of interest are discussed in the following subsections.

2.3.1 Elastic and quasi-free (QFS) scattering

In an elastic scattering process, the two colliding particles remain intact, but their momenta are changed. The momentum conservation requires that all the three momenta, one for the projectile ($\vec{p}_1$) and the other two for the final state ($\vec{p}_3$ and $\vec{p}_4$) are within a plane — resulting with a co-planarity condition formulated on the basis of

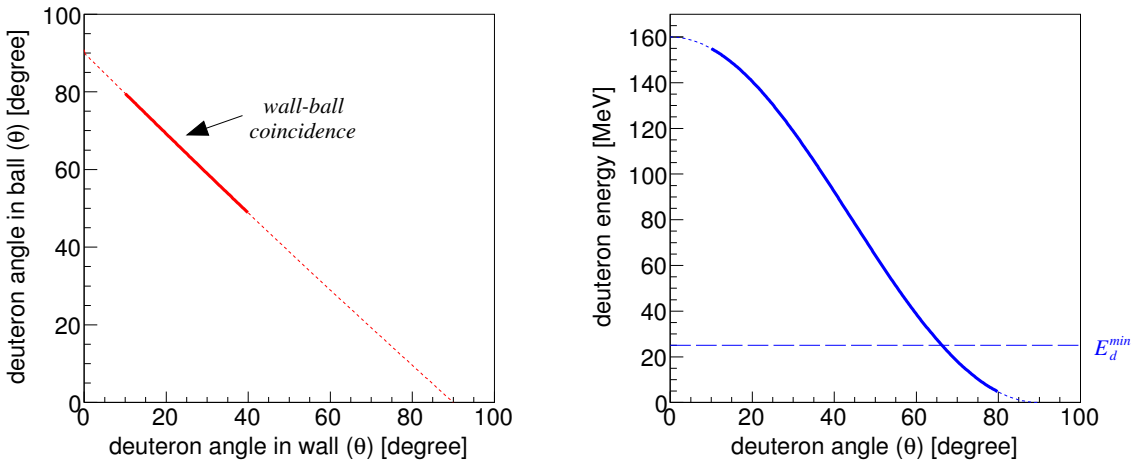

FIGURE 2.5: The kinematical relations of dd elastic scattering process; *left:* a relation between polar angles of the two outgoing deuterons, and *right:* kinetic energy of the deuteron versus it's polar angle. Part of the curves drawn as dashed line are out of the detector acceptance; the energy threshold for deuterons registered in wall, E_d^{min}, is also indicated.

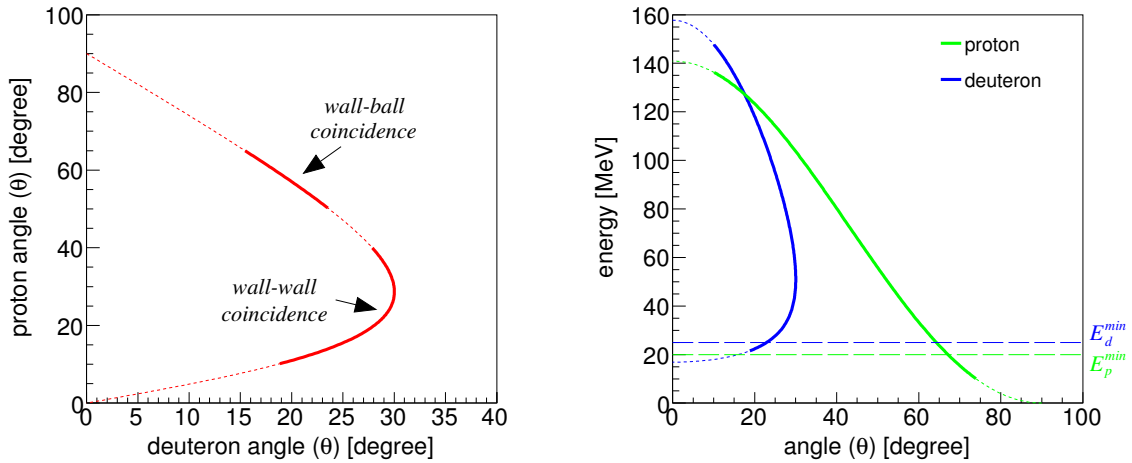

FIGURE 2.6: Kinematic relations of the dp elastic scattering at 157.7 MeV, description of the figures is analogous as in Fig. 2.5 except here both the scattered particles are possible to detect in the wall. The energy threshold for registering of the proton is also indicated.

the azimuthal ($\phi_{34} = \phi_3$ - $\phi_4 \equiv 180°$). The final state is described completely by one kinematic variable, for example E_3, E_4, θ_3 or θ_4: if only one particle is detected at a given polar angle (θ_3), the two-body kinematics determine strictly an angle (θ_4) of the second one as well as their kinetic energies. The calculated relativistic kinematical relations between scattering angles and the energies of the elastically scattered deuterons are presented in Fig. 2.5.

The quasi-free scattering (QFS) occurs when one of the colliding deuteron is scattered by the proton[1] of another deuteron while its' neutron is acting as a spectator [66]. The deuteron is a simplest bound state of nucleons with a very small binding energy (2.224 MeV), therefore with a beam energy of 160 MeV, the constituent nucleons of the colliding deuterons are seen as if they are free. The QFS process can be divided into two types; (i) the beam deuteron is scattered on proton of the deuteron target, let's call it *dp*-QFS, and (ii) the proton of the beam deuteron is scattered on deuteron target, let's call it *pd*-QFS. For the *dp*-QFS, the reaction energy will be about 157.7 MeV, while in the energy in the latter case will be about 77.7 MeV (about half the beam energy). For the present work, only the *dp*-QFS is considered for the cross section studies due to the kinematics and the forward wall acceptance. Fig. 2.6 shows the kinematical relations for the *dp*-QFS scattering in a situation when the neutron spectator is at rest in the laboratory frame.

Before the rigorous calculations of the observables become available for the 4N systems, the cross section data obtained for QFS can be compared with prediction based on *Nd* single scattering approximation (SSA), what makes the reaction very interesting and worth to study.

[1]Since the detection system allows to detect coincidences of two charged particles, QFS with proton acting as a spectator will not be discussed.

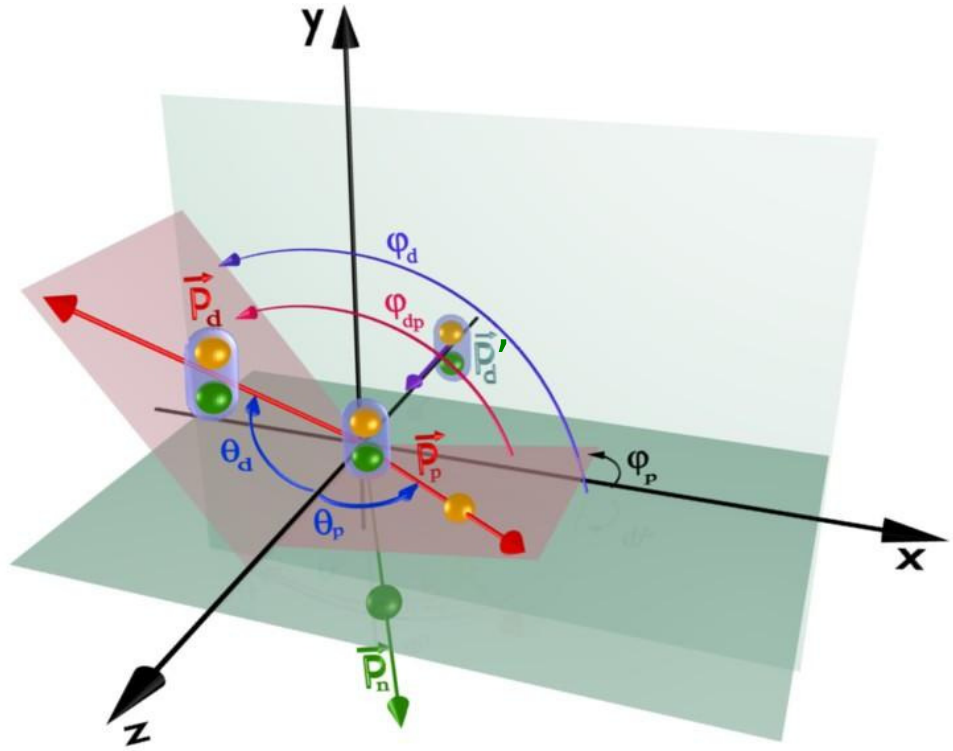

FIGURE 2.7: A schematic view of the breakup reaction with indicated momenta of the incoming deuteron ($\vec{p}_d'$) and of the three outgoing particles, the deuteron ($\vec{p}_d$), the proton ($\vec{p}_p$) and the neutron ($\vec{p}_n$). The polar (θ_d and θ_p) and azimuthal (ϕ_d and ϕ_p) angles of the two detected charged particles are defined in the chosen reference frame, as well as their relative angle ϕ_{dp} = ϕ_d - ϕ_p.

2.3.2 Three-body breakup

The $dd \rightarrow dpn$ breakup kinematics, with three free particles in the final state, offers opportunity to explore the phase-space more selectively to study and pin-down various dynamical effects of the underlying nuclear forces. The three particles can be described completely with 9 variables, namely the polar θ_i and azimuthal angles ϕ_i as well as their energies E_i, with i being d, p and n. The scattering angles are defined in Fig. 2.7. To be in consistent, the subscript "d"("p") will be assigned to describe the deuteron's (proton's) angles and energy. The energy and momentum conservation laws for the breakup reaction are given by the following equations;

$$\begin{aligned} E_0 &= E_d + E_p + E_n - Q, \\ \vec{p}_0 &= \vec{p}_d + \vec{p}_p + \vec{p}_n \end{aligned} \tag{2.5}$$

where, E_0 ($\vec{p}_0$) denotes the kinetic energy (momentum) of the deuteron projectile, E_d, E_p and E_n ($\vec{p}_d$, $\vec{p}_p$ and $\vec{p}_n$) refers to the kinetic energies (momenta) of the three outgoing particles, deuteron, proton and neutron respectively, and the Q-value (energy released) is the binding energy of deuteron, indicated as Q = -2.224 MeV. In the case of unpolarized particles, the system has, in addition, an axial symmetry. The BINA

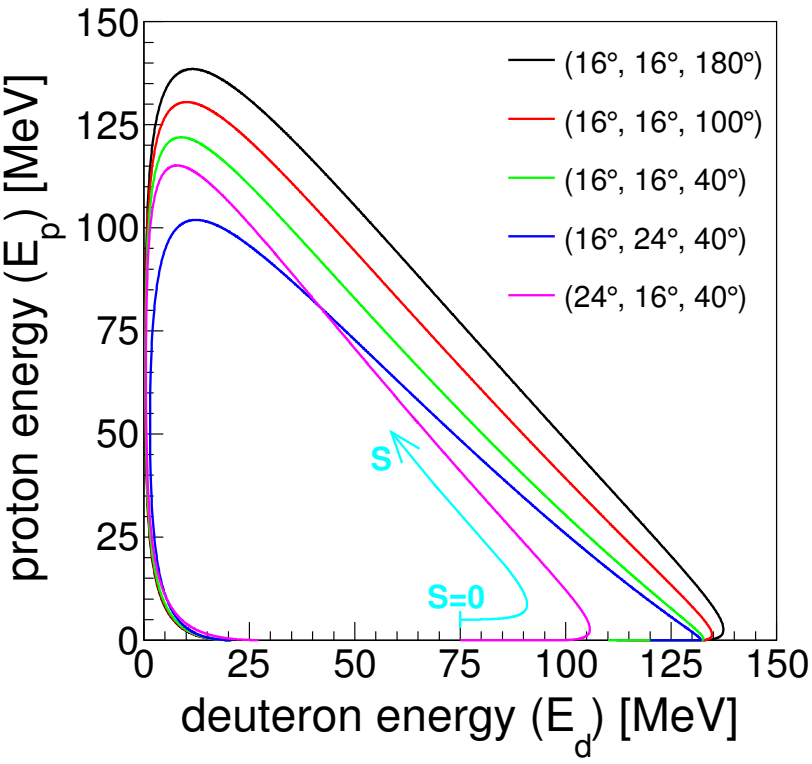

FIGURE 2.8: Sample set of kinematical relations: energy of proton versus energy of deuteron for different combinations of configurations (θ_d, θ_p, ϕ_{dp}), as indicated in the legend, are presented. The starting point S=0 (at the minimum of E_p) is indicated, with the direction of arrow indicating increase of S-value (arc-length) along the kinematics.

detector allows one to detect scattering angles and energies of charged particles. If one takes into account the above conservation laws, and additionally a relation $\phi_{dp} = \phi_d$ - ϕ_p, the variables θ_n, ϕ_n and E_n of the neutron can be eliminated. The three-body final state is then described by the kinematical variables of the deuteron and proton. The number of independent variables reduces to the following five: E_d, E_p, θ_d, θ_p and ϕ_{dp}, while E_d and E_p are not really independent, see below. Relation between these variables (in the non-relativistic framework) is given as follows [67]:

$$\begin{aligned}(m_d + m_n)E_d + (m_p + m_n)E_p - 2\sqrt{m_0 m_d E_0 E_d}\cos\theta_d - 2\sqrt{m_0 m_p E_0 E_p}\cos\theta_p \\ +2\sqrt{m_d m_p E_d E_p}\cos\theta_{dp} = m_n Q + (m_n - m_0)E_0,\end{aligned} \tag{2.6}$$

where:
$\cos\theta_{dp} = \cos\theta_d \cos\theta_p + \sin\theta_d \sin\theta_p \cos(\phi_d - \phi_p)$,
m_0, m_d are the deuteron masses,
m_p is the proton mass,
m_n is the neutron mass.
If one assumes $m_0 = m_d \equiv 2m$ and $m_p = m_n \equiv m$, Eq. 2.6 simplifies to:

$$\frac{3}{2}E_d + E_p - \sqrt{E_0 E_d}\cos\theta_d - \sqrt{2E_0 E_p}\cos\theta_p + \sqrt{2E_d E_p}\cos\theta_{dp} = \frac{Q - E_0}{2} \tag{2.7}$$

The above equation represents a 5 dimensional surface (called phase-space) in the 9-dimensional momentum space. For a chosen angular configuration — defined by two polar angles θ_d, θ_p and a relative azimuthal ϕ_{dp} angle— the relation between E_d and E_p describes a so-called "kinematical curve". Examples of a few kinematical relations are presented in Fig. 2.8. The S-variable indicates the arc-length along the kinematics and is expressed in the energy units. A point corresponding to S=0 is chosen arbitrarily at the minima of E_d or E_p, in this work we choose the notation with S=0 at the minima of E_p. Note that the QFS process, mentioned in the previous section, is in fact a limiting case of the three-body breakup process, where the energy of the 3^{rd} particle (here neutron) is set to be minimum [66, 68].

2.3.3 Transfer channels

In this process, a nucleon is transferred between the projectile and the target. This accounts for two different possibilities, the proton transfer channel (d+d→n+^3He) and the neutron transfer channel (d+d→p+^3H). The processes are described by the two-body kinematics. The kinematical relations for the transfer channels are nearly the same and therefore only one (for the neutron transfer channel) is presented in the Fig. 2.9. Having twice the electric charge as compared to the triton (and of course

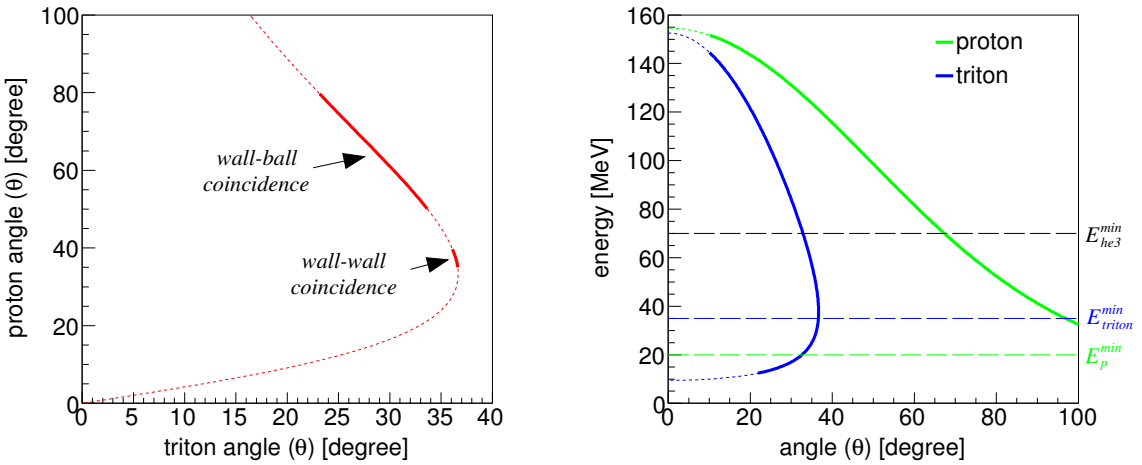

FIGURE 2.9: The kinematical relations for the neutron transfer reaction; *left:* a relation between the polar angles of the two outgoing particles, and *right:* the kinetic energy of the particles is presented as a function of their polar angles. The proton transfer channel is not much different and therefore one can refer to this one for both the transfer channels.

almost the same atomic mass), the ^3He particles would loose about twice as much energy as triton while traversing from target to the E-detector. Therefore the energy threshold in wall is about 35 MeV and 70 MeV for ^3H and ^3He respectively.

Chapter 3

Experiment

The experiment was carried out in April-2011 at Kernfysisch Versneller Instituut[1] (KVI) in Groningen, the Netherelands. The deuteron beam was provided by the superconducting cyclotron AGOR (**A**ccelerator **G**roningen **OR**say) at kinetic energy of 160 MeV and was impinging on a liquid Hydrogen (LH_2) and liquid Deuteron (LD_2) targets. A low beam current (about 5 pA) was used in order to keep the level of accidental coincidences possibly low. The reaction products were detected using **B**ig **I**nstrument for **N**uclear Polarization **A**nalysis (BINA) [69] which inherits a lot of features from its predecessor, the **S**mall-**A**ngle **L**arge-**A**cceptance **D**etector (SALAD) [70]. The BINA detector was designed to study few-body scattering reactions at medium energies.

In this chapter the most important instruments are described which have been used in the experiment.

3.1 AGOR cyclotron and beam lines

Fig. 3.1 presents a floor plan of the experimental area including the AGOR cyclotron and the experimental setups. Technical details of the AGOR cyclotron can be found in the references [68, 71].

For the presented work, the beam of 160 MeV deuterons was focused to a 1 mm spot on a liquid deuterium target (LD_2). The beam which passed through the target without interaction was stopped in a beam dump coupled with the Faraday Cup (FC) for beam current measurement.

3.2 The BINA detector

The BINA detector was assembled in 2004, as a result of collaboration between KVI and Vrije Universiteit Amsterdam [69]. During the period of 2005-2011, in collaboration of KVI with Polish physicists, it provided a large sets of data to study few-body nuclear physics. In 2012, BINA was transported to the Cyclotron Center Bronowice (CCB) in Krakow, Poland, and was successfully put into operation. The BINA setup allows to register coincidences of two-charged particles in nearly 4π solid angle, making possible to study almost full phase-space of breakup and elastic reactions. The detector is

[1]Now known as KVI-CART, Center for Advanced Radiation Technology

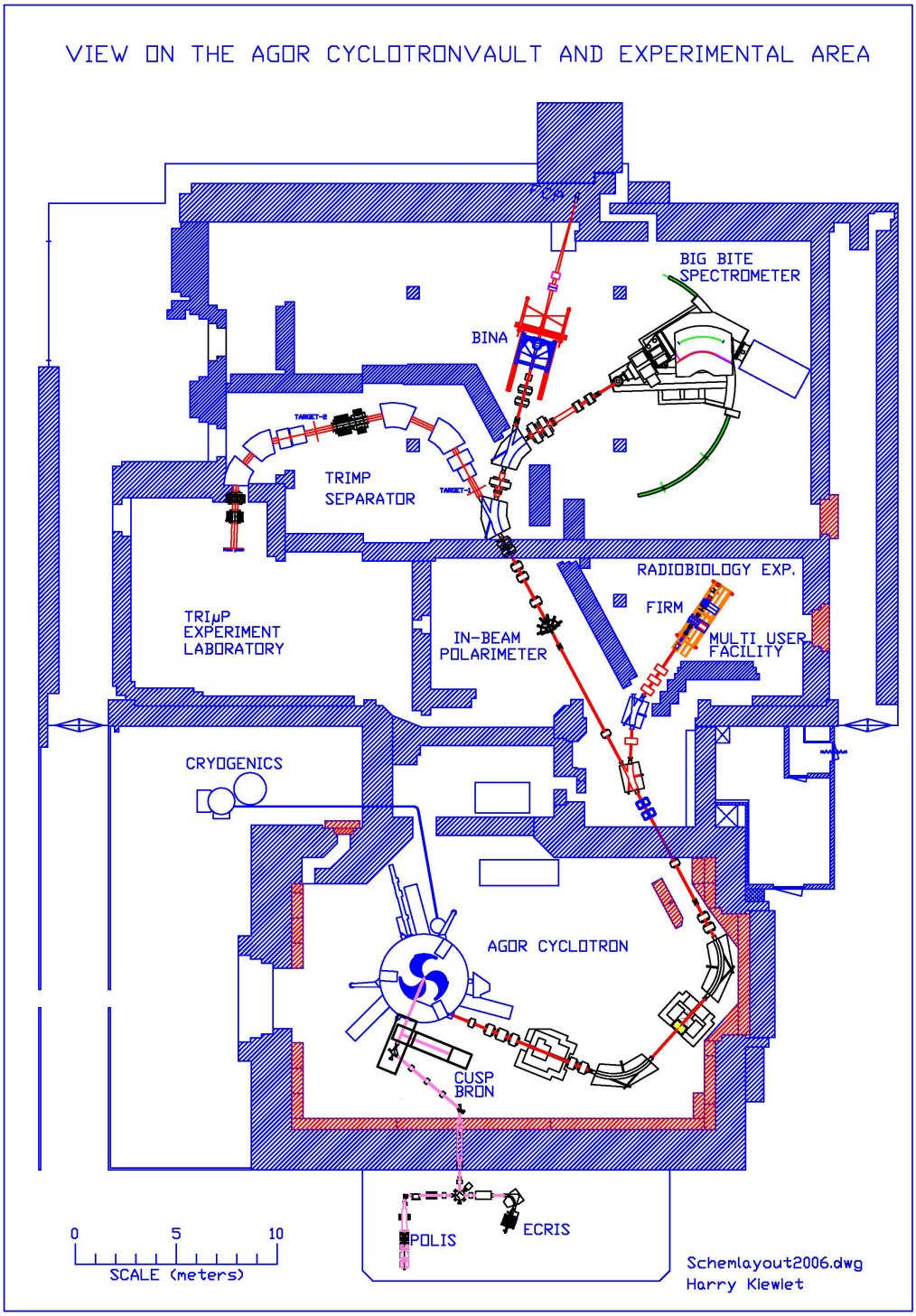

FIGURE 3.1: Floor plan of the cyclotron vault and the experimental areas. The AGOR cyclotron, beam line with analyzing magnets, and in the top area the BINA detector and the Big Bite Spectrometer are presented.

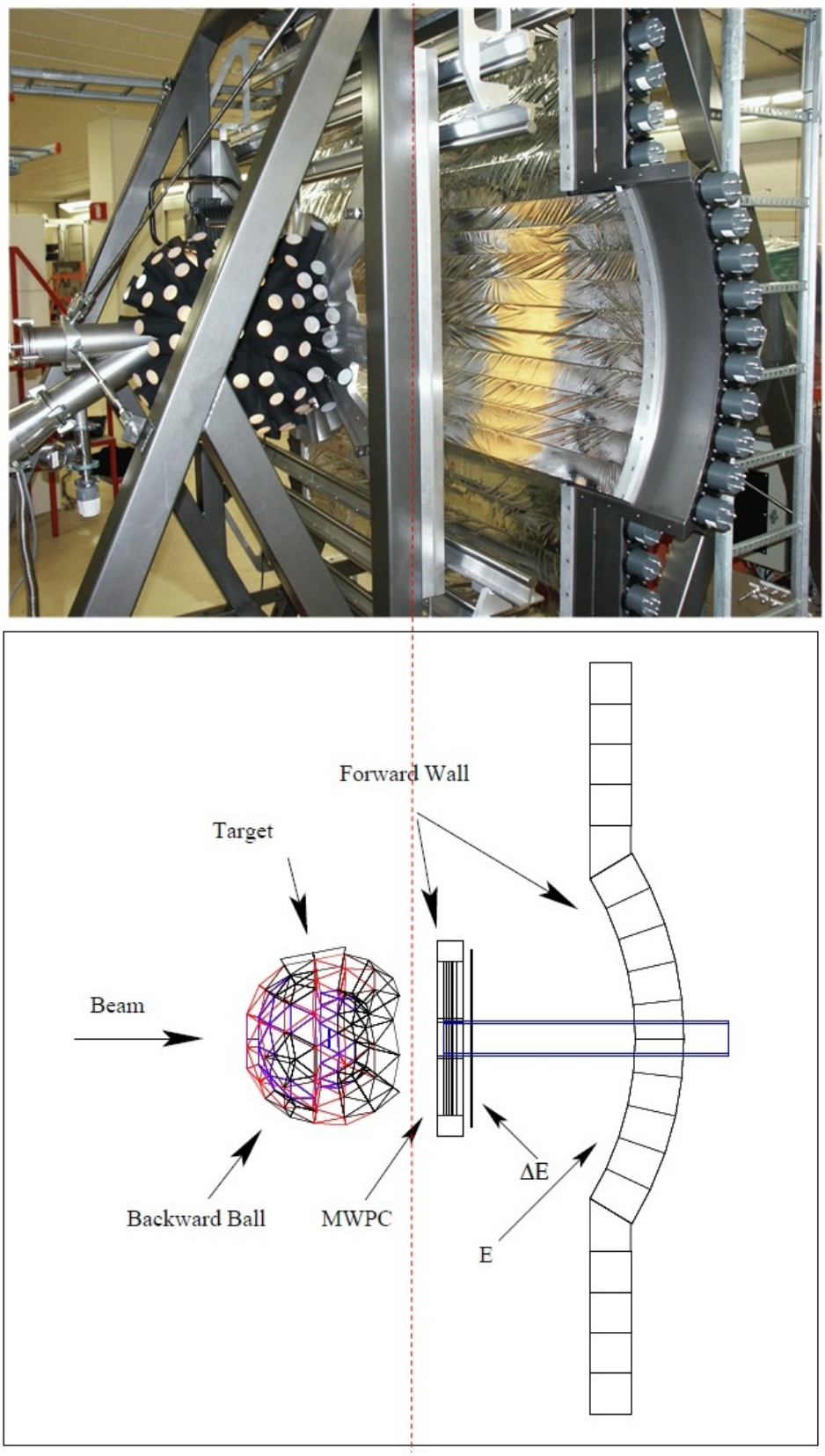

FIGURE 3.2: A side view of BINA. The top panel shows a photograph of BINA side-view and the bottom one presents schematic drawing of the forward wall and the backward ball.

divided into two main parts, the forward wall and the backward ball, see Fig. 3.2. Each of the detector parts are briefly described in following subsections.

3.2.1 Forward wall

The forward wall is composed of a three-plane multi-wire proportional chamber (MWPC) and telescopes formed by two crossed layers of scintillator hodoscopes (vertically placed thin transmission-ΔE strips and horizontally placed thick stopping-E bars). The forward wall allows to detect a charged particle scattered in the forward direction with a polar angle (θ) in the range of $10° - 32°$ with full azimuthal angle (ϕ) coverage, and extending this range up to $\theta = 37°$ with partial azimuthal angle coverage (due to corners of square-shape active region of the MWPC). A forward-scattered charged particle, passes through the MWPC — allowing a precise angular reconstruction, then it passes through the transmission-ΔE detector — where it leaves a small fraction of it's energy and, finally, the particle is stopped in the E-detector loosing all it's remaining energy. Both, the MWPC and the hodoscopes, have a central hole to allow for the passage of beam particles to the beam dump. Below the detectors are described in more details.

Multi-Wire Proportional Chamber: The MWPC is used for reconstruction of the emission angle of a charged particle produced in the target and flying in the forward

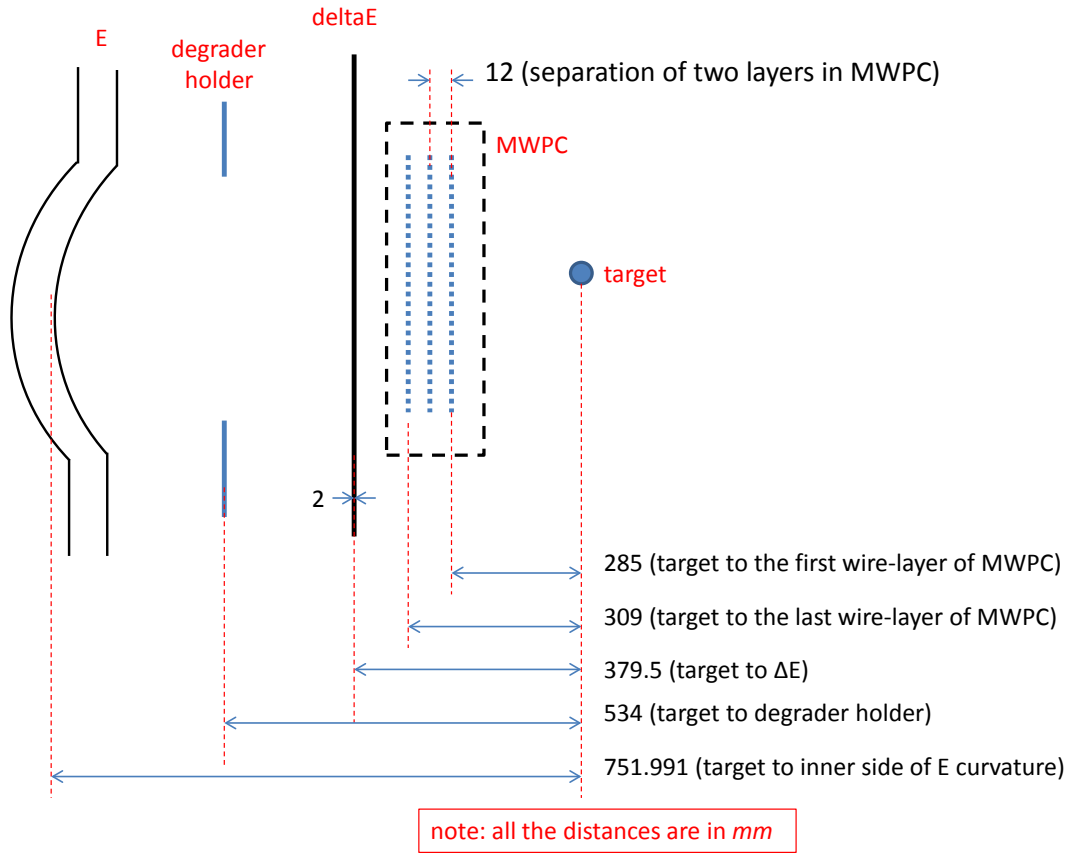

FIGURE 3.3: Dimensions and distances between various wall components and their distances from the geometrical center of target (ideally the reaction point). The picture is not to scale.

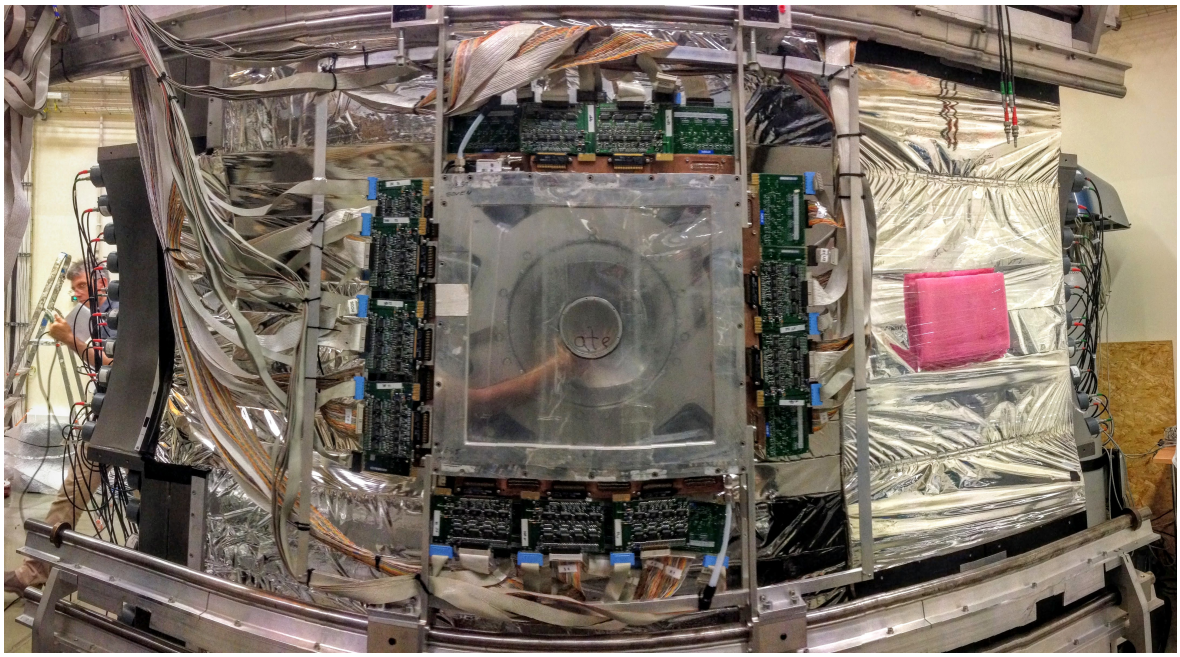

FIGURE 3.4: A panoramic photograph taken from the target location. The MWPC together with it's electronic cards (amplifier and discriminator) mounted on it, are visible in the center. The ΔE is visible (temporarily shifted out of its nominal position) on the right hand side of the picture. E-detectors are visible on the left side, behind MWPC cables.

region. It is installed at a distance of 29.5 cm from the target position and has an active area of 38×38 cm^2. The chamber consists of 3 planes, X, Y, and U, which are parallel arrays of equally-spaced (2 mm distance between any two adjacent wires) anode wires to readout the positions of the scattered particles. The anode wire planes are sandwiched between two parallel cathode frames, made of sprayed-graphite coated mylar foils with thickness of 25 μm, that are connected to a high voltage of -3150 V. The distance between two adjacent wire planes is about 12 mm. For details, see Fig. 3.3. With such an arrangement, the reaction is seen as almost point-like from the MWPC planes, allowing reconstruction of emission angles with a precision as high as 0.5°.

There are 236 parallel horizontally (vertically) placed wires in Y (X) plane, wheras the U plane contains total of 296 wires placed diagonally at an angle of 45° with respect to the former ones. The X and Y planes allow one to calculate the spatial co-ordinates of a detected charged particle whereas the U plane helps to reduce ambiguities in the reconstructed co-ordinates. An electro-negative gas mixture (80% of CF4 and 20% of isobutane), with a pressure of about 2-3 mbar, was utilized to operate the wire chamber. When a charged particle passes through the active area of the chamber, it ionizes the gas and as a consequence, the wires in the detection region produces a signal of detection. The engineering details of the MWPC and it's operational properties can be found in the reference [72].

The ΔE-E telescopes: The hodoscope is composed of two layers of plastic scintillator arrays, the ΔE and the E. The ΔE array is made of vertically placed thin plastic strips with the dimension of 0.2×3.17×43.4 cm^3 each. The E array is made of 20 horizontally placed thick bars, out of which the central 10 E-bars were used during

the experiment presented in this work. Each of the central E-bars has trapezoidal cross-section and the dimension of (9-10)×12×220 cm^3. They form together a part of a cylinder whose center coincides with the geometrical center of the target. The cylindrical shape reduces the so-called "cross-over events" (particle passing through two adjacent bars). The rest of the 10 E-bars, placed above and below the central cylindrical array, form a symmetric flat wing-like array with each bar in rectangle-cubic shape and a dimension of 12×12×220 cm^3. The latter can be used for detecting the secondary scattered particle for polarization-transfer experiment (not used in the present work).

Both, the ΔE and the E hodoscopes are made of BICRON-408 plastic scintillator material. The physical constants of the material are given in Tab. 3.1. The E-detector is thick enough (12 cm) to stop protons (deuterons) with energy below 140 MeV (180 MeV). On the other hand, due to different energy losses in materials between the target and the E-detector, the protons (deuterons) with initial energy below 20 MeV (25 MeV) will not reach the E-detector.

Each scintillator of the BINA setup is supplied with two photo-multiplier tubes (PMTs) at each ends of it via a light-guide. In case of an E-bar, the signals produced by two PMTs (when a charged particle is detected) are correlated. This correlation allows to detect the hit position of a detected particles — including neutrons, however with a very low efficiency compared to the charged particles. In the case of the ΔE-strips, no such correlation between PMT-signals was possible, because each ΔE-strip was cut into two in the middle of it's length. An exponential correction of the obtained ADC signal of ΔE was applied to compensate for the light attenuation along it's length. This improved the ΔE-E spectrum for the particle identification purpose. The Fig. 3.5 shows the individual segments (or telescopes) of the ΔE-E hodoscope with their polar angular coverage.

The energy deposited by a particle in ΔE depends on it's type (charge and mass) and it's incident energy. Therefore, when the ΔE and E signals, from a given scattered particle, are combined, it allows to identify the particle type (i.e. proton, deuteron, triton etc.) as well as to measure it's total energy.

BICRON model	Decay (ns)	λ_{max} (nm)	L_t (cm)	H/C ratio	ρ (g/cm^3)	n_c
BC-408	2.1	425	380	1.104	1.032	1.58
BC-444	180	428	180	1.109	1.032	1.58

TABLE 3.1: The physical constants of BICRON plastics. Here, L_t is the light attenuation length, λ_{max} is the peak wavelength of the generated light, H/C is the hydrogen-to-carbon ratio in the chemical composition of the plastic, ρ is the density of material and n_c is the refractive index.

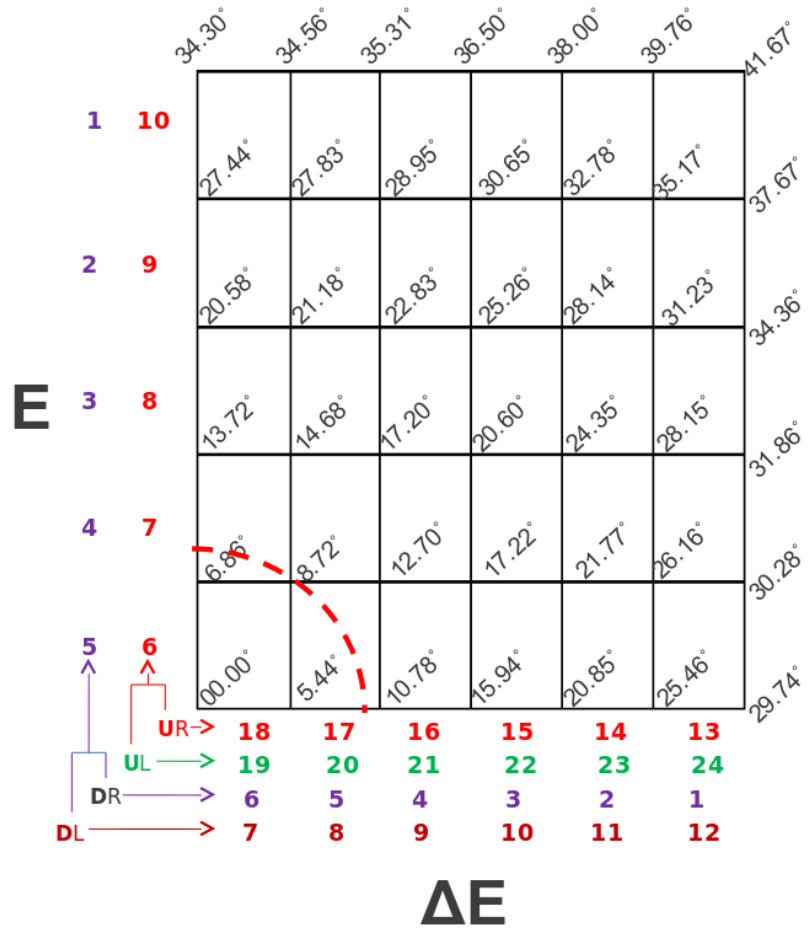

FIGURE 3.5: The segmented view of a quarter of the hodoscope. The calculated polar angular range for each telescope are also shown as well. A dashed-line arc presents the beam-pipe shadow (central hole). The short letters U, D, L and R stand for *up*, *down*, *left* and *right*, respectively to indicate location of a telescope on the hodoscop.

3.2.2 Backward ball

The backward ball is made out of 149 phoswich[2] elements. It is capable of detecting charged particles scattered with polar angle θ in the range of 40° to 165° with a full coverage in azimuthal angle (ϕ) (except gaps for the target-holder entrance at $\theta = 100°$ on top of the ball and vacuum pipe along beam axis at $\theta = 180°$). The shape and the construction of the inner surface of ball can be in a common way compared to the surface of a *soccer ball* — it is a finite normalized tight frame (FNTF) [73] and is completed with 20 identical *hexagon* and 12 identical *pentagon* structures. These polygons are further divided into identical triangles, thus reducing the pentagon into five triangles and the hexagon into six triangles (see Fig. 3.6). Each triangle represents here a single ball element (phoswich detector).

Shape of one single element is like a triangular prism with it's geometrical cross-section increasing along it's thickness as one moves outward (away) from the ball center

[2]A phoswich (phosphor sandwich) is a combination of scintillators with dissimilar pulse shape characteristics optically coupled to each other and to a common PMT.

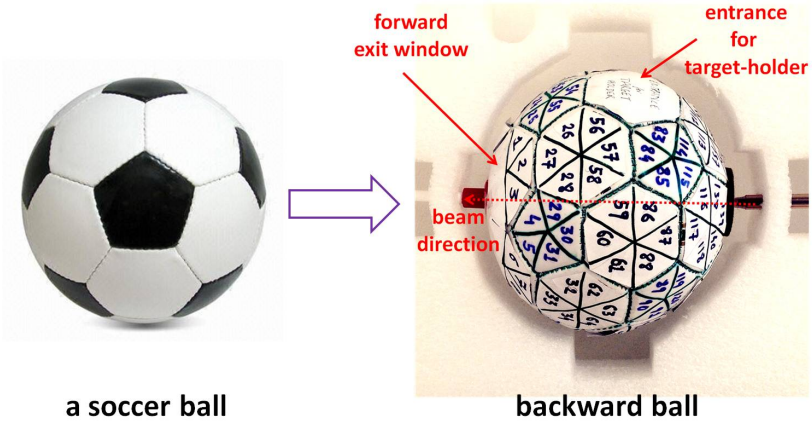

FIGURE 3.6: The left panel shows a soccer ball with it's surface complete with hexagons and pentagons (refer text for detail). On the right panel a model of the backward ball including target-holder entrance, forward exit window and beam-in pipe is shown.

in order to form the structure without gaps between the elements. The ball is acting simultaneously as a vacuum chamber and as a detector. Due to vacuum and absence of additional material or structure (except the target frame and the target window foil) inside the ball, the detected particle didn't suffer any significant energy losses[3]. In this way the ball allowed to detect particles with very low kinetic energies. The dimension of sides of a triangle face depends on the polygon shape (penta- or hexa-) to which it belongs. In hexagon, the triangle is equilateral (all sides with same size) while the one in pentagon is isosceles triangle (only two sides are the same, $a = b = 1.17 \times c$), see Fig. 3.7.

Each ball element is composed of two different types of plastic scintillators glued together (phoswich detector), a slow part from 1 mm thin BC-444 plastic and a fast part from BC-408 plastic. The physical parameters of these plastic scintillators are given in the Tab. 3.1. The thickness of the fast scintillator part is not the same throughout entire ball region. Below $\theta < 100°$ the detectors are of 9 cm thickness, while rest of the elements are of 3 cm thickness. Such a variety of thicknesses is due to energy difference between particles scattered at different polar angles. All the elements were painted with white color and glued with each other making the ball sphere (see Fig. 3.8).

The opening front window of the ball was made of thin Kevlar cloth of 250 μm combined with an Aramica foil of 50 μm [70]. It was glued to a metal ring holding the beam-pipe and attached to metal frame of the ball (see Fig. 3.8). This thin window is strong enough to hold the vacuum inside the ball allowing the forward scattered particles to pass through it with a very small energy-loss.

Taking into account the regions free of detector elements reserved for target holder entrance and the beam-pipe, the backward ball is left with 149 elements, see Fig. 3.9. The vacuum inside the ball down to 10^{-6} to 10^{-7} mbar was achieved during the measurements.

The granularity of the ball elements is poor compared to the forward wall. One single element covers an angular range as large as $\pm 20°$, in both ϕ and θ direction.

[3]Note that there is also a thin cylindrical aluminum foil used as a thermal shielding around the target cell.

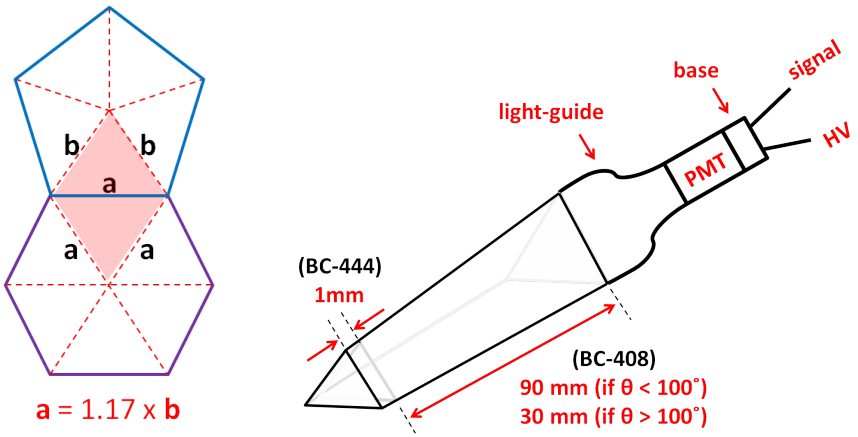

(a) (b)

FIGURE 3.7: A schematic view of the ball elements; (a) shows the two basic building blocks of the ball — the penta- and hexa- structures, and (b) shows details about a single phoswich ball element.

Moreover, the white paint appeared to be partially transparent, in consequence the scintillation light escaped to neighboring elements. Therefore, it was necessary to consider a cluster as a "basic element" instead of one single scintillator in the track reconstruction procedure. A signal from the slow phoswich component was difficult to detect due to a baseline fluctuations. Thus a particle identification was done only with the use of the wall detector and the kinematical constraints for the *dd* elastic scattering.

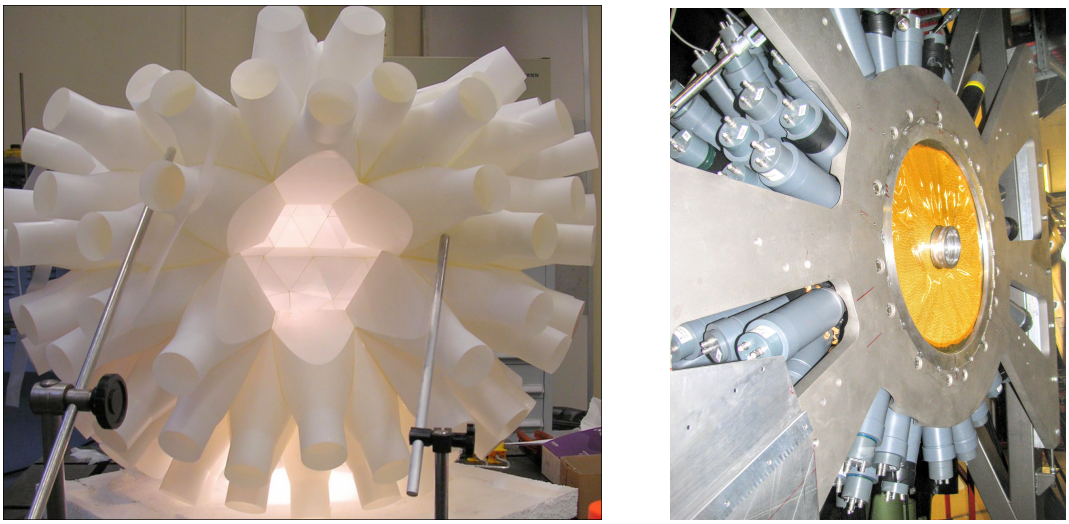

(a) (b)

FIGURE 3.8: Photographs of backward ball parts: (a) the ball elements glued together at the time of it's construction, and (b) the forward opening window.

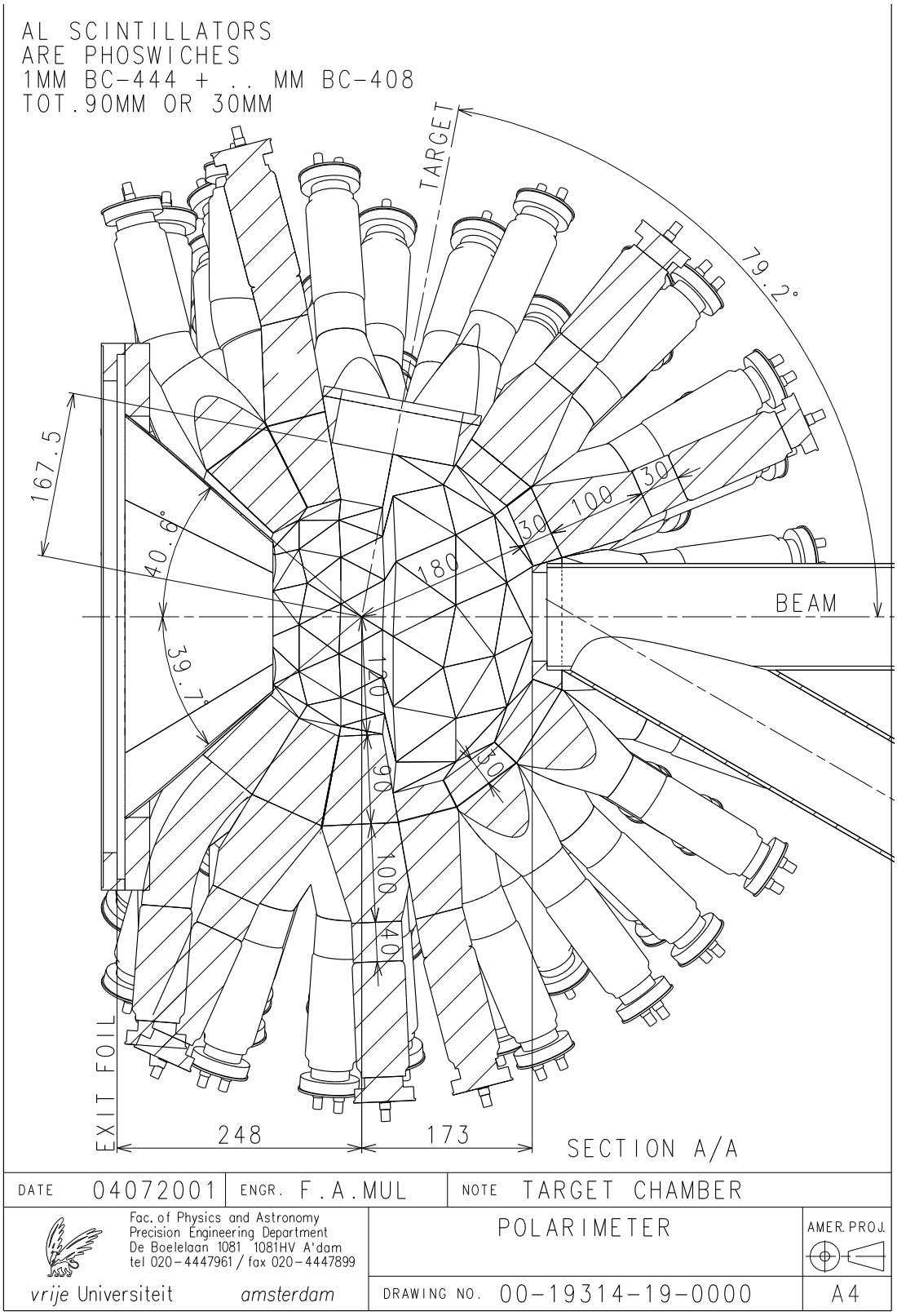

FIGURE 3.9: Details of the engineering design of the backward ball of BINA. All the distances between components and their sizes are shown in mm.

3.2.3 Electronics

The deuteron-deuteron collision may lead to several outgoing channels (See Section 2.3), out of which the elastic and the three-body breakup channels (registered as a single charged particle or a coincidence of two charged particles) are the most useful for this work. Due to their different cross-sections, the rates of events of elastic and of breakup processes can be different. Therefore one has to identify and selectively reduce (prescale) their rates. To do so, various trigger conditions, with appropriate pre-scaling factors, were prepared. These conditions were based on hit multiplicity in three groups of photo-multiplier tube (PMT) signals; left-hand side PMTs of E-detector (M_L), right-hand side PMTs of E-detector (M_R) and all ball PMTs (M_{ball}). Based on that, the registered three different types of events were as follows:

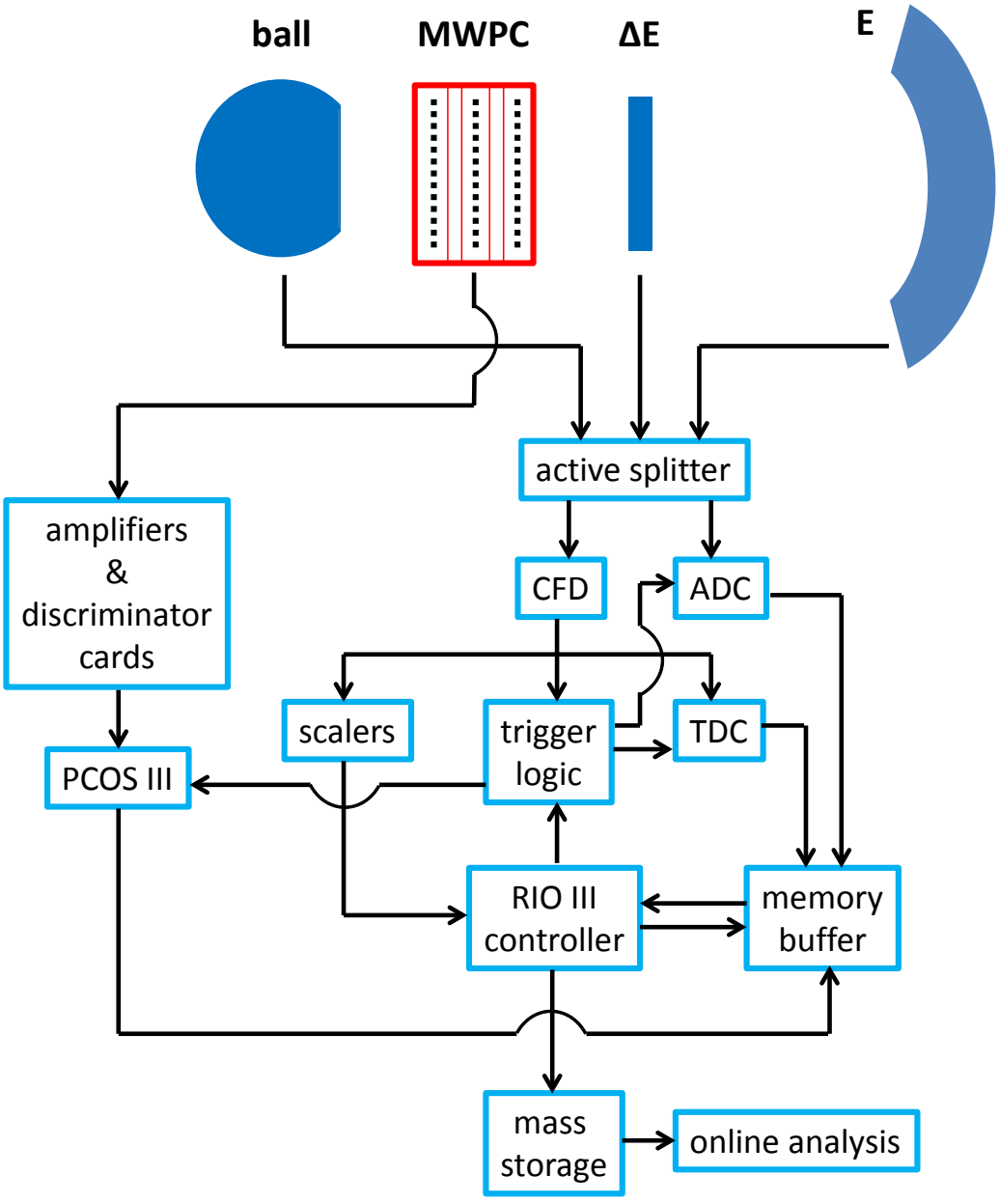

FIGURE 3.10: Simplified scheme of the electronics readout system of BINA detector setup.

1. Trigger T1 $\equiv$ $M_L \geq 2$ *OR* $M_R \geq 2$
   Coincidence of two charged particles registered in wall (wall-wall coincidence).

2. Trigger T2 $\equiv$ $M_{ball} \geq 1$ *AND* ($M_L \geq 1$ *OR* $M_R \geq 1$)
   At least one particle registered in wall and at least particle registered in ball (wall-ball coincidence).

3. Trigger T4 $\equiv$ $M_{ball} \geq 1$ *OR* ($M_L \geq 1$ *OR* $M_R \geq 1$)
   A minimum bias trigger, with at least one particle registered in the whole setup (single).

Each of the triggers was downscaled by a factor 2^x, where x=0 for T1, x=3 for T2 and x=5 for T4. A detailed description of the electronics, read-out and data acquisition can be found in references [74]. Here, only a simple electronics scheme of the setup is presented, see Fig. 3.10. First, the PMT signals were split into two; one of them was sent to Analog-to-Digital Converter (ADC) input for integration of the collected charge (equivalent to the energy of the detected charged particle) and the second one to the constant fraction discriminator (CFD). The output of CFD, then, was used for three purposes; to record rates into scalers, to store "start" time of the individual pulse in Time-to-Digital Converter (TDC) and for trigger definition.

Rates of single events were relatively larger than coincident events and therefore both the types of events were downscaled separately such that the total trigger rates were reduced to a level accepted by the DAQ. After downscale and proper delay, the logic sum of all triggers was used for defining the common signals for read-out, i.e. gates for all the ADCs and PCOS III as well as a common "stop" for all the TDCs. The hits registered in MWPC were read out via PCOS-III system, which was equipped with amplifiers/discriminators cards mounted directly on the chamber and coupled with latch modules. The PCOS-III generated a readout request if the signal, due to the passage of charged particle through any of MWPC planes, exceeded a certain threshold.

For every accepted trigger, the digitized pulse height from ADCs and the time information from TDCs were transferred using FERA bus to memory buffer units and to the front-end computer for readout. The corresponding MWPC hit information for each events, encoded into FERA format, was also inserted into the data stream for readout and combined into a single event which was stored on a mass-storage device.

3.3 Target system

Three types of targets were used in the experiment; solid (a polymer) CH_2, zinc sulphide (ZnS), and liquid deuterium (LD_2).

The ZnS target together with an empty cell were used to optimize the beam position and optics whereas CH_2 was used to make an online check of the experimental setup and optimize the settings (gain matching etc.). All the targets were mounted vertically on a holder in the center of the backward ball. The holder could be moved remotely by a pneumatic system. The holder moves along an axis which is inclined (about 10°) with respect to the vertical axis resulting in asymmetric number of detected particles between upper and lower half of ball. The target cell was thermally shielded by a thin

cylindrically-shaped aluminum foil with an opening for forward scattering part. This shielding caused asymmetric energy losses. More details can be found in Sec. 4.4.2.

Operating the liquid target requires additional equipment such as a cryogenic system, a heater, a gas-flow system, temperature sensors, and a temperature controller unit. The cell used in the experiment (see Fig. 3.11) is made of high purity Aluminium to optimize the thermal conductivity. The windows were covered by a transparent Aramid foil of 4 μm thickness. The typical operating temperature was 17 K at a pressure of 256 mbar for deuterium. The nominal thickness of the cell was 6.0 mm. In addition, the thickness of the target was increased about 0.6 mm due to bulging of the cell which leads to the thickness, ρh, of 107.2 $\pm$ 3.3 mg/cm^2, where, ρ is the density and h is the length of the target [75]. The size of the bulging was first estimated via a measurement of the target thickness as a function of a pressure at a room temperature. At the operational pressure the target had a bulging of 1.3 mm. However, the foils become more rigid as they cool down. So, the actual target thickness was obtained by comparing the cross section measurements at KVI between solid and liquid targets. The bulging at the operational temperature is found to be about 50% of the bulging at room temperature.

The procedure of filling the liquid target cell is a multi-step procedure. First, the empty cell is placed in the vacuum chamber, and deuterium is transported to the cell in a gas form at a constant pressure. Then the cell is cooled down near the triple point of the gas. As soon as the gas-to-liquid phase-transition occurs, an empty volume is created in the target cell. This volume is again filled with a new portion of gas, and procedure is repeated until the cell is completely filled with liquid. Usually it took about 11 cycles to fill the target. It is very important to keep the cell temperature well below the threshold of liquid-to-gas transition.

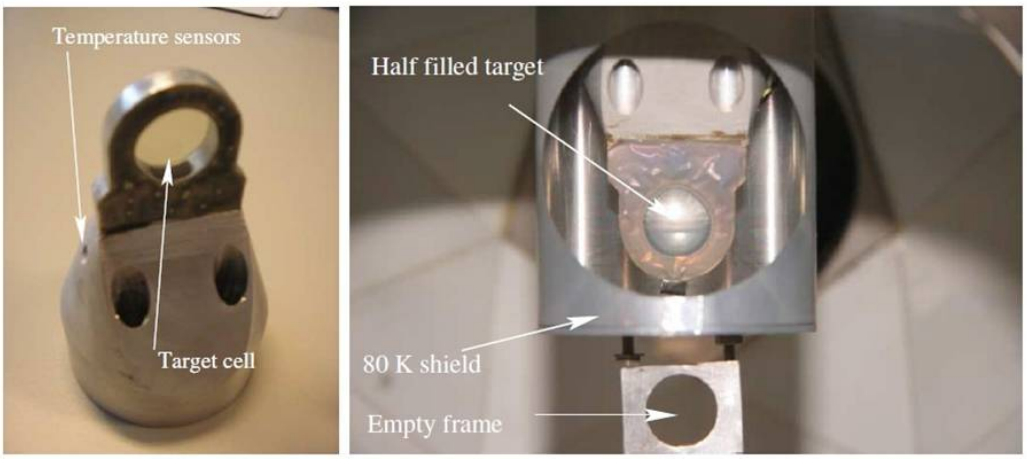

FIGURE 3.11: The target cell: (*left panel*) stand-alone; (*right panel*) mounted inside the BINA, backward ball. The cell is half filled with liquid deuterium. The thin Aluminum cylinder around the target cell isolates the cold head from the surrounding environment.

3.4 Beam intensity monitor

A Faraday cup was mounted at the end of the beam-line, to stop the beam and to measure it's intensity. The Faraday cup was made of a copper block containing a heavy alloy metal as the actual beam stopper. The current meter, connected to the Faraday cup, was calibrated using a precision current source (KEITHLEY 263 calibrator/source) with an uncertainty of 2%. The output signal (voltage) of the current-meter is converted into frequency via voltage-to-frequency converter and registered in a scaler readout by the DAQ. The beam current was typically of few pA (1-4 pA). For the present experiment, the Faraday cup didn't work correctly (see Fig.4.2). Therefore, for the normalization purpose, already measured elastic scattering cross-sections were used (see Section 4.6).

Chapter 4

Data Analysis

4.1 Framework

This chapter gives a detailed description of the steps undertaken to extract the differential cross-section for the $dd \rightarrow dpn$ breakup process measured at the beam energy of 160 MeV. The data analysis was performed with the use of the dedicated software based originally on FORTRAN and C programming languages. For the current analysis the main sorting program (FBRun) was updated, utilizing the ROOT package (C++ based data analysis framework of CERN).

First, the data were presorted on a raw level, then tracks belonging to charged particles were reconstructed. On this physical level, the FBRun software provided all the necessary information about the particles such as the deposited energy and emission angles. The data at this stage were stored in the root-trees and then used in further steps of the analysis. The parts of the runs characterized with unstable beam current or problems in functioning of any system elements were carefully removed. A geometry cross-check of the wall detector as well as a correction of a beam-shift from the target center were performed within analysis of the preceding experiment with the same experimental conditions [76], resulting in precise momentum reconstruction of the detected charged particles. With the hodoscope-like geometry of forward wall it was possible to perform a particle identification via a conventional ΔE-E technique. Moreover, for the first time the thorough analysis of the data registered in the backward wall was performed. Due to not high enough efficiency of ball, those data were used for checks of systematic effects only.

To normalize the breakup cross-section, it is necessary to have the elastic cross-section of the simultaneously measured *dd* elastic scattering or to know precisely the luminosity. Due to malfunction of the Faraday-cup the beam-current measurement was not reliable and therefore extrapolation of the *dd* elastic scattering cross-section was performed based on nearest available energies, i.e. 130 MeV and 180 MeV [40].

4.2 Pre-analysis of raw data and event selection

An overview of the preliminary data presorting and track reconstruction as well as a first step of physics analysis are presented. The raw experimental data were presorted with respect to elementary constraints imposing on TDC and ADC signals. On this

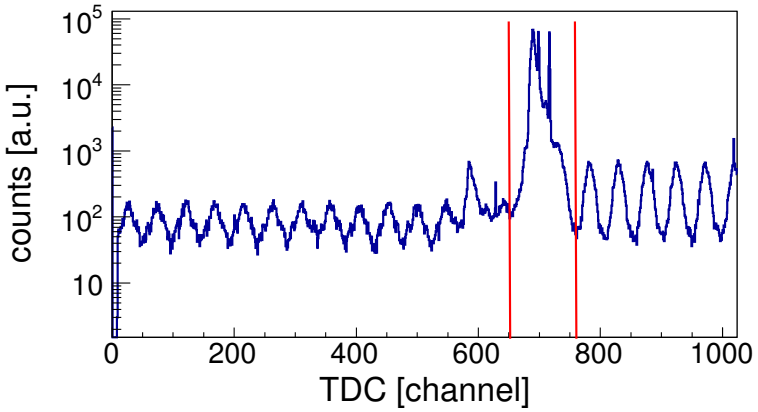

FIGURE 4.1: A sample spectrum of the TDC distribution for 6^{th} E-scintillator is shown. The gate for events to be accepted as "true+random" coincidences is marked with vertical lines.

level one is able to control the detector performance and select reliable data for further analysis. The next level physical sorter delivers useful quantities, such as the particle's momenta and energies (after calibration), which are then directly used for evaluation of the observables.

The main steps of a pre-analysis; the time information, the track reconstruction, the particle identification and selection of the reaction channels of interest are described in the following subsections.

4.2.1 Time information

In general the events of interest are coincidences of two charged particles. To select ones in a proper way, gates were applied to the TDC (time-to-digital converter) spectra of all scintillators in the forward wall. Fig 4.1 shows an example of such spectrum for a chosen wall scintillator[1]. The time was measured with respect to the trigger. The plot presents a number of equidistant peaks, each representing the particles coming from a single beam burst. The highest peak corresponds to the beam pulse which triggered the DAQ, it contains both "true" and "random" coincidences. The other peaks represent the particles accidentally coincident with the trigger. To minimize the contribution from the "accidental" coincidences in the measurement, the beam current was set on the lowest possible value, usually a few pA.

Applying the gate on the TDC spectra (enclosing the time period of highest peak), assures suppression of the accidental events contributing to the background [77, 78]. In order not to loose any "true" coincidences, the gate was chosen slightly wider to cover some part of the events from the neighbor beam burst. The remaining random coincident particles were removed in the subsequent data analysis steps by applying various cuts on the kinematical spectra.

In order to remove parts of the data collected with not good detector performance, histograms of a time evolution of various quantities, measured during the experiment, were prepared for the whole data sets, see Fig. 4.2 for details. Based on the plots, unreliable parts of the data were identified and then carefully removed, improving the

[1]No TDC was available form the backward ball, therefore all the registered hits were accepted.

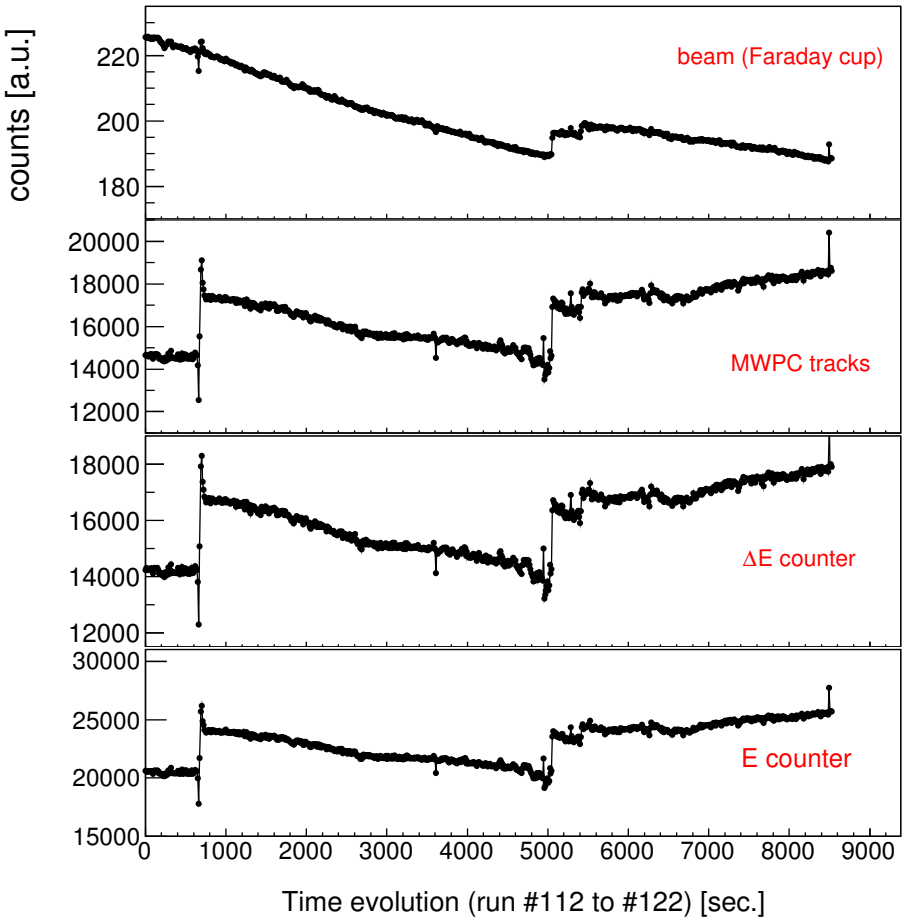

FIGURE 4.2: Time evolution of various counters is presented for a chosen part of the experiment. Panels, in top to bottom order, represent measured quantities: beam current, MWPC Tracks, ΔE counter and E counter.

overall data quality. The beam current measured and information from various detector counters (E, ΔE, MWPC) were following nearly the same structure, however at some range (as it can be seen in Fig. 4.2)they malfunctioned and therefore the region was excluded from the analysis. The beam rates from Faraday cup were found unreliable for most of the data set and therefore they were not used.

4.2.2 Track reconstruction

An "event" was reconstructed from the "hit" information of detected charged particles in the various detector elements. First the "tracks" were built for each event, starting from hits in MWPC wire-planes. Then the hit was accepted if correspondence with the ΔE and E detectors was confirmed. Such events were labeled as "good" ones. In a situation when a particle was not detected in MWPC or in ΔE detectors, but was registered in E, it was accounted for a so-called "bad" event. Such events (tracks with holes) were also used in the analysis for the purpose of the detector efficiencies calculations.

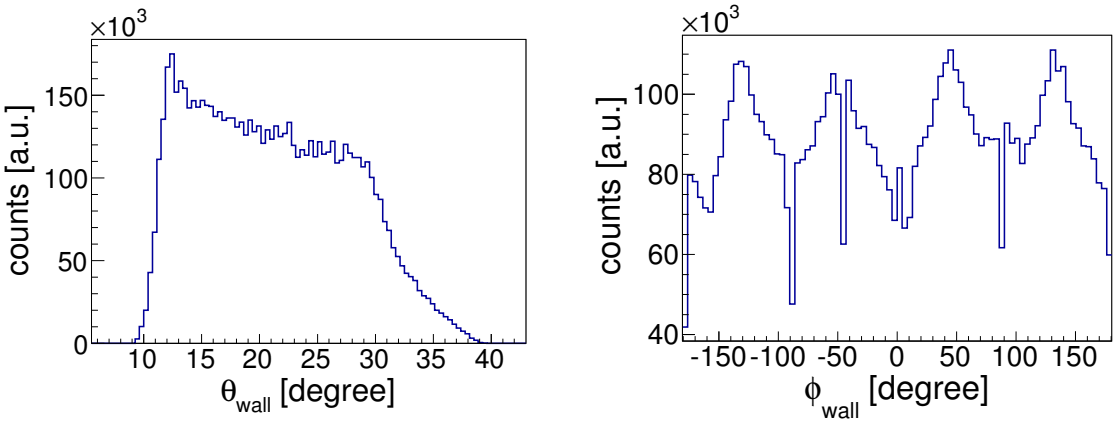

FIGURE 4.3: Impact of the angular acceptance of the wall detector on the number of detected particles. The angular ranges covered in a polar angle (left panel) θ is from 10° to 40° and full in an azimuthal angle (right panel) ϕ.

Knowing the crossing point between the corresponding MWPC wire-planes and distances between the target and the wire-planes and assuming particle emission from the target center, it was possible to obtain its polar (θ) and azimuthal (ϕ) scattering angles in the laboratory frame, see Fig. 4.3.

The MWPC detector can was also used to test the wall setup geometry. Such a cross-check is illustrated in Fig. 4.4, where selected numbers (even or odd) of the E-bars and ΔE strips are seen in the MWPC x-, y- planes. For this, single track events registered in the selected (E or ΔE) scintillator were projected onto the corresponding planes.

In the case of the ball detector the track reconstruction procedure relied on clusterization. For particles registered in a specific ball element, the polar (θ_{ball}) and the azimuthal (ϕ_{ball}) angles were calculated from the centroid of that ball element, see Appendix A. Angular coverage of a ball element, is up to ±10°, therefore the angular

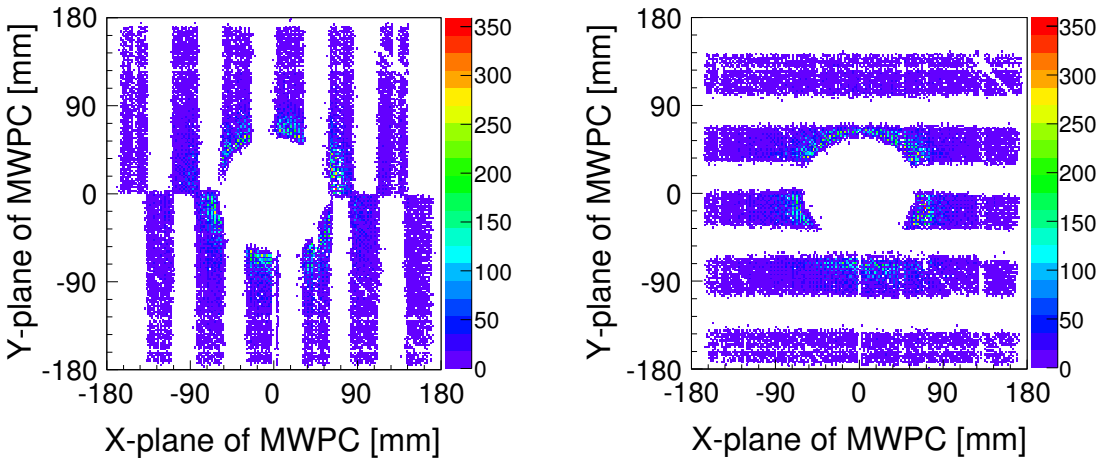

FIGURE 4.4: Response of the MWPC detector, when a selected (odd or even numbered) scintillator of ΔE (left) and E (right) responding, is presented. Not working wires are also visible.

resolution is much poorer than the one in the wall. However, a clusterization method was implemented to improve the angular resolution in the ball, as described in the section 4.4.2.

The data were collected with different trigger patterns (as it was mentioned in Section 3.2.3) to selectively enhance the studied reaction channels. Regarding the number of reconstructed tracks (one or two) within an event and by imposing TDC/ADC constraints, the events were classified as "single-track" or "double-track". To investigate the dd elastic scattering, one needs to analyze the wall-ball coincidences mainly collected with T2 trigger or using the single track events.

4.3 Particle identification

The particle identification (PID) was performed using the ΔE-E technique. For each ΔE-E telescope, a two dimensional "ΔE-energy loss vs. E-energy deposited" spectra were prepared. Particles energies for different channels are restricted by the kinematical rules, therefore their presence or place on a ΔE-E spectrum changes from one telescope to another. Sample ΔE-E spectra are presented in Fig. 4.5. The long branches of protons and deuterons are indicated as originating from the breakup reactions, while the two-body final states (elastic scattering and the transfer reactions) are seen as forming distinct spots on the plot. Separation between the two breakup loci was found quite well over the entire wall region.

To distinguish and select the different particle types, graphical cuts ("gates") were defined for each individual ΔE-E telescope. The protons or deuterons were selected by lines which define an arbitrary area ("banana" shape), wide enough to avoid significant

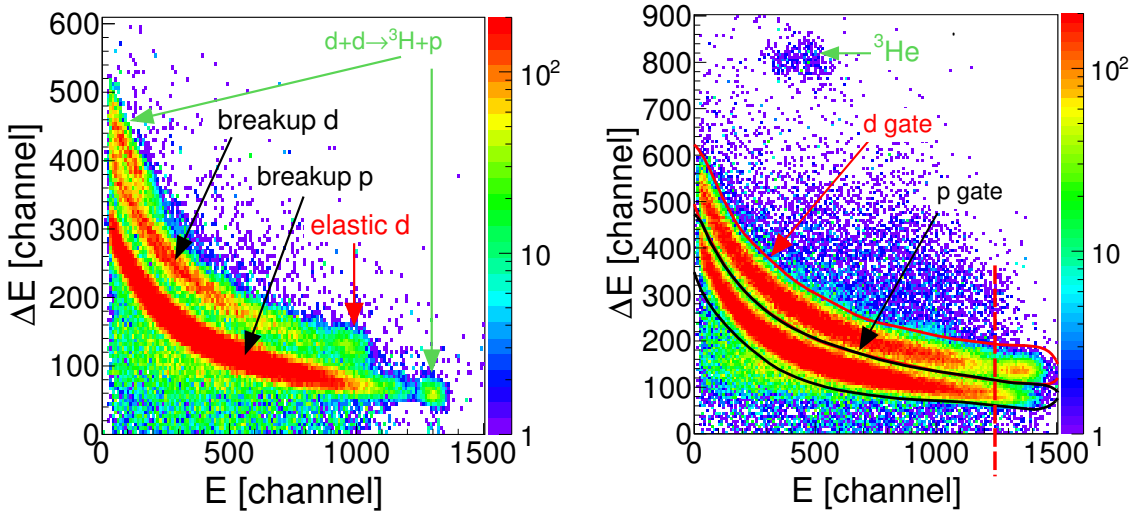

FIGURE 4.5: Particle identification based on ΔE-E spectra is presented for two different telescopes. On the left panel (ΔE=1 and E =1) particles originating from the different reaction channels were indicated. On the right panel (ΔE=3 and E =1) the sample of applied graphical cuts is presented. The particles originating from the transfer channels are also visible. The cut on peak of the elastically scattered deuteron, within d-gate, is shown with a dashed vertical line.

losses of the particles, see Fig. 4.5, right panel. After introducing the PID method into the analysis, a calibration was performed for each type of particles and various reaction channels were identified.

4.4 Energy calibration

The differential cross section of the break-up reaction for a chosen angular configuration — defined by polar angles θ_d,θ_p and a relative azimuthal angle ϕ_{dp} of the deuteron and proton — is given as a function of their energies, E_d and E_p. Alternatively the observable is presented as a function of the arc-length, S, along the breakup kinematical curve (see Ch.2). Therefore, it is highly demanded to have a reliable and an accurate energy calibration of the detectors. The calibration was performed for the wall E-detector and the ball scintillators based on a specific data sample and the procedure is described in the following subsections.

4.4.1 Wall scintillators

When a charged particle enters the scintillator volume, it loses its kinetic energy by excitation of atomic electrons along its trajectory. These excited electrons then de-excites via emission of light (known as fluorescence effect). The *light signal* is converted into an *electronic signal* (ADC channel) with the use of the photomultiplier tubes (PMTs) coupled with the scintillator via a light-guide. To assure light tightness and good reflectivity of the surface, a layer of an aluminised thin Mylar foil was wrapped on the scintillators.

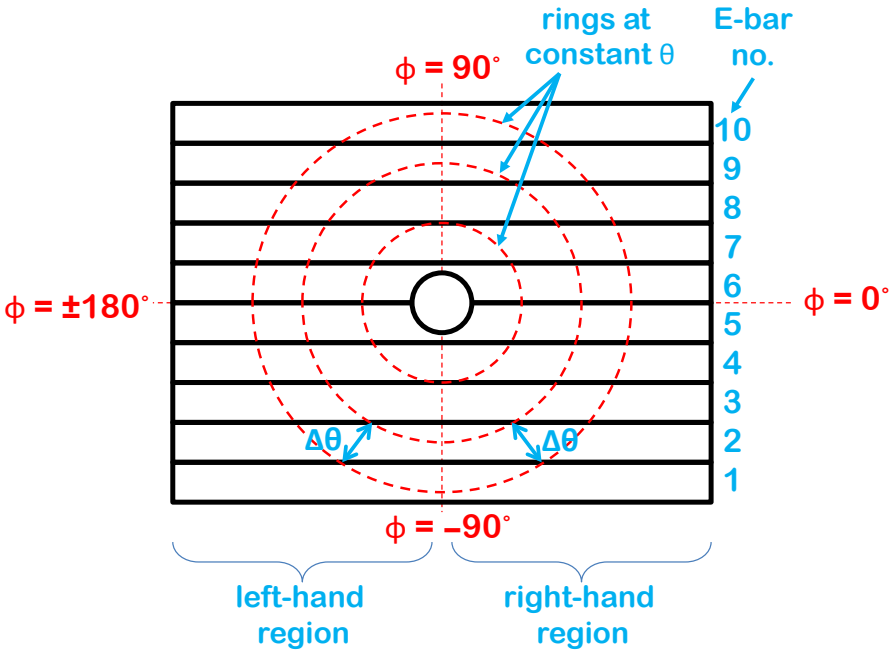

FIGURE 4.6: The array of 10 E-scintillators in the forward wall is shown schematically. The polar angles θ (red circles) and the selected azimuthal angles $\phi = 0°, 90°, -90°$ and $\pm 180°$ are marked. Each E-scintillator can intersect twice with a circle of given θ angle, in the left- and in the right- hand region.

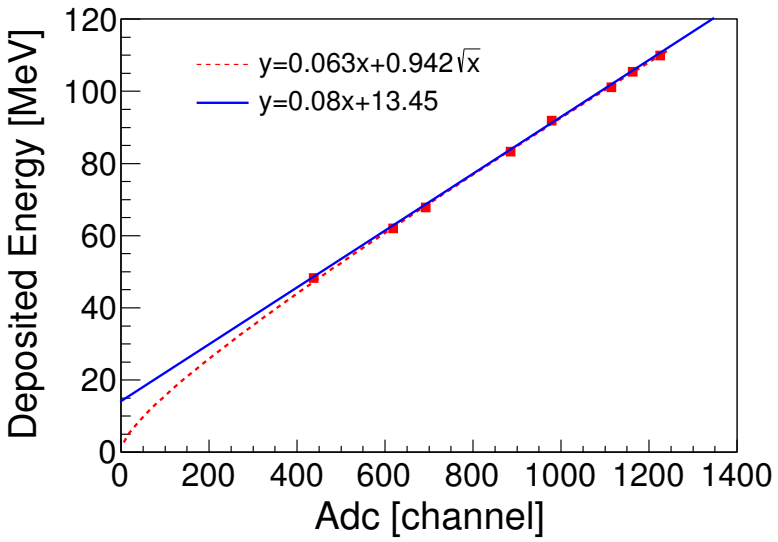

FIGURE 4.7: The relation between ADC channel and the simulated energy deposit of elastically scattered protons (MeV) is shown with a linear and a non-linear fits. The error bars for data points (dots), in most cases, are smaller than the dot size. The non-linear function was fitted to account for the small quenching effect in such a way that it passed through origin (0,0) of the presented graph.

Purpose of the calibration procedure is to convert the obtained ADC channel into the particle's initial energy at the reaction point. This is done mainly in two steps. Firstly, the ADC channels are translated into energy deposited by a particle (E_{dep}) and, secondly, corrections on the energy loss along the particle path between the target and the E-detector are applied. The first step was based on the energy deposited by the protons originating from the *dp* elastic process (measured in the preceding experiment with the same experimental conditions in dedicated runs with the use of the set of steel plates as the energy degraders). A detailed description of the procedure can be found in [79]. Here only a brief description of both the steps are explained. The conversion of the obtained proton calibration function, into the one for deuteron, is presented.

Step 1. Translating channel into deposited energy: In the forward wall of BINA, each stopping E-detector is supplied with two photomultiplier tubes (PMTs) on its two ends (left-PMT and right-PMT). When a charged particle hits the E-detector, in an ideal condition both the PMs respond, giving two pulse height values.

The gains of PMT's were well matched, so the difference in the signals, obtained from the left-PMT and right-PMT, is mainly due to different light attenuation. This results in position-dependent light collection along a scintillator assembly. To perform the energy calibration for a given E-bar, a position independent C_{LR} value was obtained as a geometric mean of the left-PMT signal (C_L) and the right-PMT signal (C_R), i.e. $C_{LR} = \sqrt{C_L \times C_R}$. The new quantity C_{LR} is called a "reduced signal" for a hit in a single E-detector and the position-dependent part of exponential attenuation effect cancels in this average. The central two E-detectors were partially cut from the middle (due to a beam-pipe hole) and therefore the "reduced signal" for them was taken as a sum of the two signals, i.e. $C_{LR} = C_L + C_R$, instead of the multiplication. Thus

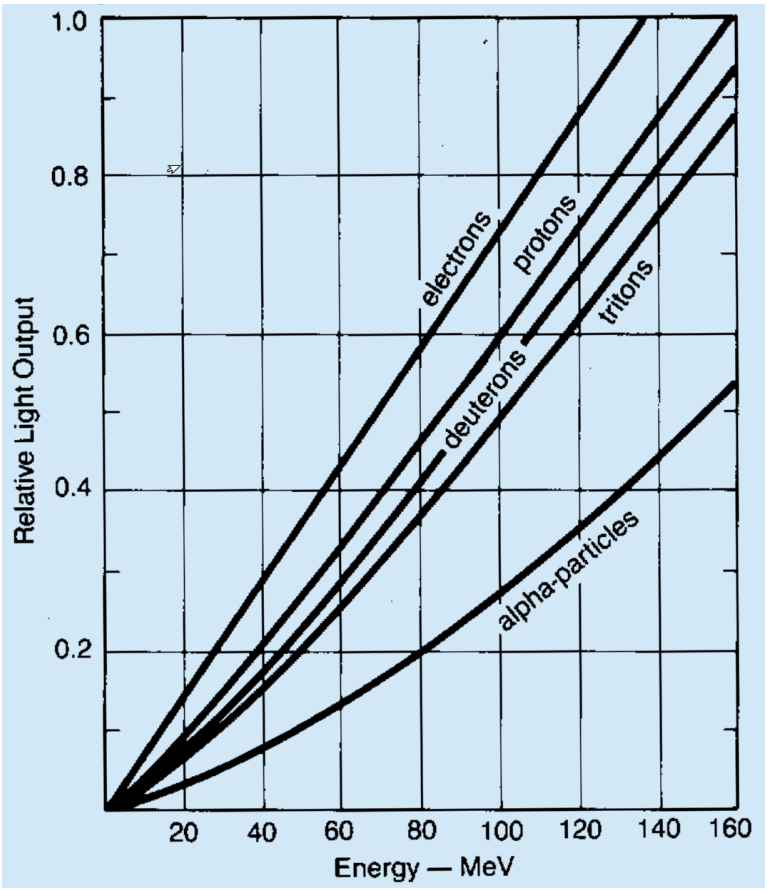

FIGURE 4.8: The light output relation between different particles for the BICRON plastic scintillators. Image Credit: Saint-Gobain Ceramics & Plastics, Inc.

avoiding the "zero signal" situation when one of the two PMT signals is absent.

The obtained C_{LR} hardly depends on the hit position [41,74]. The relation between the deposited energy and C_{LR} is represented by a nonlinear function, with parameters depend on the E-detector, side (left, right) of the detector and the θ angle (see Fig. 4.6). In general the function can be written as follows:

$$E_{dep}(\theta) = f(C_{LR}(\theta, side)) \tag{4.1}$$

where $E_{dep}(\theta)$ is the energy deposited in the E detector, obtained with the use of the GEANT4[2] simulation for the BINA detector. The detector geometry and the important parameters of the set-up such as materials, dimensions and distances are included in the simulation.

The relations described with the Eq. 4.1 have a non-linear character at energies below 40 MeV which is caused by the quenching effect (described with the Birk's formula [80]). The observed amount of the quenching effect was very small therefore non-linear correction functions were fitted (see in Fig. 4.7) to the $E_{dep}(\theta)$ vs. C_{LR} dependencies. The functions obtained are the calibration for a given polar angle θ (left or right-half side) and for a given E-detector.

[2]GEANT4 is a software toolkit for both full and fast Monte-Carlo simulation of detectors in high energy physics.

Since the deuterons from the elastic *dp* process are not detected in full range of θ angle in the wall, the obtained proton calibration functions were used to calculate the same dependencies for the deuterons. Due to different scintillation light output for protons and deuterons a well known light-output to energy deposit relations [81] for these particles (as shown in Fig. 4.8) were used to translate the proton function into the one for the deuterons (and similarly to the ones for ^{3}H and ^{3}He). The punch-through protons were observed in a region of small θ angles and the effect of incomplete energy loss was corrected for by slight change of the light output relation at the highest energies. A final formula which was used to recalculate the light outputs of protons (E_{dep}) into the one for deuterons (E^d_{dep}) is given as follows:

$$E^d_{dep} = a_0 + a_1 E_{dep} + a_2 E^2_{dep} + a_3 E^3_{dep} + a_4 E^4_{dep} + a_5 E^5_{dep} \tag{4.2}$$

with fitted parameters:
a_0=0.79±0.21,
a_1=1.52±0.03,
a_2=(-1.75±0.12) $\times 10^{-2}$,
a_3=(2.51±0.20) $\times 10^{-4}$,
a_4=(-1.56±0.14) $\times 10^{-6}$,
a_5=(3.49±0.37) $\times 10^{-9}$
E^d_{dep} (E_{dep}) denotes the energy deposited by deuteron (proton).

Step 2: Converting deposited energy (E^d_{dep}) into initial energy (E_{init}): The energy deposited by a particle in the E-detector is lower compared to its initial energy E_{init}. It is due to the energy-loss in the materials (such as target material and window, opening flange of BINA, MWPC, ΔE, air, wrapping foil etc.) placed between the

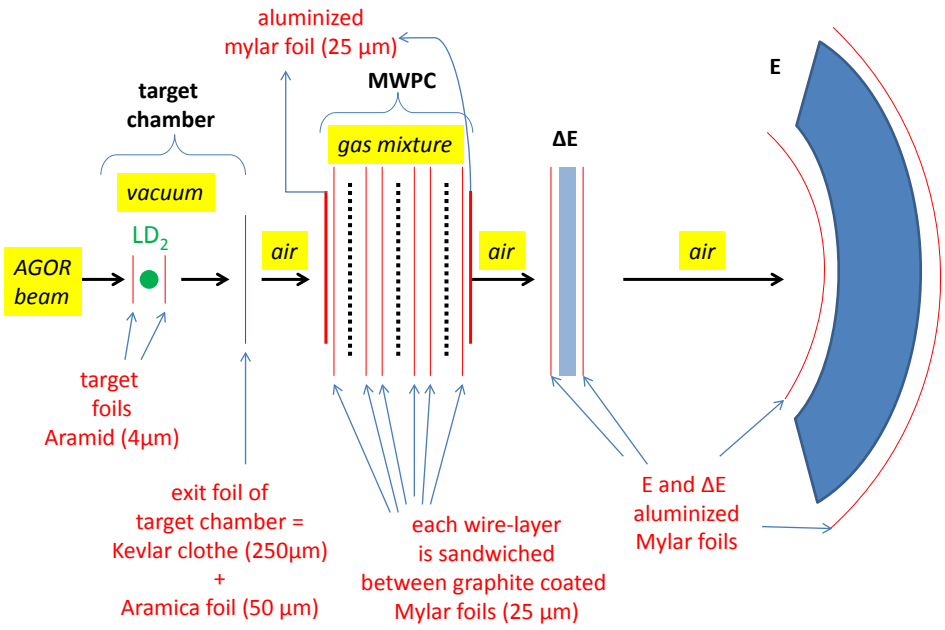

FIGURE 4.9: A schematic view of the materials in between the reaction point and hit position in the E-detector. The figure is not to scale.

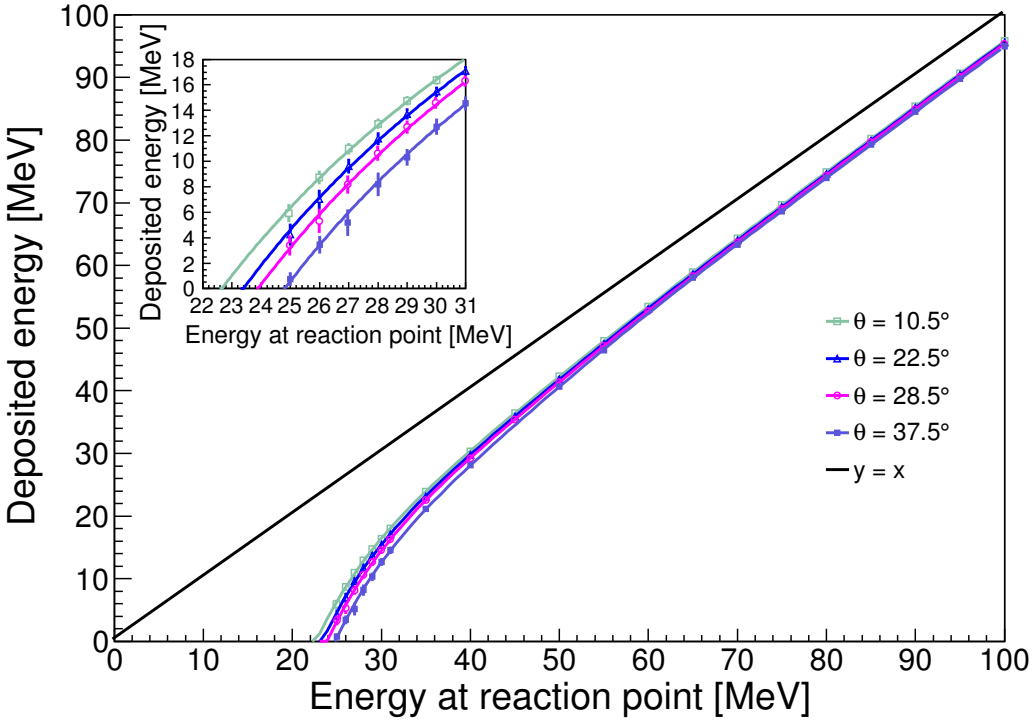

FIGURE 4.10: The plot presents energy deposited in the E-detectors vs. energy at the reaction point for different scattering angles of the deuterons. The inset shows zoom of the low energy range where the energy loss depends on scattering angle of the deuteron. The diagonal line (y=x) was drawn to show deviation from the linear response.

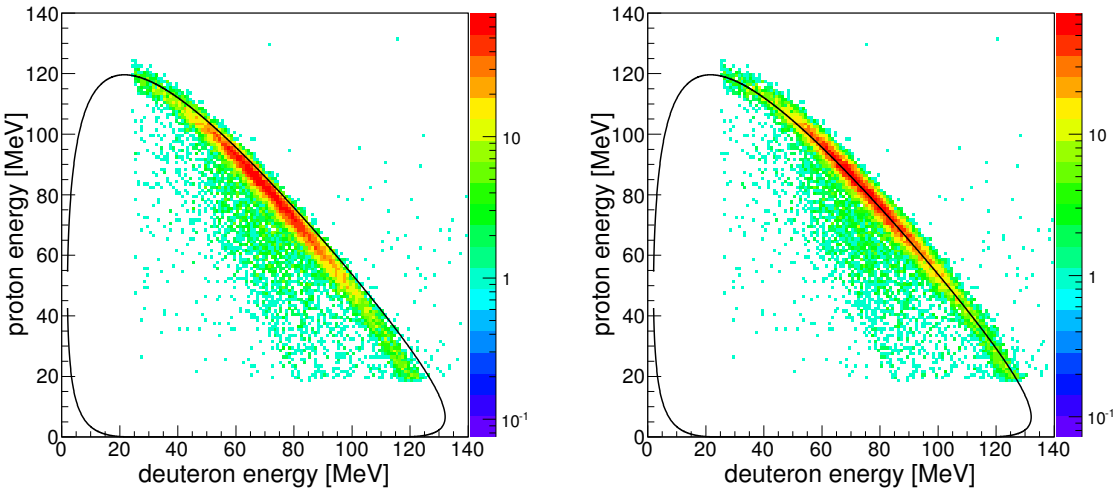

FIGURE 4.11: A breakup kinematics; range of accepted data, defined as $\theta_d = 20 \pm 1°$, $\theta_p = 30 \pm 1°$ and $\phi_{dp} = 180 \pm 5°$, is presented. The solid line refers to the kinematics calculated for the central values of this range. Left panel shows the kinemtics before applying the light output correction for deuteron (Fig. 4.8) and the right panel after the correction.

reaction point and the E-detector, see Fig. 4.9. These losses depend on the scattering angle.

To correct for this effect, the GEANT4 simulation was utilized. The particles (protons and deuterons) were generated at given polar angle θ energy E_{init} changed with a step of 1 MeV at lower energies (below 30 MeV) and a step of 5 MeV at higher ones. The distribution of the simulated deposited energy was then fitted with a Gaussian function. The mean values (E_{dep}) obtained from the fits were then plotted as a function of the corresponding E_{init}. Finally a polynomial of rank 8 was fitted to obtain the relation ("correction function") between E_{dep} and E_{init}, see Fig 4.10. The procedure was repeated for all the bins in the polar angles, varied between 10.5° and 37.5° with the step of 3°.

To check the calibration correctness, a kinematical relation for deuterons and protons from the $dd \rightarrow dpn$ breakup was drawn (see Fig. 4.11). One can see that the experimental data follow the calculated kinematics.

4.4.2 Ball scintillators

In the experiment presented in this work, only 55 out of all the 149 ball elements were put into operation, allowing to detect a charged particles scattered with polar angles up to 80° (see Appendix A). Since only thick scintillators were used (no phoswich function), therefore a direct particle identification was not possible. To overcome this obstacle, the kinematical relation of the elastic scattering were used to perform the ball calibration. Since the ball elements are covering polar angles above 40°, it was necessary to use wall-ball coincidences to select the dd elastic scattering process. The particle detected in the wall was required to be deuteron (selected by particle identification on ΔE-E) with energy above certain threshold and co-planar with the corresponding coincident deuteron in the ball, that is $|\Delta\phi - 180°| < 10°$. At this point, the angles in ball (ϕ_d^{ball} and θ_d^{ball}) were taken at the centroid of ball elements.

Another obstacle was the lack of light tightness of the ball elements, which resulted in additional contributions from the neighboring elements to the registered signal, i.e. a particle was registered in the ball with more than one element responding. Contribution of such events was significant and could not be neglected. Therefore to reconstruct a

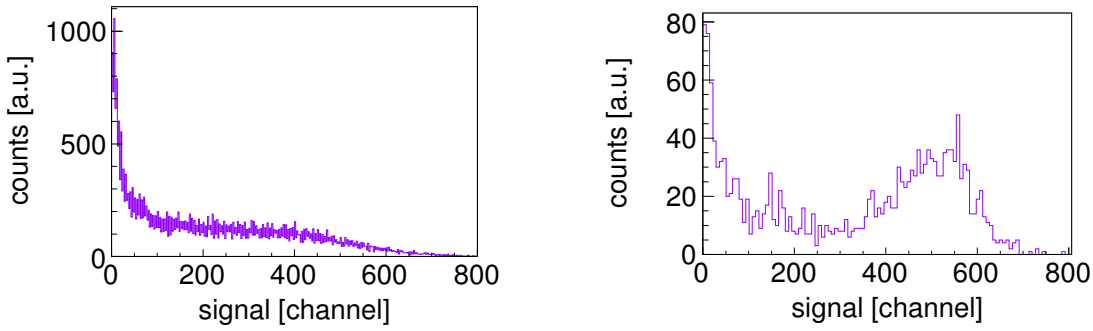

FIGURE 4.12: The ADC spectrum for a given ball element. The left panel shows distribution before applying any cuts and the right panel presents the same distribution but after selecting the wall-ball dd coincidences.

particle emission angle and energy, a cluster instead of a single element was considered in the further analysis.

In order to obtain reliable cluster information (energy and angles) of a reconstructed event, one needs to balance the signal (ADC channel) values, correcting for gain variations between individual PMTs. Therefore a preliminary calibration was performed and the cluster candidates were selected. The procedure is briefly described in following paragraphs.

Preliminary calibration, (without clusterization): At first, the ball elements characterised with producing noisy signal or the "dead" (not working) ones were discarded from the analysis. For the remaining elements, the so-called "well controlled" wall-ball coincidences originating from elastic *dd* scattering were chosen in the following three steps:

step 1: Knowing the angular ranges (both, polar and azimuthal) of a given ball element and using the kinematical relation for the elastic *dd* process, the angular ranges (in $\Delta\theta_{wall}$ and $\Delta\phi_{wall}$) of the corresponding coincident deuteron in wall were fixed. This ensured that the particle in ball is the deuteron from the elastic dd process with very low admixture of breakup protons. Fig 4.12 shows sample ADC spectra before and after applying these cuts.

step 2: The elastically scattered deuterons were selected in wall with a bin $\Delta\theta_{wall}$ such that the corresponding bin $\Delta\theta_{ball}$ of the deuteron in ball was lying close to the geometrical center of that element. This reduced the number of events which were registered as a cluster.

step 3: then the events were filtered by applying upper limit on the amount of the light leakage from a given ball detector to its neighbors. Depending on the ball element, the upper limit value was set between 1-10%.

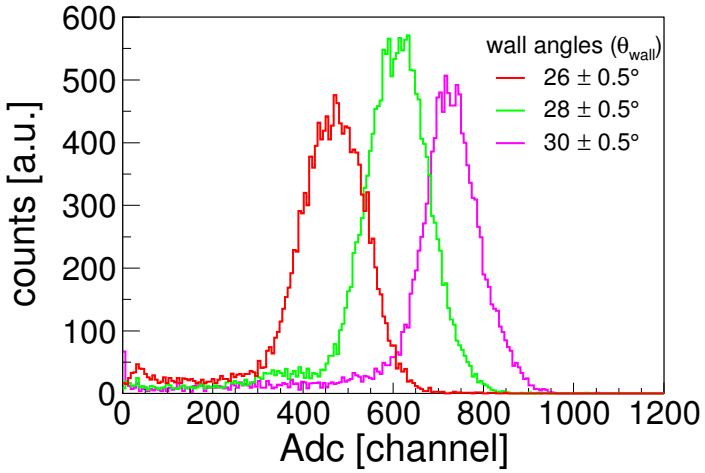

FIGURE 4.13: A sample spectrum of ADC response of a chosen ball element (here #51) for *dd* elastic scattering. Few different cuts on θ_{wall} were imposed (see the legend) producing peaks in the corresponding ADC spectra (different line colors).

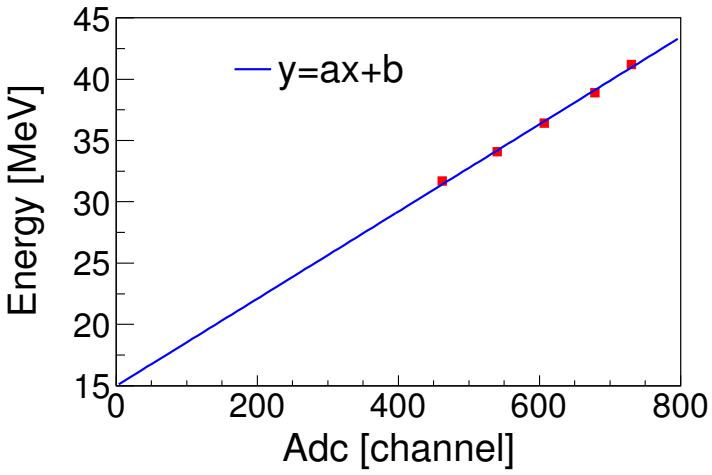

FIGURE 4.14: A sample of the applied linear calibration fit is presented for a given ball element. The fit parameters are a=0.03557±0.00014 MeV/channel and b=14.975±0.089 MeV.

Ideally the steps 2 and 3 are selecting events with "single detector clusters". Within these well controlled events, when selecting a specific polar angle (θ_{wall}) of the deuteron detected in the wall, one expects a corresponding energy peak for the coincident deuteron in ball.

By changing the θ_{wall} values, the corresponding peak in a given ball element was shifted, see Fig 4.13. Knowing the θ_{wall} and therefore the energy E_{ball} deposited in ball (from the kinematics), it was possible to find a relation between the ADC channel and energy. Since the energy range covered by the ball is very small, a simple linear approximation function was assumed, see Fig. 4.14.

The ball elements were classified into six rings and then into subrings charecterized by the same geometrical orientation. Only the first ring (having three subrings) and the second one (with four subrings) were working, see Fig. 4.15. Such classification not

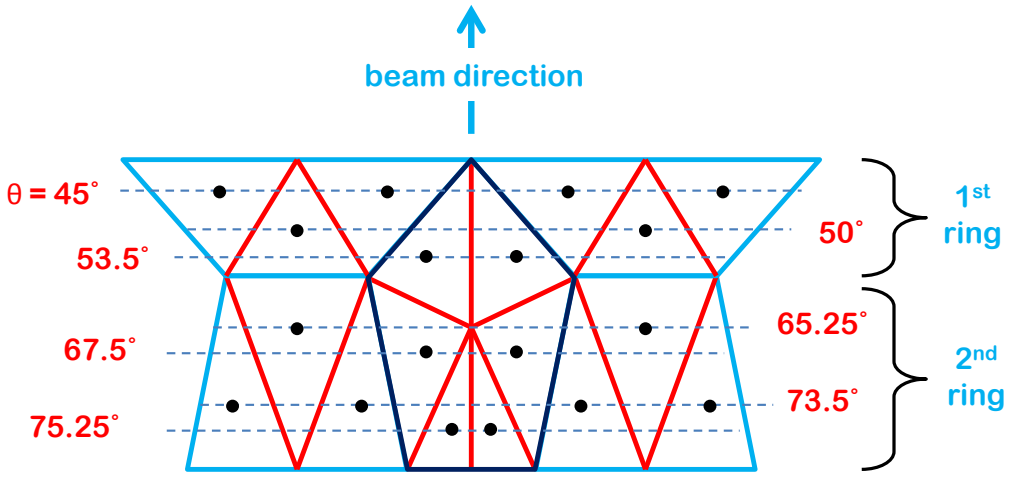

FIGURE 4.15: A part of the Mercator projection (bending of lines has been neglected) for the first two rings is shown schematically. Each ring has triangles with their different orientations — in each orientation the centroid of a triangle coincides with a common polar angle θ.

only simplified the task of finding the elastic peak position in the ADC spectra, but also allowed one to identify unusual behavior of any ball element within the subring.

To be in consistence with the forward wall geometry, the azimuthal angles (ϕ) of the ball were considered in the range from -180° to +180°, with the lower half ball covering a range from -180° to 0° and upper one from 0° to +180°. What is more the target was mounted in such a way that it was slightly tilted with respect to the vertical axis (see Fig. 3.9). Therefore the particles which scattered in the lower half region of the ball, passed through an extra material around the target (the thermal shielding and the target cell). In consequence, the energy of the detected particles was very low or the particles were stopped before they reached the detector. This manifested itself as up/down asymmetry in a spectrum of the relative azimuthal angles for the wall-ball coincidence, see Fig. 4.16.

An example of the wall-ball polar angles correlation, for a co-planar dd elastic scattering process, is presented in Fig. 4.17. The most populated regions on a given subring reproduces the proper θ_{wall}-to-θ_{ball} kinematical relation.

Cluster information: A cluster consist of a group of ball elements or a single ball element. The neighboring channels are considered to belong to the same cluster if their energy is above certain threshold. A given cluster is characterized with its azimuthal ϕ_c and polar θ_c angles and its energy E_c. The ϕ_c and θ_c are calculated as weighted average of the angles of the cluster elements as follows:

$$\phi_c = \frac{\sum_{i=1}^{n} \phi_i E_i}{\sum_{i=1}^{n} E_i} \tag{4.3}$$

$$\theta_c = \frac{\sum_{i=1}^{n} \theta_i E_i}{\sum_{i=1}^{n} E_i} \tag{4.4}$$

where n is the number of elements constituting a cluster and i refers to the i^{th} element[3] in the cluster.

In order to reconstruct the cluster energy, one needs to take into account a so-called attenuation factor α which refers to the light loss on the borders of the ball elements. Thus the cluster energy is calculated as follows:

$$E_c = E_{max} + \sum_{i=1}^{n-1} (1+\alpha) E_i, \tag{4.5}$$

where n and i have the same meaning as in the Eq. 4.4 and Eq. 4.3, and the E_{max} is the energy deposited in a central cluster element where the particle is detected (deposits the largest part of its energy). For the clusters, it was sufficient to take only the nearest neighboring elements (3 on the sides and 9 on the vertexes), see Appendix A for details. The estimation of α was done by looking at cluster events where only two adjacent ball elements responded to the detection of an elastically scattered deuteron.

[3]Note that the angles (ϕ and θ) for a ball element are at the centroid of the element.

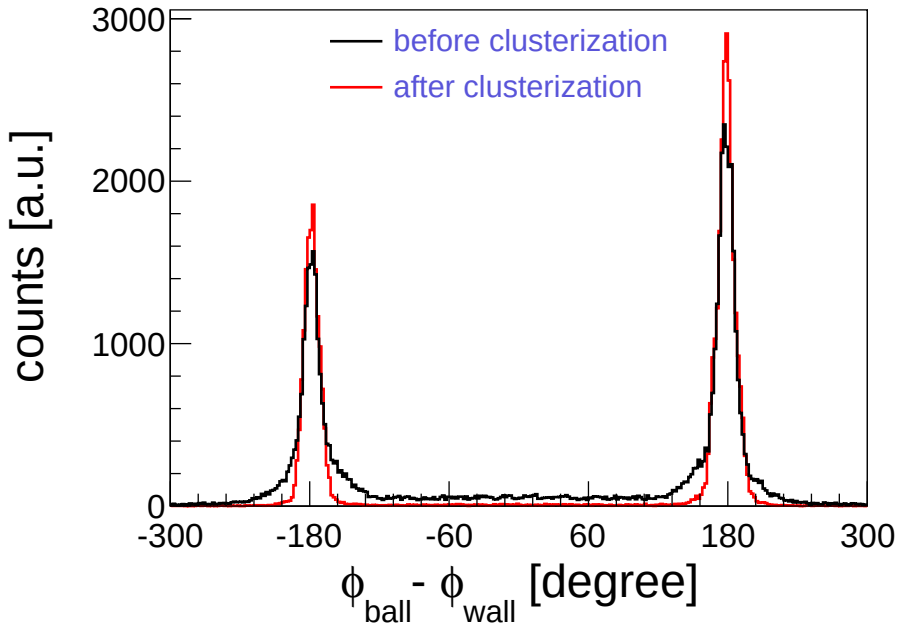

FIGURE 4.16: The distribution of elastically scattered wall-ball coincident deuterons is presented as a function of their relative azimuthan angle. The peaks are centered around ±180° and the width of the peaks represents the angular resolution of the detector. Clusterization (the red curve) led to an improvement in the angular resolution as compared to analysis performed without clusterization (the black curve).

One assumes that the particle is detected in the element with largest energy. Sum of the energies in the two ball elements is found smaller compared to the energy expected by the dd elastic kinematics. This difference is accounted for the energy lost in the surface between the two ball element. In principle, each element having 12 neighbors at most, it would be a tedious task to obtain the α coefficient for the surface between every two adjacent ball elements. However, Study shows that in most part of the ball, the α coefficients are about 10%.

After applying the angle reconstruction based on the cluster information (Eq. 4.4 and Eq. 4.3), the distribution of the relative azimuthal angle (see Fig. 4.16) and polar angles (see Fig. 4.18) were obtained. The resolution is significantly improved when comparing to the reconstruction method based only on a single ball element. To test this method with respect to the energy reconstruction, the wall-ball energy kinematical relation for the *dd* elastic scattering process was drawn (see Fig. 4.19). The events group along the calculated kinematics.

Since the most basic variables which characterize the particle are reconstructed far better when using the clusterization method, thus this approach was used in the further analysis. The estimated overall energy resolution in the ball is about 10-20%.

The clusterization method is less accurate when the reconstructed clusters lie at the edge of the ball's acceptance (and near the target holder entrance) as well as it can contain an element with no response ("dead" element). The light in such situation is not completely recovered and the energy and angular resolution is diminished.

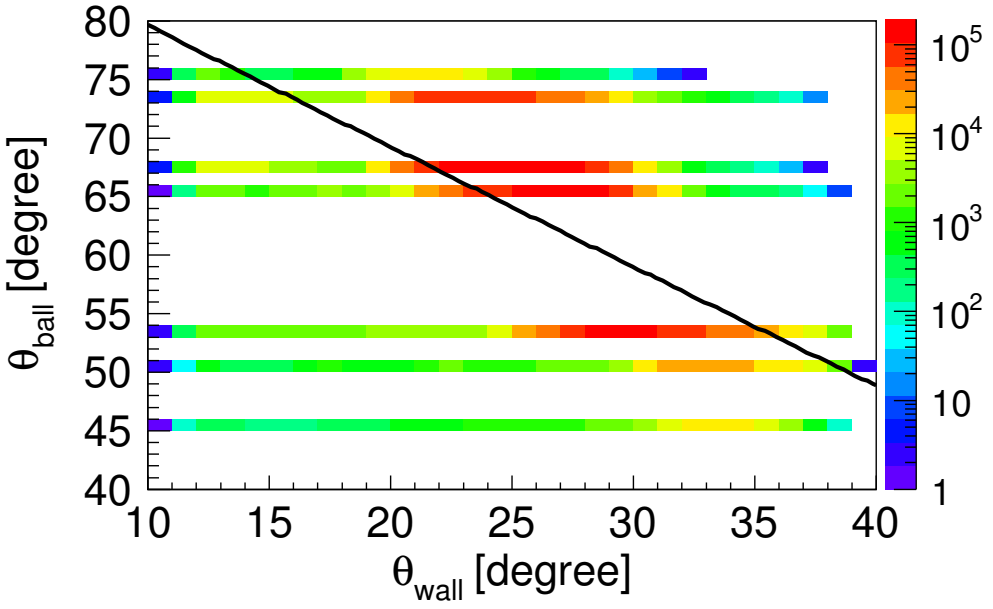

FIGURE 4.17: A correlation between polar angles of wall (θ_{wall}) and ball (θ_{ball}) is presented for the wall-ball coincident events. The horizontal bands are manifested by the ring and subring structure of the ball elements as explained in the Fig. 4.15

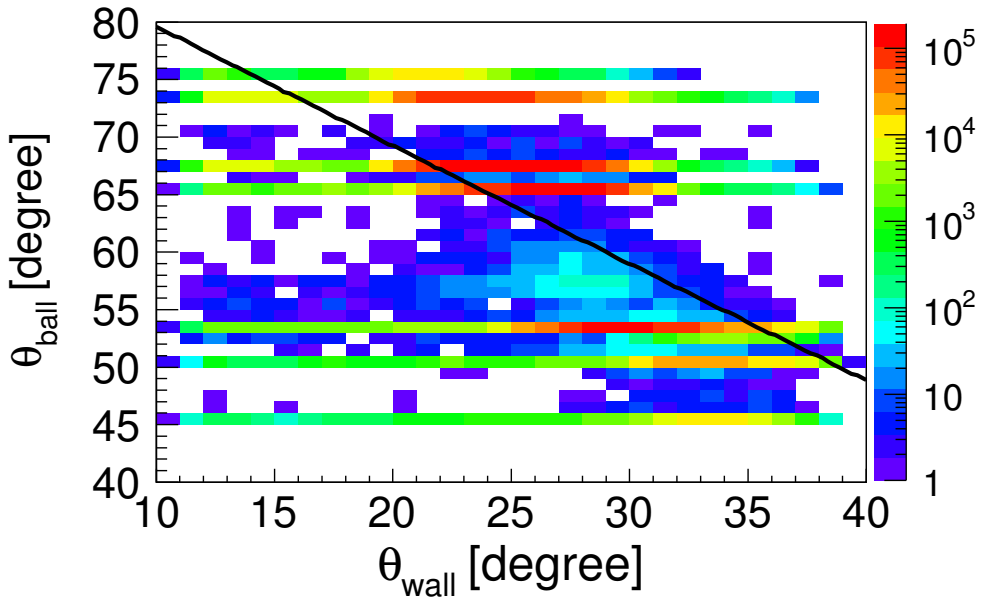

FIGURE 4.18: The same as Fig. 4.17 but after applying clusters. One can notice that the cluster method give more realistic angular distribution for most of the events, filling the empty gaps between the rings (and sub-rings) of the ball elements.

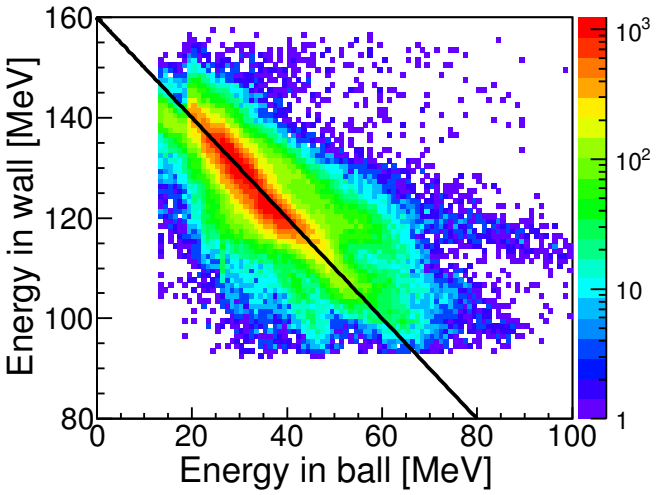

FIGURE 4.19: The wall-ball energy correlation for the *dd* elastic scattering reaction. The black line refers to the calculated kinematics.

4.5 Discrimination of reaction channels

Elastic dd scattering and dp-quasifree process: To discriminate the elastically scattered deuterons registered in wall from the breakup ones, additional cuts were imposed on the energy (seen as vertical dashed line) within the "d gate" as shown in Fig. 4.5, right panel. To calculate a number of elastically scattered deuterons — to be used further for the normalization purpose (see Sec.4.7), a careful background subtraction was performed as described in Sec.4.6. In case of the wall-ball *dd* coincidences, applying the additional co-planarity condition (i.e. cut on the relative azimuthal angle $|\Delta\phi - 180°| < 10°$), lead to a suppression of the breakup contamination (see Fig. 4.20,

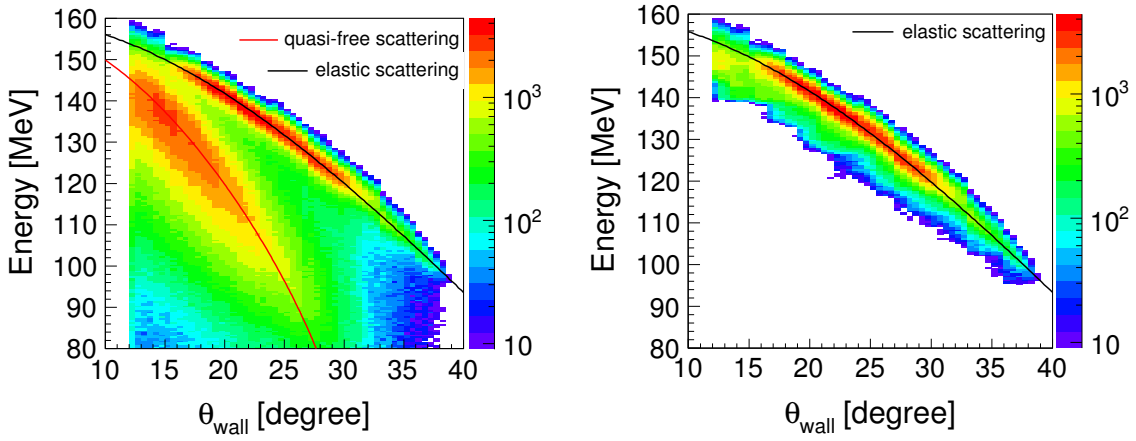

FIGURE 4.20: The wall-ball coincidences with deuterons selected in wall; left panel shows the deuterons full-filling the co-planarity condition. The elastically scattered and QFS deuterons are easily distinguished. Right panel presents the same spectrum but with the cut applied to the elastically scattered deuterons.

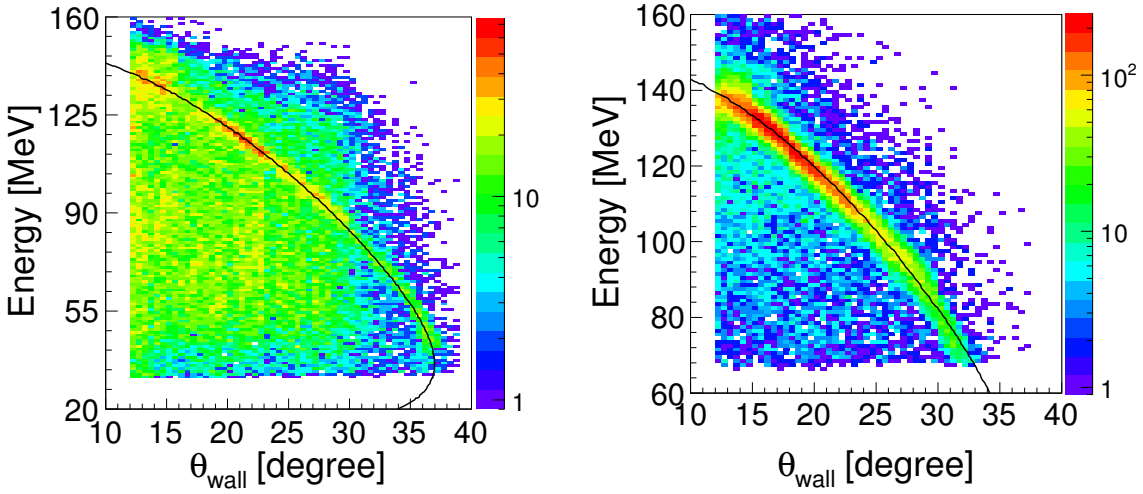

FIGURE 4.21: The kinematical spectra of the transfer reactions are presented for the ^3H (left panel) and ^3He (right panel) particles. The solic black lines represent the calculated kinematics.

right panel). However, due to low efficiency of the ball detectors (see Sec. 4.6.4) this condition was not further used for luminosity determination (normalization).

The quasi-free three-body process (QFS) was also identified within the co-planar wall-ball coincidences. As it is seen in Fig. 4.20, the deuterons coming from dp-quasifree process are spread over a wide band around the calculated dp kinematics. This broadening is due to the fact that the spectator neutron caries some minimum energy. Therefore one can study the QFS process as a function of energy of the spectator neutron (see Section 4.7).

Transfer reactions: In case of the transfer reactions (see Sec. 2.5), charecterized with low cross section (in comparison to the elastic and breakup process) the amount of observed particles was small. The cross-section (and the kinematics) of both the transfer reactions is comparable, therefore one expects to observe the same amount of ^{3}H and ^{3}He particles in a given telescope.

The ^3He particles were found well separated due to their relatively large energy losses in ΔE detector whereas the ^3H particles were lying very close to the branch of the breakup deuterons and therefore it was difficult to separate them. Particle identification gates were also applied for these heavier particles and after applying the calibration agreement with calculated kinematics was checked, see Fig. 4.21.

One can notice that the energy threshold for ^3He is very large, about 70 MeV, whereas for the ^3H it is of about half, that is 35 MeV. The ^3He nucleus has twice the electric charge of the ^3H, and according to the Bethe-Bloch formula, the energy loss of a charged particle in ionizing medium is in proportion to the charge of that particle. The mentioned above analysis is based on PID, with no requirement of coincidence. However, in case of the neutron transfer channel, it was possible to register both, the wall-wall and the wall-ball coincidences. Whereas in case of proton transfer channel only the single track of ^3He in wall were considered[4].

[4]Due to small efficiency of neutron detection in ball, the wall-ball coincidence was also observed in

4.6 Detector efficiency

In order to obtain absolute values of the breakup cross section, it is necessary to take into account efficiency of the detection system. Depending on the type of the detected particle, proton or deuteron, corrections were done separately. Determining the BINA detector efficiencies is a procedure of finding scaling factors for the obtained number of the breakup coincidences $N_{br}(S,\Omega_d,\Omega_p)$, registered at the angles $\Omega_d = (\theta_d, \phi_d)$ and $\Omega_p = (\theta_p, \phi_p)$, where θ_d, θ_p, ϕ_d, ϕ_p correspond to the scattering angles of the coincident particles. One can distinguish between a hardware and a geometrical efficiency.

In the first case, probability of detecting a charge particle is connected with an efficiency of each element of the detectors: wall (MWPC, ΔE, E) and ball. Certain detector elements became inefficient i.e. they function with lower efficiency or cease to function at all ("dead" wires/elements), what can cause quite a significant effect. In case of the scintillator hodoscopes, the inefficiencies also occur if a charged particle escape through the gap between two adjacent scintillators (in ΔE hodoscope)or deposits its energy in both of them (in the E hodoscope).

In case of the geometrical efficiency, one can count a so-called "configurational inefficiency". If both charged particles (a proton and a deuteron) coming from the breakup reaction $dd \rightarrow dpn$) hit the same E-bar or ΔE strip, its not possible to distinguish between their signals and have proper energy information so the event is rejected. Size of the effect is strongly dependent on the angular configuration of the two particles.

The above effects can affect the measured angular distributions causing sometimes large fluctuations. In order to eliminate and compensate their role, efficiency maps in θ, ϕ co-ordinates, reflecting the correction factors, were calculated for the wall and ball components separately. In each case a common binning size was set to 1° and 5° in θ and ϕ angles, respectively. Finally the total efficiencies were calculated.

4.6.1 MWPC efficiency

The charged particles passing through the MWPC detector induce signals in wire-planes. If the signal is below certain threshold or does not appear at all, such event is counted for inefficiency of that wire-plane. The efficiency varies across the active area of MWPC. The maps of individual planes were obtained and the total efficiency was calculated as a product of the efficiencies of all the three wire-planes.

The efficiency of the given plane was found by determining θ and ϕ angles from hits in the two other planes and checking, if the corresponding hit in the plane of interest is present. Such a procedure was performed by counting the number of events in the angular segments of $\Delta\theta = 1°$ and $\Delta\phi = 5°$ (standard granularity to be used also in subsequent sections of rest of the detector efficiency). Only the single particle events were taken into account (maximum one hit in each plane, one hit in ΔE and one hit in E). The probability of registration of a particle in a given MWPC plane, for example in the x-plane, for a given angular segment is:

$$\epsilon_x(\theta,\phi) = \frac{N_{xyu}(\theta,\phi)}{N_{xyu}(\theta,\phi) + N_{yu}(\theta,\phi)} \tag{4.6}$$

the proton transfer channel. This may be useful, in future, to find neutron detection efficiency of ball by knowing the wall-ball coincidence.

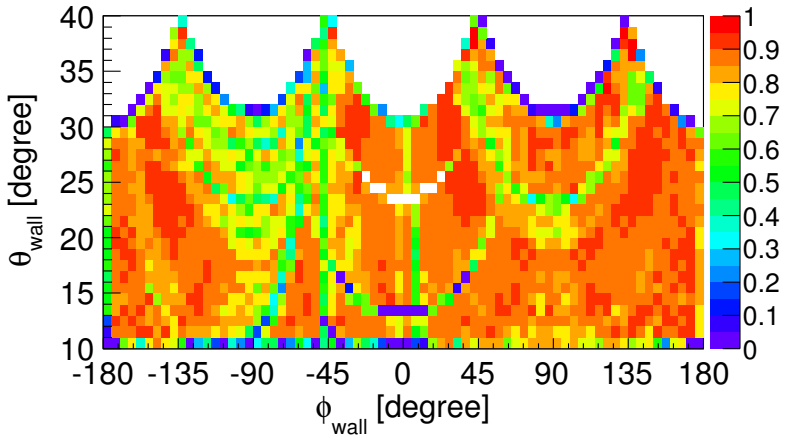

FIGURE 4.22: Efficiency map of MWPC. The elliptic like structure illustrates the "dead-wires".

where $N_{xyu}(\theta,\ \phi)$ is a number of events registered in a given angular bin $(\theta,\ \phi)$ in the three planes, whereas $N_{yu}(\theta,\ \phi)$ is a number of events, registered in this bin, but with at least one wire hit in plane y and one in plane u. The efficiencies of y and u planes were calculated in the similar way. The total MWPC efficiency was obtained by multiplication of the probabilities for particle registration in the individual planes:

$$\epsilon_{xyu}(\theta,\phi) = \epsilon_x(\theta,\phi) \cdot \epsilon_y(\theta,\phi) \cdot \epsilon_u(\theta,\phi) \tag{4.7}$$

Fig. 4.22 shows the efficiency map for the whole MWPC detector. Due to the square shape of MWPC the range of polar (θ) angle between 30° and 40° is only partially covered in azimuthal angle ϕ (see empty region). One can notice the broken ("dead") wires seen as low intensity areas. The method does not work for two crossing dead wires in two planes, such bins on the efficiency map were completely rejected and were corrected for with additional Monte Carlo simulations. The MWPC efficiency is generally above 95%, but in some regions it falls down dramatically to about 70%. The MWPC efficiency was determined within statistical accuracy of 0.2%.

4.6.2 ΔE scintillators:

The efficiency for ΔE was obtained in a similar way as in the case of MWPC, taking the MPWC and E-detectors as reference counters. If a particle was registered in MWPC and the E-detector but not in ΔE then such event was counted for inefficiency of the ΔE detector. The inefficiency is mainly due to two reasons: the ΔE scintillators are very thin and a fraction of high energy charged particle may transmit through the ΔE detector without leaving enough energy to be registered or the particles may pass through the gap between two ΔE strips. An efficiency map of ΔE was calculated with the standard granularity and is presented in Fig. 4.23. As one can see, the efficiency in most of the area of the map, excluding the detector borders, is almost 100%. The statistical accuracy of the ΔE efficiency was found to be 0.15%.

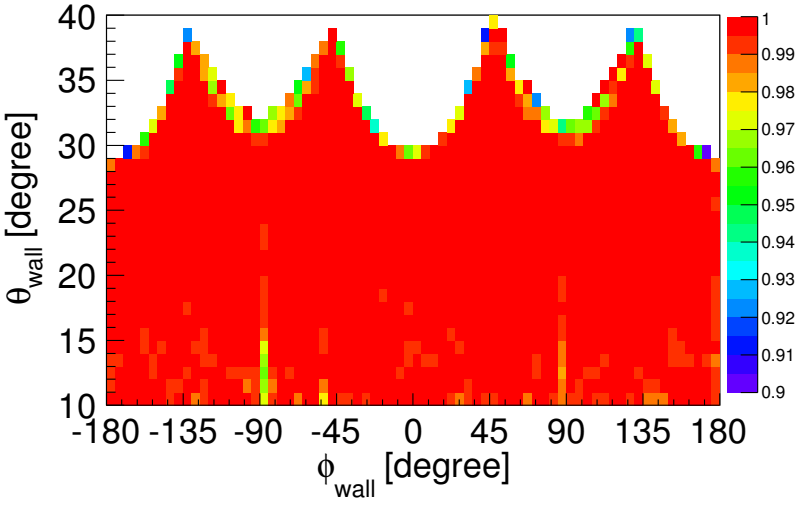

FIGURE 4.23: Efficiency map of the ΔE transmission detector.

4.6.3 E scintillators:

To establish the E-detector efficiency, one has to count for two different effects whose magnitude, in some case, can significantly reduce the detector efficiency; these are the so-called "cross-over effect" and the "configurational effect".

The cross-over events are present when a charged particle is registered in the two adjacent E-scintillators. Such events were rejected from the analysis and were compensated by simulating the effect. A sample distribution of the cross-over events can be seen in Fig. 4.24, obtained using the GEANT4 simulation for the elastically scattered deuterons. The inefficiency due to cross-over were found at most 1%.

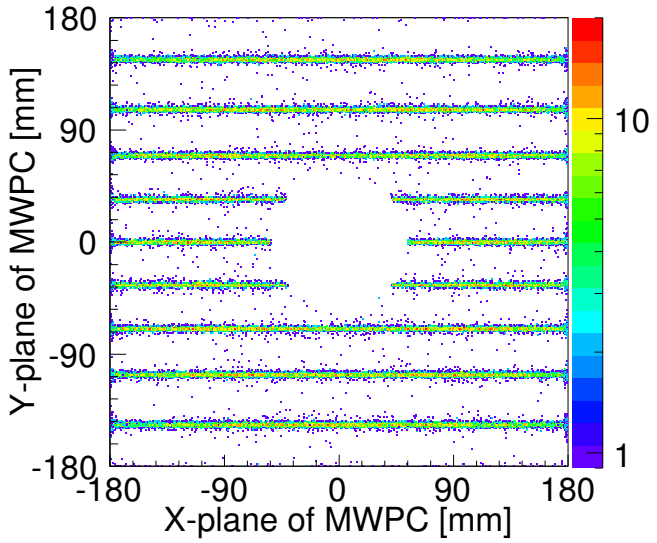

FIGURE 4.24: Cross-over events, obtained from the GEANT4 simulation, shown as a function of XY wire-planes.

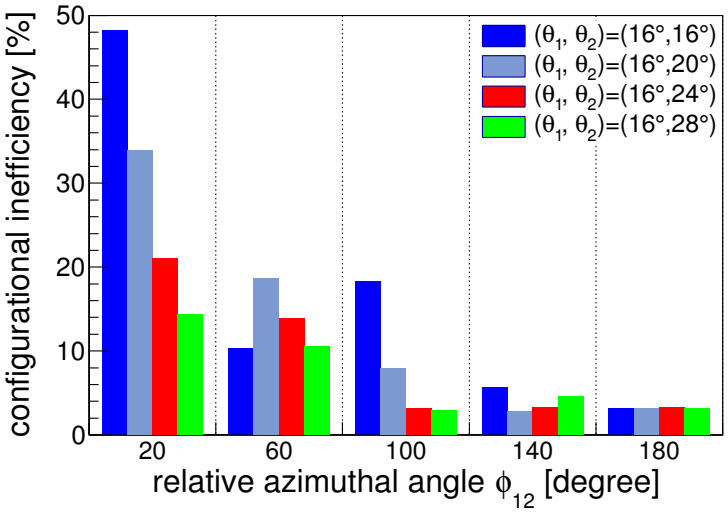

FIGURE 4.25: A bar chart representing the inefficiency for 20 different breakup configurations. In general, the inefficiency increases with decrease in the spatial distance between the two outgoing particles.

The configurational inefficiency has influence only in the case of the breakup $dd \rightarrow dpn$ process. To correct for this effect, the number of breakup coincident events for each analyzed configurations were counted. For the same set of breakup configurations, GEANT4 simulations were performed and fraction of the breakup coincidences, with proton and a deuteron registered in the same E-detector, was obtained. Then corresponding correction factors were calculated. The configurational inefficiency was found large for the configurations with a small relative azimuthal angle ϕ_{dp}. For example at ϕ_{dp}=20° the inefficiency reached to almost 50% and by increasing ϕ_{dp}, its magnitude became smaller reaching below 5% in the case of the co-planar configurations and all other configurations analyzed within this work, i.e. with ϕ_{dp} = 140° and 160°. The statistical uncertainties, in both the above mentioned inefficiencies, are within 0.1%.

4.6.4 Ball efficiency

The ball efficiency was calculated with the use of the elastically scattered deuterons and information from the wall detector like the particle identification and energy cut imposed on elastic peak. To find the efficiency, the single track deuterons were counted (N_{wall}) under the mentioned constraints on wall. Having the energy and momentum of this first deuteron registered in wall and knowing kinematical relation for the dd scattering, one can verify the information of the second deuteron in ball. Then number of the elastically scattered deuterons was counted in the case when both deuterons were detected as a wall-ball coincidence ($N_{wall-ball}$). In the latter case, additional co-planarity condition was applied as $\Delta\phi$=10°. The probability of registration of a particle in ball for a given angular segment was then calculated with the following formula:

$$\epsilon_{ball}(\theta,\phi) = \frac{N_{wall-ball}(\theta,\phi)}{N_{wall-ball}(\theta,\phi) + N_{wall}(\theta,\phi)} \tag{4.8}$$

Fig. 4.26 presents the efficiency map obtained for the ball detector with the standard

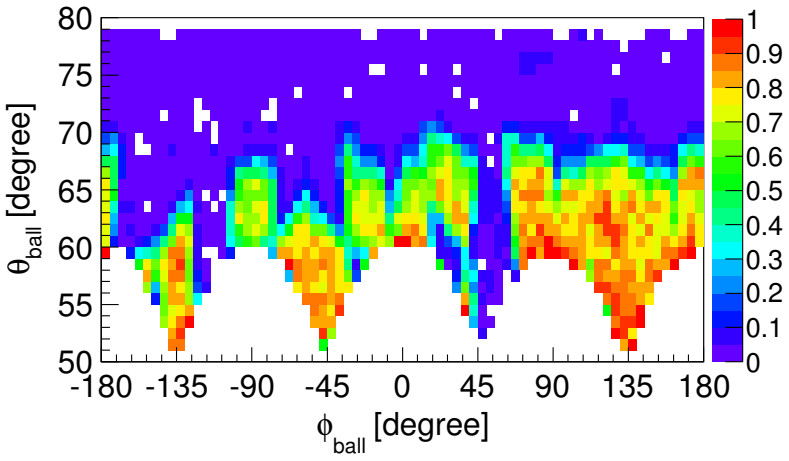

FIGURE 4.26: Efficiency map of ball. The broken or not working ball elements are visible in inefficient triangular regions below $\theta_{ball} = 70°$.

binning size. One can notice the target shadow (as explained in Sec. 4.4.2) and the broken ("dead") ball elements. Due to the kinematical reasons, the efficiency becomes almost zero above θ=70°. The deuterons above this angle have very low kinetic energy and, therefore, are stopped before reaching the ball detector. The statistical uncertainty in this case was found at most 0.28%.

4.7 Analysis of elastic scattering process

Due to kinematic relations, it is not possible to detect both the deuterons from the elastic scattering (as explained in Sec. 2.3.1) in wall; one of them is always emitted at the angle corresponding to the acceptance of ball. The analysis presented in Sec. 4.6.4 reveals rather low ball efficiency, so the number of wall-ball coincidences is reduced and burdened by high systematic uncertainty due to the ball efficiency correction. Therefore, in order to obtain the number of elastically scattered deuterons with a good statistical accuracy, the selection of deuterons was done based on wall information only. That is, the particle is identified as deuteron and, it has no coincident particle in wall, though another particle may (or may not) be registered in ball; let's call this selection rule as "single track in wall". The single tracks in wall assure that all the deuterons from elastic scattering are selected and the deuterons coming from wall-wall coincidence of $dd \rightarrow dpn$ breakup are rejected which otherwise would give a large background. Final selection relies on the deposited energy, as explained in the following section. One has to cope with the remaining background, largely due to the deuterons coming from wall-ball coincidences of the breakup reaction.

4.7.1 Background subtraction and calculation of normalization factor

The counts for elastically scattered deuterons, are obtained after careful subtraction of the background deuterons coming from the $dd \rightarrow dpn$ breakup process. An exclusive distribution of single track deuterons, registered in the forward wall at three different θ angles, is presented in Fig. 4.27. A sharp peak due to the elastically scattered deuterons can be seen at the highest energy region of each distribution (marked with "1"). The peak is contaminated by the background of the deuterons originating from the $dd \rightarrow dpn$ breakup process which is spread over the entire energy range. Depending on the scattering angle, the amount of background varies. Moreover two broader peaks

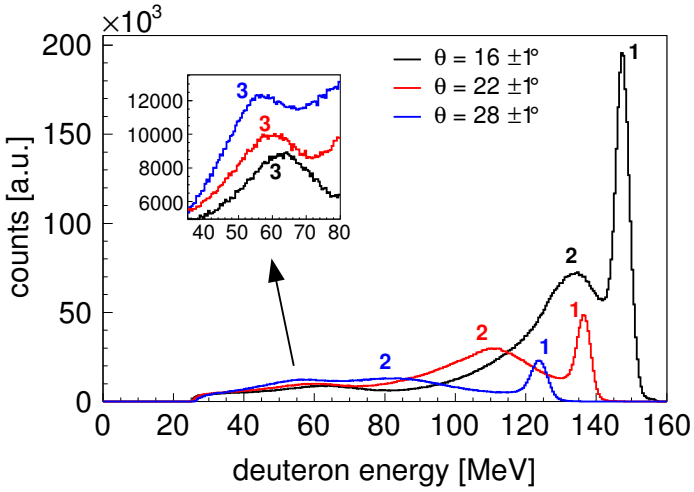

FIGURE 4.27: Energy distribution of the deuterons detected in wall, at three different θ angles, is presented. Refer to the text for the details.

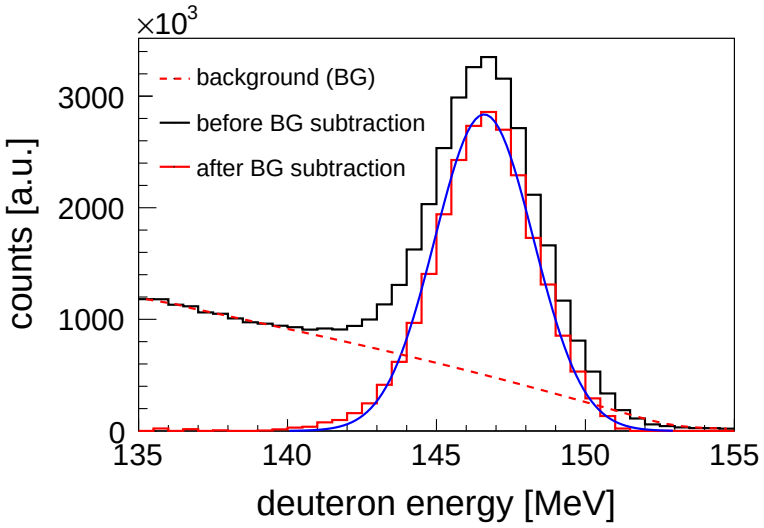

FIGURE 4.28: Background subtraction method presented on sample energy spectrum obtained for deuteron scattering angle θ=16.5±0.5°. The distribution obtained after the background subtraction (red line) is fitted with a Gaussian (blue) whose mean value is found 146.60±0.0003 MeV which is consistent with the value of 146.59 MeV resulting from kinematic relations.

contribute to the spectrum (marked with "2" and "3"). The second peak is dominated by *dp-quasifee* process (the target deuteron is disintegrated). The peak marked with "3" (see inset of the figure) contains events from the *pd-quasifee* process (the beam deuteron is disintegrated). The background was subtracted with the use of Statistics-sensitive Non-linear Iterative Peak-clipping (SNIP) algorithm [82], see Fig. 4.28. Due to the reason that the exact shape of the background is not known, the simplest linear one was assumed. Reliability of the applied algorithm was confirmed by comparing the peak position (obtained by fitting a Gaussian) with the theoretically calculated values at the given scattering angle.

4.7.2 Cross-section scaling

During the experiment, it was not possible to have a reliable beam current measurement. Therefore the obtained distributions of elastically scattered deuterons were scaled to the existing precise experimental data of nearest energies, from BBS experiment [40].

First, the number of elastically scattered deuterons, obtained after the background subtraction, was corrected for various efficiencies of detection system, see Sec.4.6 and Fig.4.29. Next, the corrected distribution was transformed to the center-of-mass system and, subsequently, presented as a function of the four-momentum transfer (q) which is square root of absolute value of the Mandelstam variable (t) and it is given as follows:

$$q = \sqrt{|t|}, \quad where, \; t = 2p_{1cm}^2(\cos\theta_{1cm} - 1) \tag{4.9}$$

and p_{1cm} (θ_{1cm}) is the momentum (scattering angle) of the deuteron in the center-of-mass frame. A detailed study of four-momentum transfer for the few-nucleon system can be found in reference [41]. When presenting the cross-section distribution as a

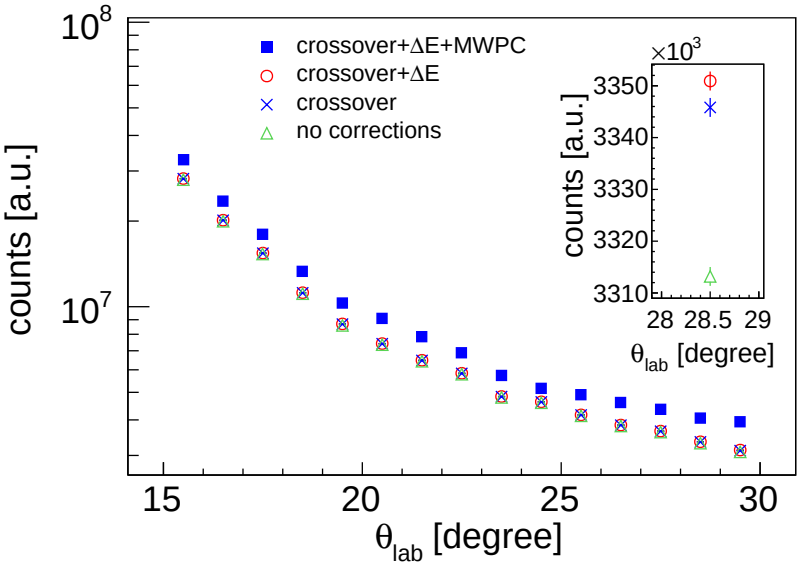

FIGURE 4.29: The distribution of elastically scattered deuteron as a function of its polar angle θ is presented before and after applying various efficiency corrections.

function of q, one finds a scaling region where the distributions at different beam energies overlap. Such an effect suggests simplicity of the reaction mechanism in which the

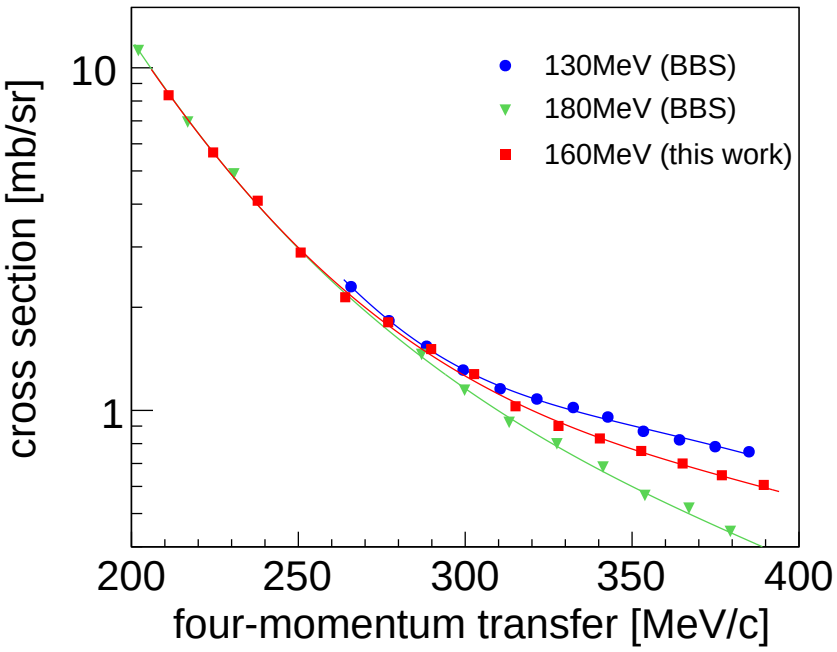

FIGURE 4.30: Cross section for 160 MeV is shown after scaled to the existing data from BBS-experiment at 180 MeV. The BBS data are taken from [40]

dynamical part of the scattering cross section predominantly depends on q regardless of the reaction energy. Benefiting from this fact, the entire distribution of 160 MeV data was scaled to the existing BBS data at 180 MeV, in the scaling region below q=250 MeV/c (see the Fig. 4.30). To this end a function y=f(q) — in the form of a polynomial of rank-7 multiplied with an exponential (i.e. "pol7*expo" function in the ROOT framework) — was fitted to the data measured at 180 MeV, with a reduced χ^2=4.45, and the following parameters were obtained:
a_0=7.98±0.46
a_1=(-3.09±0.15)×10^{-02}
a_2=(-1.53±0.83)×10^{-04}
a_3=(7.06±3.27)×10^{-07}
a_4=(1.89±0.89)×10^{-09}
a_5=(-4.74±2.34)×10^{-12}
a_6=(-2.90±1.44)×10^{-14}
a_7=(7.99±3.43)×10^{-17}

The resulting function was multiplied by a scaling factor k_{scale} treated as the only free parameter of the function y=k_{scale}×f(q), which was fitted to the distribution of elastically scattered deuterons of this work. As the result, the parameter where k_{scale} was found to be:

$$k_{scale} = 33870122 \pm 475679 \ [counts/mb] \tag{4.10}$$

The obtained scaling factor is used in the next section for the normalization of the breakup cross section. Note that k_{scale} account for the experimental conditions such as beam current, target thickness etc.

4.8 Breakup reaction analysis

4.8.1 Evaluation of breakup coincidences

In order to obtain the breakup cross section for a given angular configuration, (θ_d, θ_p, ϕ_{dp}), the number of counts of deuteron-proton coincidences, corrected for the detector efficiencies, are projected onto the corresponding theoretical kinematics, see Fig.4.31.

The convention for selecting S=0 point and the S-curve direction is defined in Sec. 2.3.2. The S-curve is divided into segments of equal width ΔS (4 MeV) along its length and each event is ascribed to one ΔS segment according to its closest point on the kinematics. Farther, a new variable D is introduced (see Fig. 4.32) as a signed distance of the event to the kinematical curve, with events from inside (outside) the kinematics having negative (positive) distance.

For each ΔS segment, counts of the breakup coincidences are projected onto the D-axis, as shown in Fig.4.32. One expects the obtained distribution along D-axis to be centered around D=0 and its tail distribution on the D<0 region may carry background of accidental coincidences. Since the exact form of this background is not known, as a first approximation, we take it of the wedge-like (decreasing as moving from -D to +D) shape as presented in Fig.4.32. The counts obtained after the background subtraction, for each ΔS, are then normalized using Eq. 4.11.

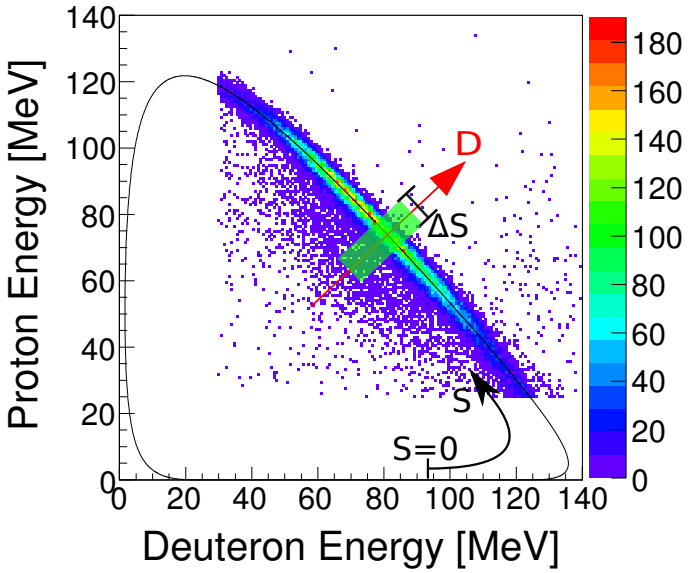

FIGURE 4.31: A sample breakup kinematics for chosen angular configuration ($\theta_d = 18 \pm 1°$, $\theta_p = 22 \pm 1°$, $\phi_{dp} = 180 \pm 5°$) is presented. Shadowed area represents one ΔS bin (for definition of S see Section 2.3.2) with the D-axis perpendicular to a segment ΔS and representing distance of a data point from the kinematical curve; for details see the text.

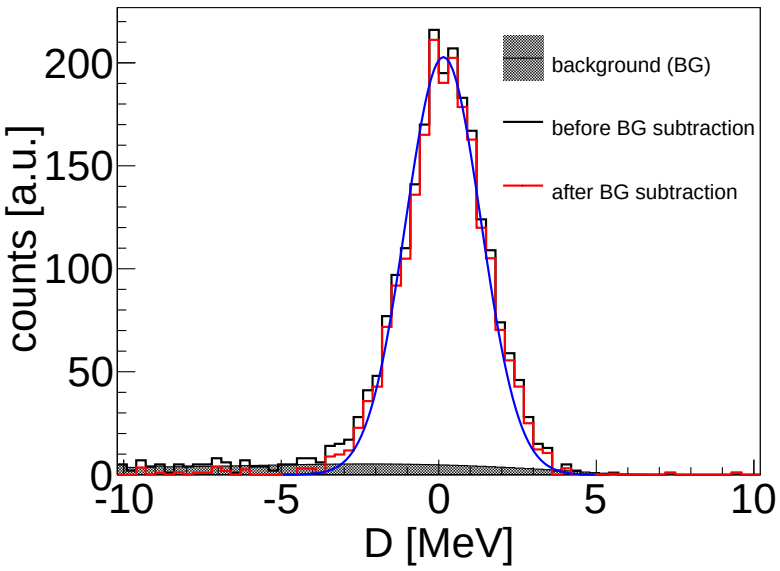

FIGURE 4.32: Distribution of events in a function of the D variable obtained in a chosen ΔS segment (see Fig.4.31). The background subtraction is done with the help of SNIP algorithm [82]. The obtained distribution, after subtraction, was fitted with a Gaussian.

4.8.2 Three-body breakup cross-section

Since the measurement of the $dd \rightarrow dpn$ breakup and the dd elastic scattering were done simultaneously, one can profit from the fact, that the factors such as beam current, thickness of the target or dead-time are identical. Therefore, the differential cross section of breakup process is normalized relatively to the elastic scattering process. Explicit formula for both these quantities are given in the Appendix B. The differential cross section of the breakup process can be expressed as follows [18]:

$$\frac{d^5\sigma}{d\Omega_d d\Omega_p dS}(S,\Omega_d,\Omega_p) = \frac{d\sigma_{el}}{d\Omega_d}(\Omega_d) \cdot \frac{\Delta\Omega_d^{el}\epsilon^{el}(\Omega_d^{el})}{N_{el}(\Omega_d)} \cdot \frac{N_{br}(S,\Omega_d,\Omega_p)}{\Delta\Omega_d\Delta\Omega_p\Delta S} \cdot \frac{1}{\epsilon(\Omega_d)\epsilon(\Omega_p)}, \quad (4.11)$$

where,
N_{el} is the number of the elastically scattering deuterons registered in the solid angle Ω_d^{el},
N_{br} is the number of of the deuteron-proton coincidences from the three-body breakup process registered at solid angles Ω_d, Ω_p and within a ΔS-wide arc-length bin,
$\epsilon(\Omega_i)$ is position dependent total detector efficiency for the breakup particles in the wall (subscript i stands for d or p.).

Note that the first two terms — the elastic cross section and the inverse of counts for elastic events, corrected over efficiencies and solid angle — can be replaced by the scaling factor k_{scale} and then the equation Eq.4.11 reduces to the following:

$$\frac{d^5\sigma}{d\Omega_d d\Omega_p dS}(S,\Omega_d,\Omega_p) = \frac{1}{k_{scale}} \cdot \frac{N_{br}(S,\Omega_d,\Omega_p)}{\Delta\Omega_d\Delta\Omega_p\Delta S} \cdot \frac{1}{\epsilon(\Omega_d)\epsilon(\Omega_p)} \quad (4.12)$$

Total of 147 breakup configurations were analyzed and the obtained breakup differential cross sections are presented in Ch. 5. Since the calculations, the data are compared with, are relevant "near QFS", the geometries close to co-planar (i.e. with $\phi_{dp} = 140°$, 160° and 180°) have been analyzed.

4.9 Possible sources of uncertainty

Two types of uncertainties influence the obtained breakup cross sections — the statistical and the systematic one. The first one arises mainly due to the error in the number of counts obtained for the the elastic scattering (Section 4.7) and for the breakup coincidences (Section 4.8), with a negligible contribution of the statistical uncertainties of the detection efficiency (Section 4.6). The typical statistical uncertainty of the cross section (where a typical value is 0.2 mb$\cdot$ sr$^{-2}\cdot$ MeV^{-1}) for breakup configurations, with $\phi_{dp} = 160°$ and 180°, is about 1.2%. It varies between 1% to 5%. Due to its relatively low value (typically 0.03 mb$\cdot$ sr$^{-2}\cdot$ MeV^{-1}) the cross section measured in breakup configurations with $\phi_{dp} = 140°$ has larger statistical uncertainty of about 3.5%, varying between 2% to 8%.

The systematic uncertainties were largely reduced via careful pre-sorting of the data (as explained in the Section 4.2) and study of the detection system geometry (as discussed in [18]). The remaining systematic uncertainties, due to various possible effects, were estimated and are briefly discussed below:

1. Particle identification

   Various types of particle were identified via defining graphical cuts (i.e. "d gate" and "p gate" as shown in Fig. 4.5) enclosing the branches/spots on the ΔE-E spectra. A finite precision in defining such gates may lead to mixing of particle types, i.e. protons can be identified as deuteron and vice versa (see Fig. 4.34), or cutting out a part of useful events. The systematic uncertainty associated with this process was estimated by repeating the analysis based on slightly modified gates (moving the line separating protons from deuterons by 18 channels (in ΔE)

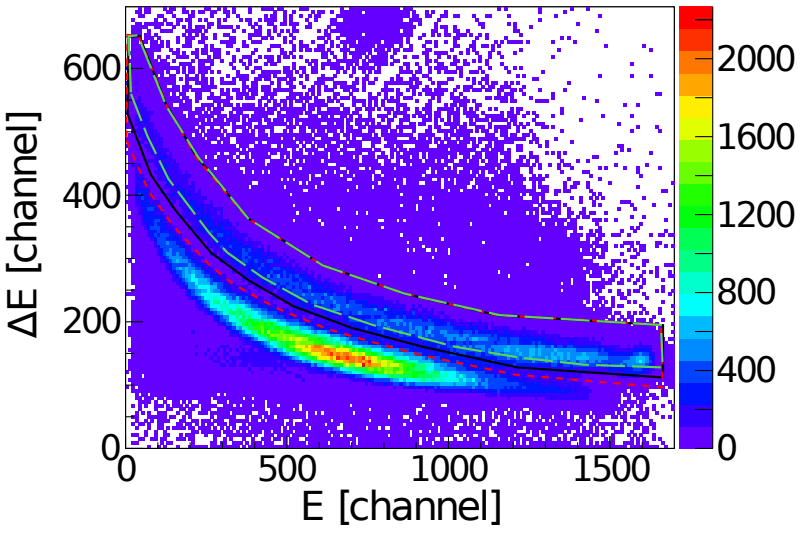

FIGURE 4.33: An example of particle identification gates applied to select deuterons, presented for sample ΔE-E telescope. The solid (black) line corresponds to the original gate (graphical cut) used to obtain the final results. The gate presented in long-dashed green (short-dashed red) line were used for the purpose of error estimation in the final results.

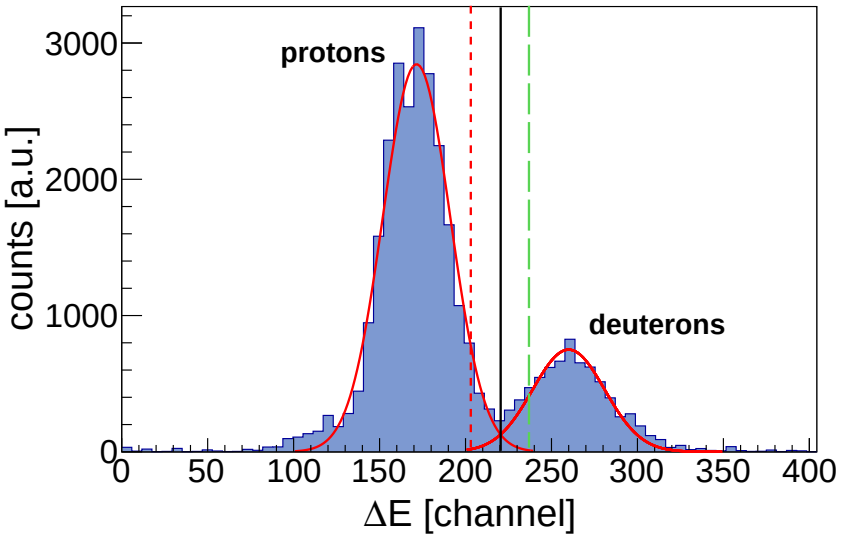

FIGURE 4.34: Illustration of mixing of particle types: events presented in Fig. 4.33 in one energy bin (here E=500 channel) have been projected onto ΔE axis. The resulting peaks, marked with the identified particle types (i.e. protons and deuterons), are fitted by Gaussian distribution and their overlap is accounted for the amount particle mixing.

up and down, see Fig.4.33) and calculating the relative difference of the resulting cross-section value. The typical uncertainty related to this effect, on the final cross sections, was found not more than 5%.

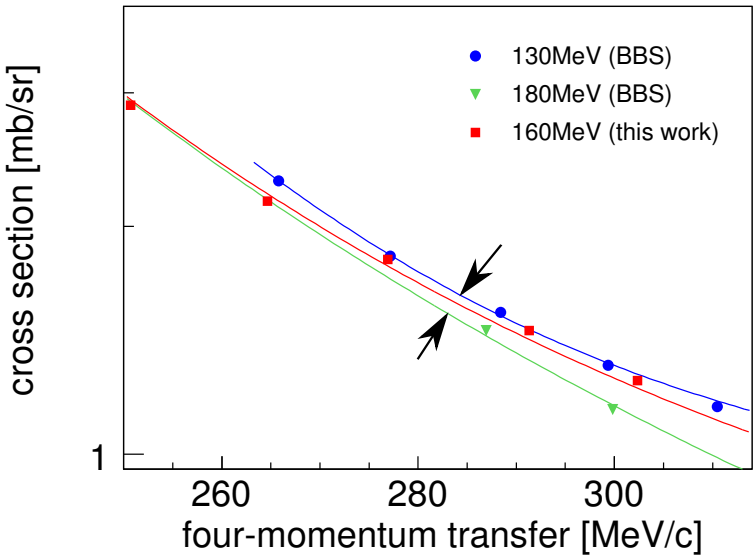

FIGURE 4.35: Zoom of Fig. 4.30: the region between two black arrows indicates the separation of two BBS data sets slightly above the scaling region. Assuming that the 160 MeV data should lie within this limit, the arrows indicate the systematic uncertainty of the scaling procedure.

2. Absolute normalization

   The obtained distribution of elastically scattered deuterons was normalized to the 180 MeV BBS data set in the scaling region (characterized with low four-momentum transfer(q))— see Section 4.7.2. In the scaling procedure, we assume that the cross section at different beam energies coincide (as shown in Fig.1.4), showing almost energy independent behaviour of the dynamics. The scaling is not necessary exact, so the possibly close energy was chosen. For the control, the lower energy of 130 MeV could be used, however, the BBS data at 130 MeV, measurement during the same experiment as 180 MeV, have no data point in the scaling region. Therefore, the region slightly above the scaling was chosen and it was assumed, that the curve for 160 MeV should be placed between the curves for two BBS data sets (see Fig. 4.35) and the uncertainty of the scaling factor k_{scale} was determined. The uncertainty in the final cross section, associated, with the choice of scaling region, was estimated to be of 2.9%. This value is further affected by the uncertainty in the BBS data, which is quoted to be 5.02 % in reference [40].

3. Reconstruction of the scattering angles

   The reconstructed emission angles (θ and ϕ) of a detected charged particle can be affected by various factors. One of them is the discrete information from MWPC (i.e. finite 12 mm spacing between MWPC planes and the wire-spacing of 2 mm in each plane). This results in a limited angular resolution which varies across the MWPC plane. The resolution in θ is about 0.5° at $\theta = 10°$ which decreases with increasing θ, reaching the resolution of about 0.3° at $\theta = 30°$. The resolution in ϕ depends on θ and varies between 0.6° and 2.3°. The angular resolution is relatively small compared to the chosen angular ranges applied in defining kinematic configurations and hence the influence of angular uncertainty on the final results is negligible. The other factors that can affect the reconstructed angles, with the assumption of the point-like source, are the finite target thickness (about 6.6 mm) and size of the beam spot on the target (about 3 mm in diameter). The spread associated with the reconstructed angles in the breakup cross section was estimated to be of maximum 1%. The beam position on target and target to MWPC distance were checked on the basis of dp elastic scattering kinematics measured in the run with LH_2 target and absolute value of the θ was controlled within precision better than 0.3° [79].

4. Background subtraction

   The amount of background in case of breakup coincidences was found negligibly small (See Fig. 4.32) and therefore the associated systematic uncertainty was neglected. However, the background contribution in case of the elastic scattering process was large and its subtraction procedure could have been a source of significant systematic uncertainty. One way to estimate the amount of this systematic error is to look at the difference in number of counts obtained in case of "single track in wall" and in case of the wall-ball coincidences, much less affected by background. To do this, first a ball element with a good detection efficiency is chosen and the events corresponding to wall-ball coincidences with that particular element are selected. For those events the deuteron energy distribution is

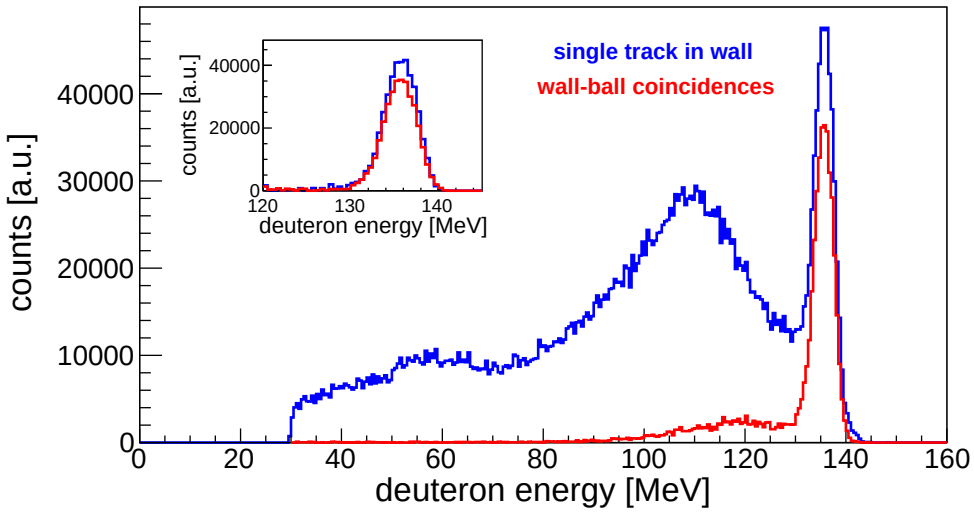

FIGURE 4.36: Comparison of the number of counts for "single track in wall" (blue) to the "wall-ball coincidences" (red), for ball element 47 and solid angle in wall (θ = 22±1°, ϕ =−7±5°), is presented as a function of deuteron energy. Inset shows the same comparison after applying the background subtraction procedure as described in Sec. 4.7.1.

built. The solid angle for particles registered in wall ($\Delta\theta$,$\Delta\phi$) is chosen in such a way that the corresponding solid angle of second deuteron (originating from dd elastic scattering) lies withing the chosen ball element. Then the "single tracks in wall" (as described in Section 4.7) are obtained for the same solid angle ($\Delta\theta$,$\Delta\phi$). This procedure was performed for seven different well working ball elements, the

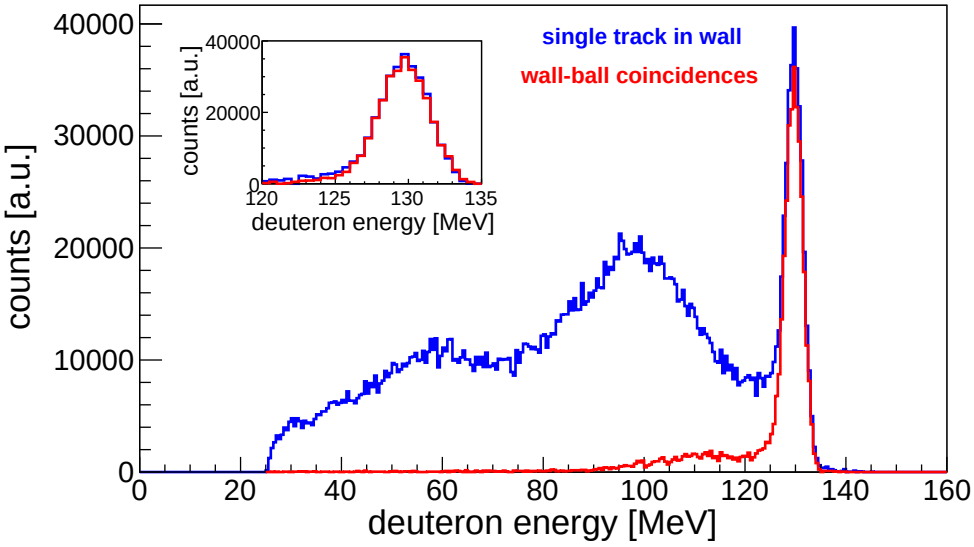

FIGURE 4.37: The same as Fig. 4.36 but for ball element 51 and the solid angle in wall (θ = 25±1°, ϕ = −53±5°)

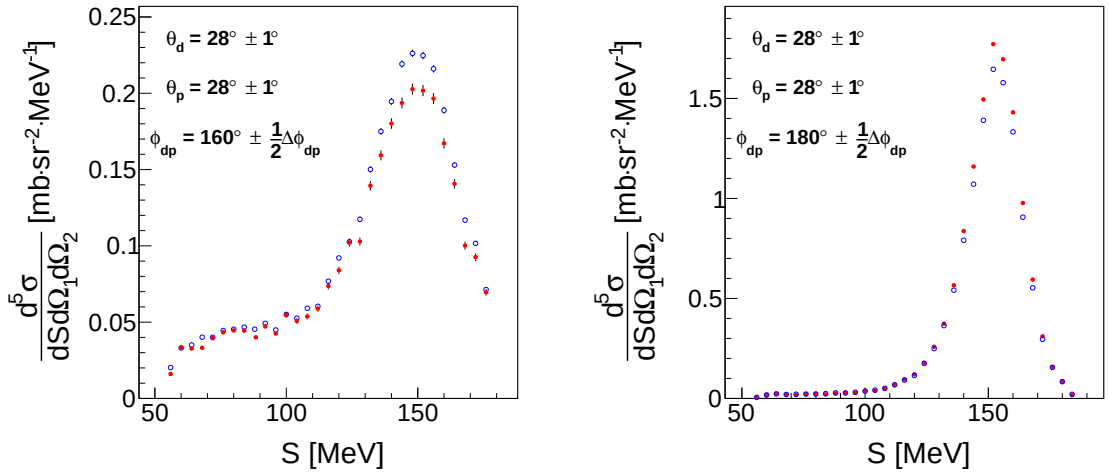

FIGURE 4.38: Comparisons of sample cross sections obtained with (a) regular bin size of $\Delta\phi_{dp} = 10°$ (blue), and (b) smaller bin size of $\Delta\phi_{dp} = 4°$ (red).

obtained spectra for two of which are presented in Fig. 4.36 and Fig. 4.37. Depending on the signal-to-background ratio observed in analysis of single track in wall, the number of events obtained in analysis of the wall-ball coincidences was by 1 to 10 % lower. As a results, the systematic uncertainty due to this effect on cross section was estimated to be about 5%.

5. Energy calibration

   The error in the calibration function can affect the shape and length of the S-curve which ultimately influences the height of the distribution cross section. The influence of this systematic effect on the final results is estimated by varying the calibration parameters and its found to be below 1%.

6. Averaging Problem

   The experimental cross section, for a given angular configuration (θ_d, θ_p, ϕ_{dp}), is evaluated by taking a finite bin width around these angles, i.e. $\theta_d \pm \frac{1}{2}\Delta\theta_d$, $\theta_p \pm \frac{1}{2}\Delta\theta_p$ and $\phi_{dp} \pm \frac{1}{2}\Delta\phi_{dp}$. The bin width is taken wide enough (here $\Delta\theta_d = \Delta\theta_p = 2°$ and $\Delta\phi_{dp}= 10°$) for the purpose of good statistical accuracy. On the other hand, the theoretical predictions, used for the comparison, are calculated at the central values of these angular bins. As explained in [83], one has to take the theoretical predictions averaged over the experimental bin width. The systematic effect associated with the averaging is related to the size of the angular bin width. For this work, the bin size of relative azimuthal angle, $\Delta\phi_{dp}= 10°$, was quite large (as compared to the bins in polar angles $\Delta\theta_d = \Delta\theta_p = 2°$). In order to estimate the associated systematic error, the analysis was repeated with smaller bin size $\Delta\phi_{dp}= 4°$. Comparisons of sample cross sections for the two different bin sizes, $\Delta\phi_{dp}= 4°$ and $\Delta\phi_{dp}= 10°$, are presented in Fig. 4.38. The systematic error associated with this effect, in most cases, was found up to 5%.

TABLE 4.1: Sources of systematic effects and their influence (in %) on the final results.

Source of uncertainty		**effect on the cross section [%]**
Particle identification		5.0
Absolute normalization	choice of scaling region (error in k_{scale})	2.9
	error quoted for BBS data	5.02
Reconstruction of angles		1.0
Background subtraction		5.0
Energy Calibration		1.0
Averaging Problem		5.0
Total		10.52

Chapter 5

Results and Discussion

In this chapter, the discussion of the experimental results and their comparison with the theoretical predictions are presented. To make a reliable comparison between data and theories usually one performs a χ^2 analysis. In this case, however, the calculations are only approximate, thus such an analysis would not be statistically meaningful. Therefore, to be able to conclude on the calculations quantitatively, the distance between each data point and corresponding theory point was calculated and normalized to the theory. The quantitative analysis was performed with respect to two variables: energy of the relative motion of the deuteron-proton pair (E_{rel}) and the neutron energy(E_n).

The results for the $dd \rightarrow dpn$ breakup reaction are presented in the form of five-fold differential cross section for 147 chosen angular configurations defined by θ_d, θ_p, ϕ_{dp}. The proton (θ_p) and the deuteron (θ_d) polar angles are changed with a step of 2°, in the range from 16° to 28°, resulting in total of 49 different combinations. Each of the combinations is studied for three different relative azimuthal angles ϕ_{dp}: 140°, 160° and 180°. The choice of the ϕ_{dp} angles is motivated by studies of the phase-space region dominated by dp-QFS. In this case the neutron acts as a spectator with its energy close to a minimum. The bin size for the polar angles was set to be $\Delta\theta_d$=$\Delta\theta_p$=2° and for the relative azimuthal angles $\Delta\phi_{dp}$=10°. The cross section distributions are presented as a function of a kinematical variable S. The corresponding bin size was chosen to be ΔS=4

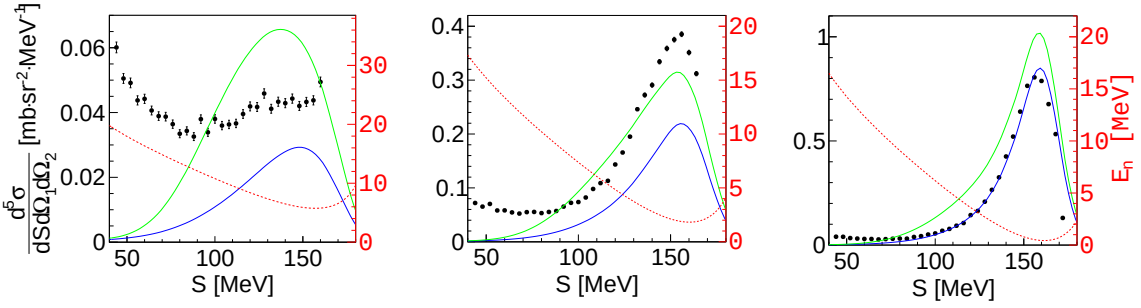

FIGURE 5.1: Sample cross section distributions obtained for 3 geometries characterized by the same combination of polar angles:(θ_d=22°, θ_p=20°) and three different ϕ_{dp} values: 140° (left), 160° (center) and 180° (right). The solid lines are for theoretical prediction — blue with 1-term calculations and green with 4-term calculations (see Section 2.2). The dashed-line and the right hand scale (both in red color) present the dependence of the spectator neutron energy (E_n) along S-axis.

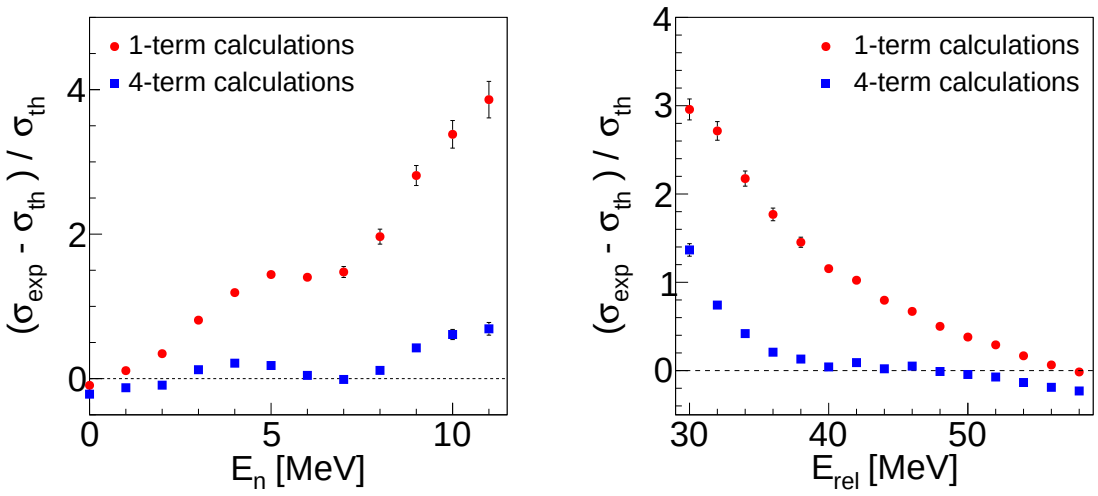

FIGURE 5.2: Relative discrepancies between the experimental data and the theoretical predictions of the breakup cross sections as a function of (a) the spectator neutron energy (left) and (b) relative energy of the deuteron and the proton (right).

MeV. These integration limits are wide enough to reach good statistical accuracy. For each configuration the data points are presented along with their statistical uncertainty.

Since the exact theoretical calculations are not yet available, the obtained results are compared with the ones (provided by A. Deltuva) based on the SSA, expected to be a rough estimate near QFS kinematics, i.e. so-called *one-term calculations* (1-term) and *four-term calculations* (4-term) (see Section 2.2). The spectator neutron energy is presented along with the cross-section distributions to have a feeling of how far the data points are from the QFS limit. Here it is worth to mention that the calculations are based on the non-relativistic framework and therefore the kinematical variable S has to be recalculated to the relativistic form. This was done simply by a projection of the kinematics used in the calculations onto the relativistic one.

Sample of the cross-section distributions obtained, for a chosen combination of polar angles ($\theta_d = 22°$, $\theta_p = 20°$) and for the three relative azimuthal angles is presented in Fig. 5.1. The whole set of cross-section results is presented in Appendix C.

The data are arranged in a way that for a given θ_d the full set of the cross section for all analyzed θ_p is presented. For the lower available $\theta_d = 16°$ and for the QFS configurations ($\phi_{dp} = 180°$), the agreement between the data and the 1-term calculations are visible at $\theta_p = 18°$. With the increasing value of θ_d, the agreement in case of the 1-term theory and the data appears at $\theta_p = 18°,\ 20°$, whereas for the 4-term ones it is seen only for $\theta_p = 22°$. A similar picture repeats also at the higher analyzed θ_d, up to 26°. For the $\theta_p = 28°$ the both kinds of the calculations give the same results, therefore one can estimate a difference between the calculations and the data according to increasing value of θ_d. As one can notice, the difference decrease and for the configuration of $\theta_d = 28°,\ \theta_p = 28°$ is about 3 times less than for $\theta_d = 16°,\ \theta_p = 28°$.

The discrepancies observed between the results and the theoretical calculations are rather large. However a relative difference between the data and theory, defined as $(\sigma_{exp}\text{-}\sigma_{th})/\sigma_{th}$, is calculated and presented as a function of (a) the spectator neutron

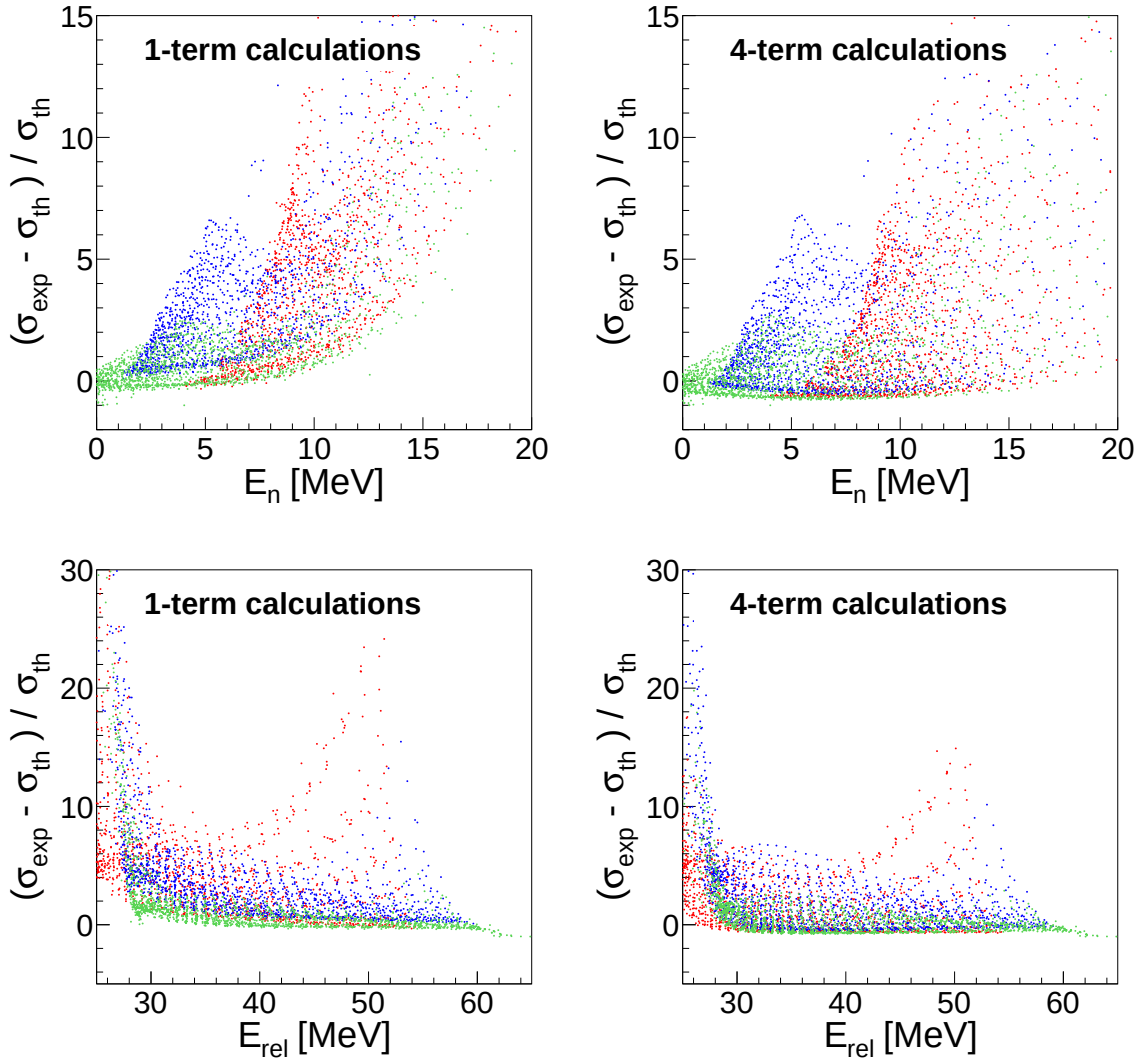

FIGURE 5.3: Similar to Fig. 5.2: except the relative discrepancies between the experimental data and the theoretical predictions are presented for individual data points. The data points for a given relative azimuthal angle are grouped in one color — $\phi_{dp} = 140°$ (red), $\phi_{dp} = 160°$ (blue) and $\phi_{dp} = 180°$ (green).

energy (E_n) and (b) the energy of relative motion of deuteron-proton pair (E_{rel}). Such a study allows one a quantitative verification of the calculations.

As expected, at very small E_n, both types of the calculations describe the data equally well. With the increasing values of E_n, the 4-term calculations relatively better describe the data. The same trend can be observed when presenting the individual data points grouped (different color) for a given ϕ_{dp}, see Fig. 5.3. Here, as one can see, the data-vs-theory is the best described for $\phi_{dp} = 180°$ and (as one moves away from QFS limit) worst for $\phi_{dp} = 140°$.

Based on the set of the cross section for individual configurations few conclusions can be drawn. The shape of the cross-section distributions for configurations with $\phi_{dp} = 160°$ and $180°$ is equally well reproduced by the calculations. However, due to relatively small values of the cross-section, it is difficult to conclude on the data for ϕ_{dp}=140°.

From the theoretical point of view, single-scattering approximation is expected to be more reliable when the spectator energy is small. In some cases, especially at $\phi_{dp} = 180°$, a reasonable agreement is seen. Furthermore, if 1- and 4-terms theories do not agree, this implies that other terms beyond the 1st one are important too. Therefore, more complicated picture should be considered in this situation, like interplay involving higher-order terms. Having only rough calculations, the approximation is more trust worthy when 1- and 4-term theories agree and in such cases the comparison with the data is reasonable. What is more, the higher-order terms are expected to be suppressed more when the neutron-deuteron and neutron-proton relative energies are larger, i.e., when the proton and the deuteron are scattered at larger θ with larger energies.

From the data side, one should also take into account a large systematic uncertainty associated with the absolute normalization. The discrepancy at the smallest E_{rel} values can be, on the other hand, attributed to the seizable contribution of the Coulomb force.

Chapter 6

Summary, Conclusion and Outlook

The aim of this work was to investigate the $^2H(d,dp)n$ breakup reaction near quasi- free scattering (QFS) kinematics, at which the spectator neutron energy (E_n) remains close to zero. The experiment was performed at the KVI Groningen facility. The deuteron beam at 160 MeV energy was provided by the AGOR cyclotron and was impinged on the liquid deuterium target. The reaction products were detected using the 4π BINA detection system. The set of the five-fold differential cross section $\frac{d^5\sigma}{d\Omega_1 d\Omega_1 dS}$ was obtained for 147 dp configurations. The results complement the database of 4N systems with about 4500 new data points. In addition, the data collected with the backward part of BINA (ball) were for the first time analyzed extensively. The most significant steps in the data analysis were the introduction of the cluster based angular and energy information into the charged particles track reconstruction and the ball calibration.

The cross-section results have been compared to the very first theoretical calculations using single-scattering approximation (SSA) based on the CDBonn+Δ potential, provided by A. Deltuva. Despite the fact that the energy at which the experiment was carried out was not high enough for SSA, the approximate calculations describe the data fairly well and for a few configurations satisfactory agreement have been achieved. Both, the 1-term and the 4-term calculations, reproduce the data well at lowest E_n. As the E_n increases, the discrepancy between 1-term calculation and the data becomes larger compared to the one based on the 4-term. This behavior is quite obvious since the 4-term calculations include more dynamical terms. In general, the data are described better by the theory at ϕ_{dp}=180° and worst for the lower studied values of ϕ_{dp}. Moreover, as one moves to the larger values of θ_d , the discrepancy between both, 1-term and 4-term, calculations decreases what indicates that the additional part of the dynamics which contributes to the QFS state is less important and in such cases, the agreement is improved.

The strategy developed for trajectory and energy reconstruction in the ball will certainly be useful for exploring the region of larger scattering angles. Moreover, the data analysis can be extended to other channels in dd scattering. One may study for example the transfer channels which have already been identified and shown or the double quasi-free process within four-body breakup $dd \rightarrow ppnn$, where both neutrons are acting as spectators. The results obtained are very important for the future theoretical studies of the 4N systems dynamics, serving as a verification tool for the calculations currently being developed which are entering in a new step of the advancement.

Appendix A

List of ball elements

The backward ball of BINA has 149 phoswich elements as explained in the Chapter 3. The table below provides list of first 55 ball elements, each with list of it's neighbor elements and angular information about their geometrical centers. With a triangular shape, each elements has maximum 12 neighbors — 3 elements from three sides (s_i, where i=1,2,3) and 9 elements from three vertexes (v_j, where j=1,2,..,9) — each vertex with three neighbors. There is exception for an element, placed at an edge of gaps (the target-holder entrance, the beam-pipe entrance, the forward window opening), will have less than 12 neighbors.

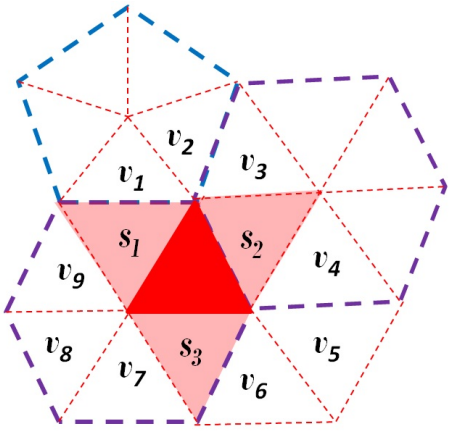

FIGURE A.1: Ball element neighbors. See the text for the details.

During the analysis, the vertex neighbors can be switched off or on. In present work we used only the nearest neighbors, this is because the inclusion of neighbors-of-neighbor didn't have any notable influence on the results.

Table A.1: A table listing all the ball elements BINA's backward ball — each with it's centroid angles (ϕ and θ) and it's neighbor elements. The first column represents the elements number, the second and third columns are the angles. Rest of the columns represent neighbor elements (see the text for detail).

ball nr.	**angles [degree]**		**neighbors**											
			on sides			**on vertexes**								
(#)	ϕ	θ	s_1	s_2	s_3	v_1	v_2	v_3	v_4	v_5	v_6	v_7	v_8	v_9
1	71.25	45.0	2	25	—	3	23	24	26	27	55	—	—	—
2	54.0	50.0	1	3	27	4	25	26	28	29	55	—	—	—
3	36.75	45.0	2	4	—	1	5	6	27	28	29	—	—	—
4	25.75	53.5	3	5	29	2	6	27	28	30	31	—	—	—
5	10.25	53.5	4	6	31	3	7	29	30	32	33	—	—	—
6	359.25	45.0	5	7	—	3	4	8	31	32	33	—	—	—
7	342.0	50.0	6	8	33	5	9	31	32	34	35	—	—	—
8	324.75	45.0	7	9	—	6	10	11	33	34	35	—	—	—
9	313.75	53.5	8	10	35	7	11	33	34	36	37	—	—	—
10	298.25	53.5	9	11	37	8	12	35	36	38	39	—	—	—
11	287.25	45.0	10	12	—	8	9	13	37	38	39	—	—	—
12	270.0	50.0	11	13	39	10	14	40	41	37	38	—	—	—
13	252.75	45.0	12	14	—	11	15	16	39	40	41	—	—	—
14	241.75	53.5	13	15	41	16	42	43	12	39	40	—	—	—
15	226.25	53.5	14	16	43	13	44	45	17	41	42	—	—	—
16	215.25	45.0	15	17	—	13	14	43	44	45	18	—	—	—
17	198.0	50.0	16	18	45	46	47	19	15	43	44	—	—	—
18	180.75	45.0	17	19	—	16	20	21	45	46	47	—	—	—
19	169.75	53.5	18	20	47	21	48	49	17	45	46	—	—	—
20	154.25	53.5	19	21	49	18	50	51	22	47	48	—	—	—
21	143.25	45.0	20	22	—	18	19	23	49	50	51	—	—	—
22	126.0	50.0	21	23	51	52	53	24	20	49	50	—	—	—

Continued on next page

Table A.1 – *Continued from previous page*

ball nr. (#)	angles [degree]		neighbors											
			on sides			on vertexes								
	ϕ	θ	s_1	s_2	s_3	v_1	v_2	v_3	v_4	v_5	v_6	v_7	v_8	v_9
23	108.75	45.0	22	24	—	21	51	52	53	25	1	—	—	—
24	97.75	53.5	23	25	53	1	54	55	51	52	22	—	—	—
25	82.25	53.5	24	1	55	23	26	27	2	53	54	—	—	—
26	67.0	73.5	1	27	56	25	1	2	57	58	28	54	—	—
27	54.0	65.25	26	28	2	1	25	55	3	4	29	56	57	58
28	41.0	73.5	27	29	58	2	3	4	59	60	30	26	56	57
29	36.5	67.5	28	30	4	27	2	3	5	31	58	59	60	—
30	18.0	75.25	29	31	60	4	5	28	58	59	61	62	32	—
31	0.5	67.5	30	32	5	6	7	33	60	61	62	4	29	—
32	355.0	73.5	31	33	62	5	6	7	63	64	34	30	60	61
33	342.0	65.25	32	34	7	5	6	31	8	9	35	62	63	64
34	329.0	73.5	33	35	64	7	8	9	65	66	36	32	62	63
35	324.5	67.5	34	36	9	33	7	8	10	37	64	65	66	—
36	306.0	75.25	35	37	66	9	10	67	68	38	34	64	65	—
37	287.5	67.5	36	38	10	9	35	11	12	39	66	67	68	—
38	283.0	73.5	37	39	68	10	11	12	69	70	40	36	66	67
39	270.0	65.25	38	40	12	10	11	37	13	14	41	68	69	70
40	257.0	73.5	39	41	70	12	13	14	71	72	42	38	68	69
41	252.5	67.5	40	42	14	39	12	13	43	15	70	71	72	—
42	234.0	75.25	41	43	72	40	70	71	14	15	73	74	44	—
43	215.5	67.5	42	44	15	16	17	45	72	73	74	14	41	—
44	211.0	73.5	43	45	74	15	16	17	75	76	46	42	72	73
45	198.0	65.25	44	46	17	15	46	43	18	19	47	74	75	76
46	185.0	73.5	45	47	76	17	18	19	77	78	48	44	74	75
47	180.5	67.5	46	48	19	45	17	18	49	20	76	77	78	—
48	162.0	75.25	47	49	78	19	20	79	80	50	46	76	77	—

Continued on next page

Table A.1 – *Continued from previous page*

ball nr.	**angles [degree]**		**neighbors**											
			on sides			**on vertexes**								
(#)	ϕ	θ	s_1	s_2	s_3	v_1	v_2	v_3	v_4	v_5	v_6	v_7	v_8	v_9
49	143.5	67.5	48	50	20	47	19	78	79	80	21	22	51	—
50	139.5	73.5	49	51	80	20	21	22	81	82	52	48	78	79
51	126.0	65.25	50	52	22	49	20	21	23	24	53	80	81	82
52	113.0	73.5	51	53	82	50	80	81	54	22	23	24	—	—
53	108.5	67.5	52	54	24	25	55	82	51	22	23	—	—	—
54	90.0	75.25	53	55	—	24	25	26	56	52	82	—	—	—
55	71.5	67.5	54	25	26	53	24	25	1	2	27	56	—	—

Appendix B

Formula for differential cross section

The differential elastic scattering cross section can be given as follows:

$$\frac{d\sigma_{el}}{d\Omega_d}(\Omega_d^{el}) = \frac{1}{n(1-\tau)N_0\Delta x} \cdot \frac{N_{el}(\Omega_d^{el})}{\Delta\Omega_d^{el}} \cdot \frac{1}{\epsilon^{el}(\Omega_d^{el})\epsilon^{el,ball}(\Omega_d^{el,ball})} \tag{B.1}$$

where,
n = density of the interaction centers in the target,
$(1-\tau)$ = elcronic live-time (fraction of time when the DAQ is active to accept events),
N_0 = collected charge in the FC (in the units of elementary charge e),
Δx = target thickness,
N_{el} = counts of the elastically scattering deuterons registered in the solid angle Ω_d^{el},
$\epsilon^{el}(\Omega_d^{el})$ = total detector efficiency for deuteron in the wall,
$\epsilon^{el,ball}(\Omega_d^{el,ball})$ = total detector efficiency for deuteron in the ball. For the case of the single track elastic events in wall, $\epsilon^{el,ball}(\Omega_d^{el,ball}) = 1$. In case of the three body breakup process, the diff. breakup cross section is given as follows:

$$\frac{d^5\sigma}{d\Omega_d d\Omega_p dS}(S, \Omega_d, \Omega_p) = \frac{1}{n(1-\tau)N_0\Delta x} \cdot \frac{N_{br}(S, \Omega_d, \Omega_p)}{\Delta\Omega_d\Delta\Omega_p\Delta S} \cdot \frac{1}{\epsilon(\Omega_d)\epsilon(\Omega_p)} \tag{B.2}$$

where,
N_{br} = counts of the deuteron-proton coincidences from the three-body breakup process registered at solid angles Ω_d, Ω_p and projected onto a ΔS-wide arc-length bin,
$\epsilon(\Omega_i)$ = total detector efficiencies for the breakup particles in the wall (subscript i stands for d or p.).

Appendix C

Breakup Cross Section Results

Please go to the next page.

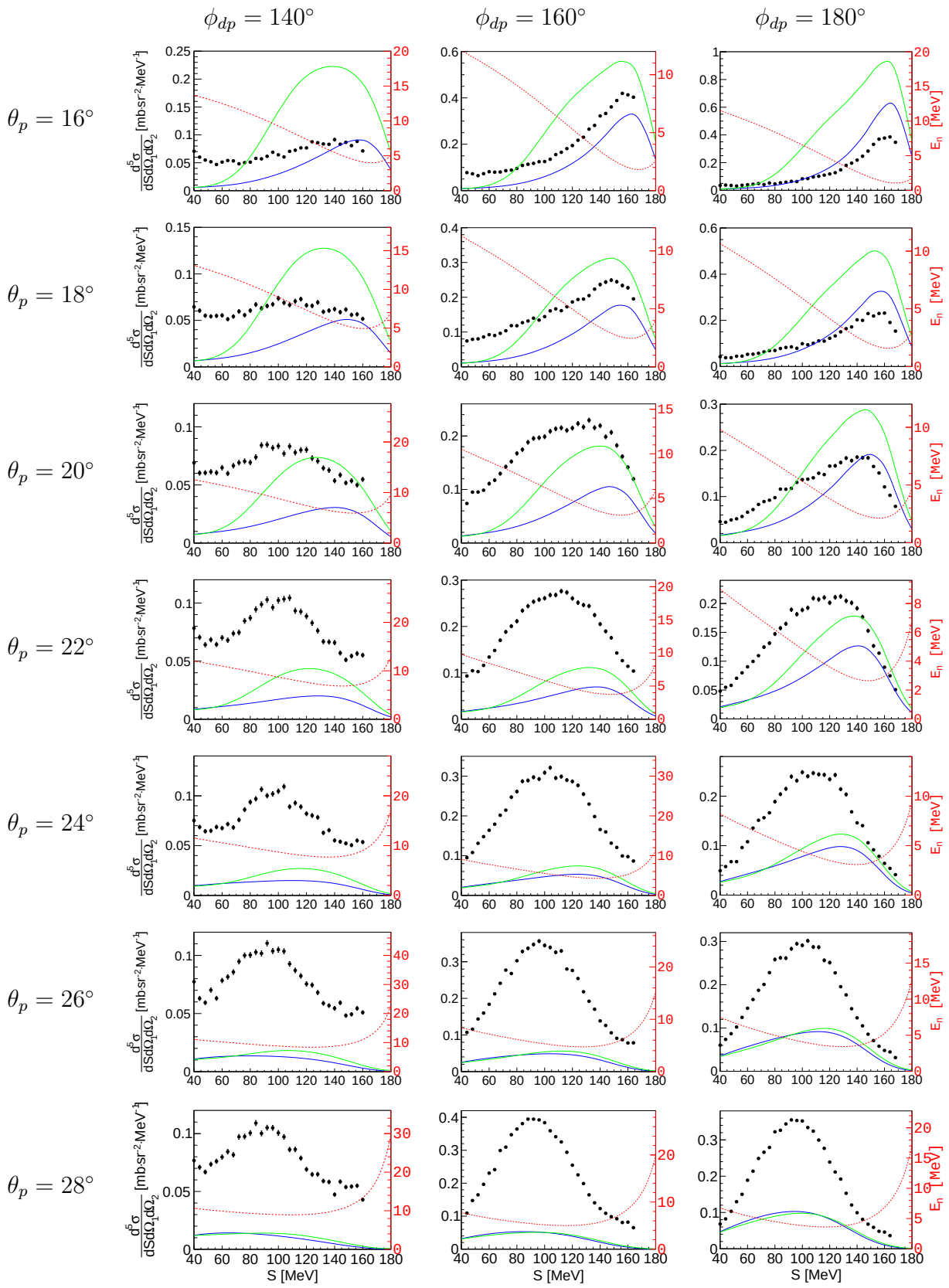

FIGURE C.1: Results at $\theta_d = 16°$ for different ϕ_{dp} (columns) and different θ_p (rows). The solid lines are for theoretical prediction — blue with 1-term calculations and green with 4-term calculations (see Section 2.2). The dashed-line and the right hand scale (both in red color) present the dependence of the spectator neutron energy (E_n) along S-axis.

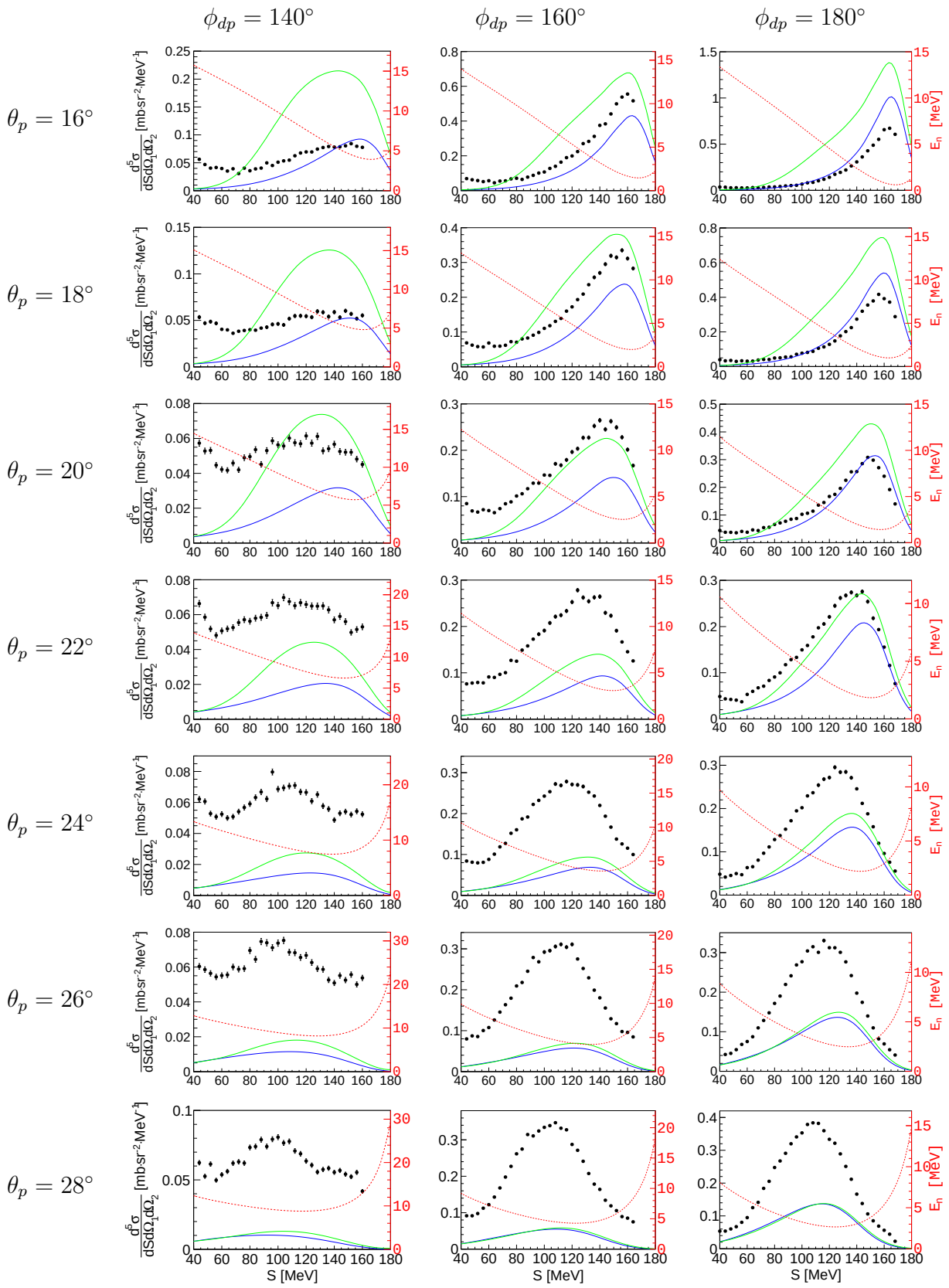

FIGURE C.2: The same as Fig.C.1, except for $\theta_d = 18°$.

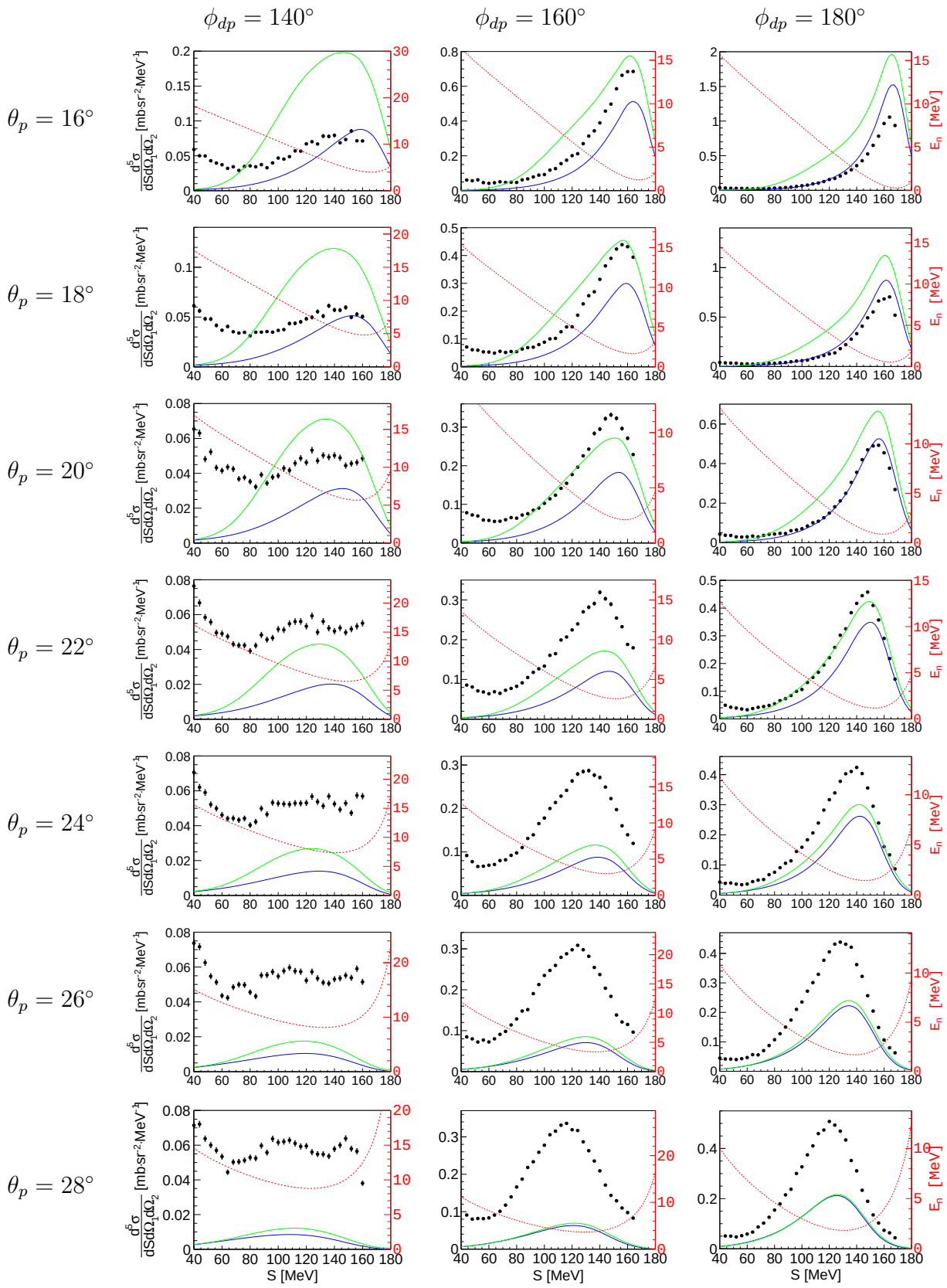

FIGURE C.3: The same as Fig.C.1, except for $\theta_d = 20°$.

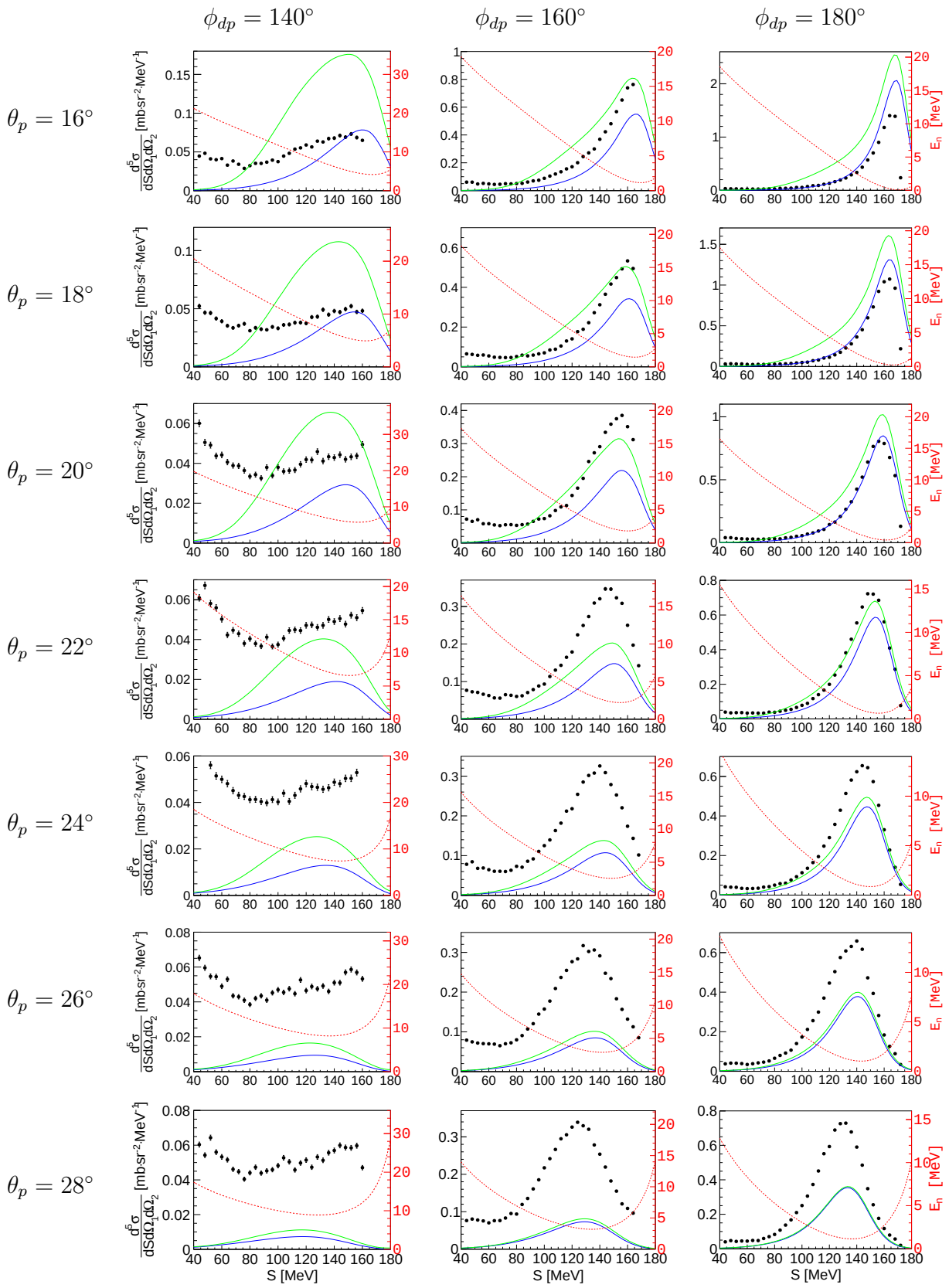

FIGURE C.4: The same as Fig.C.1, except for $\theta_d = 22°$.

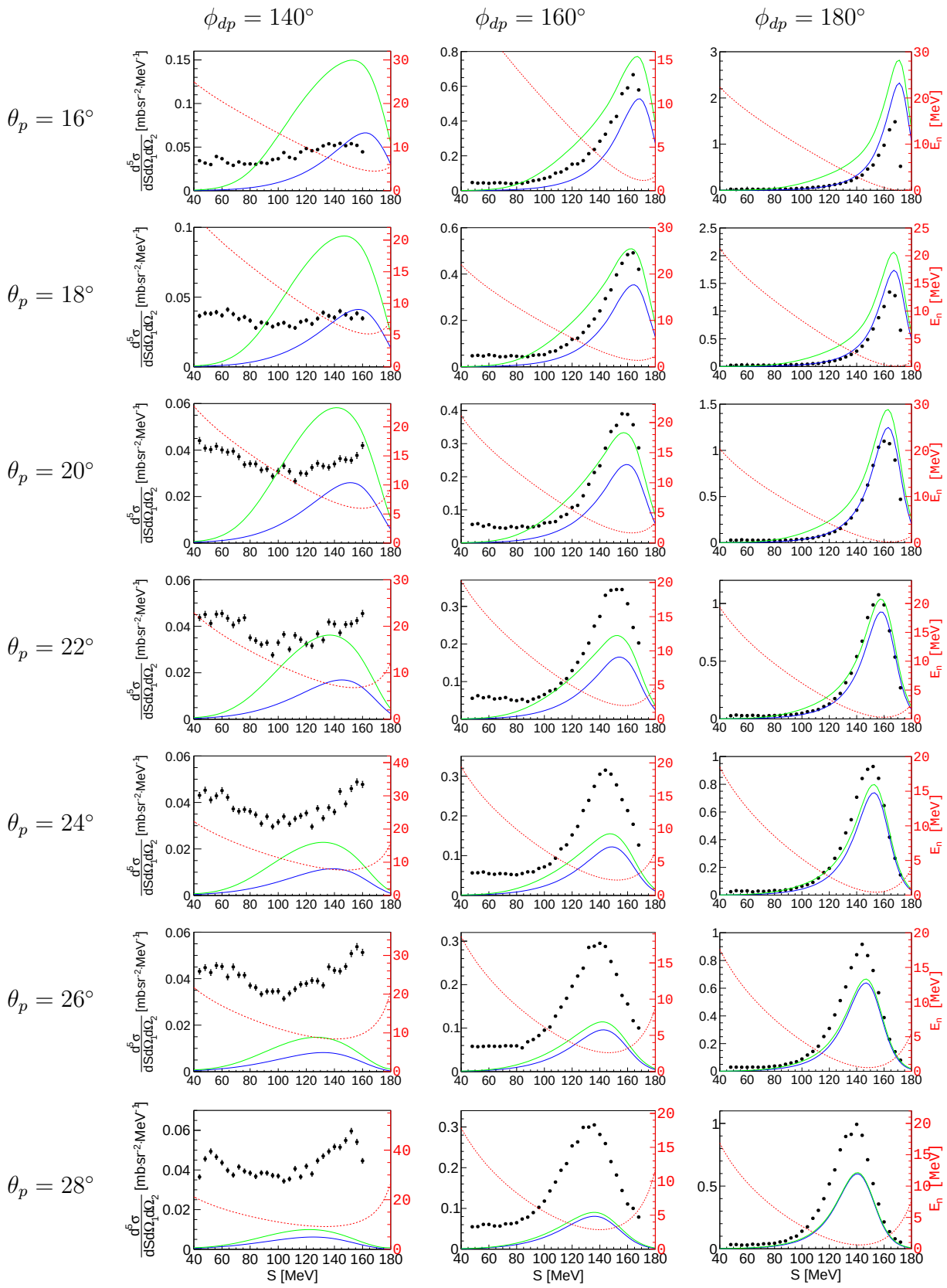

FIGURE C.5: The same as Fig.C.1, except for $\theta_d = 24°$.

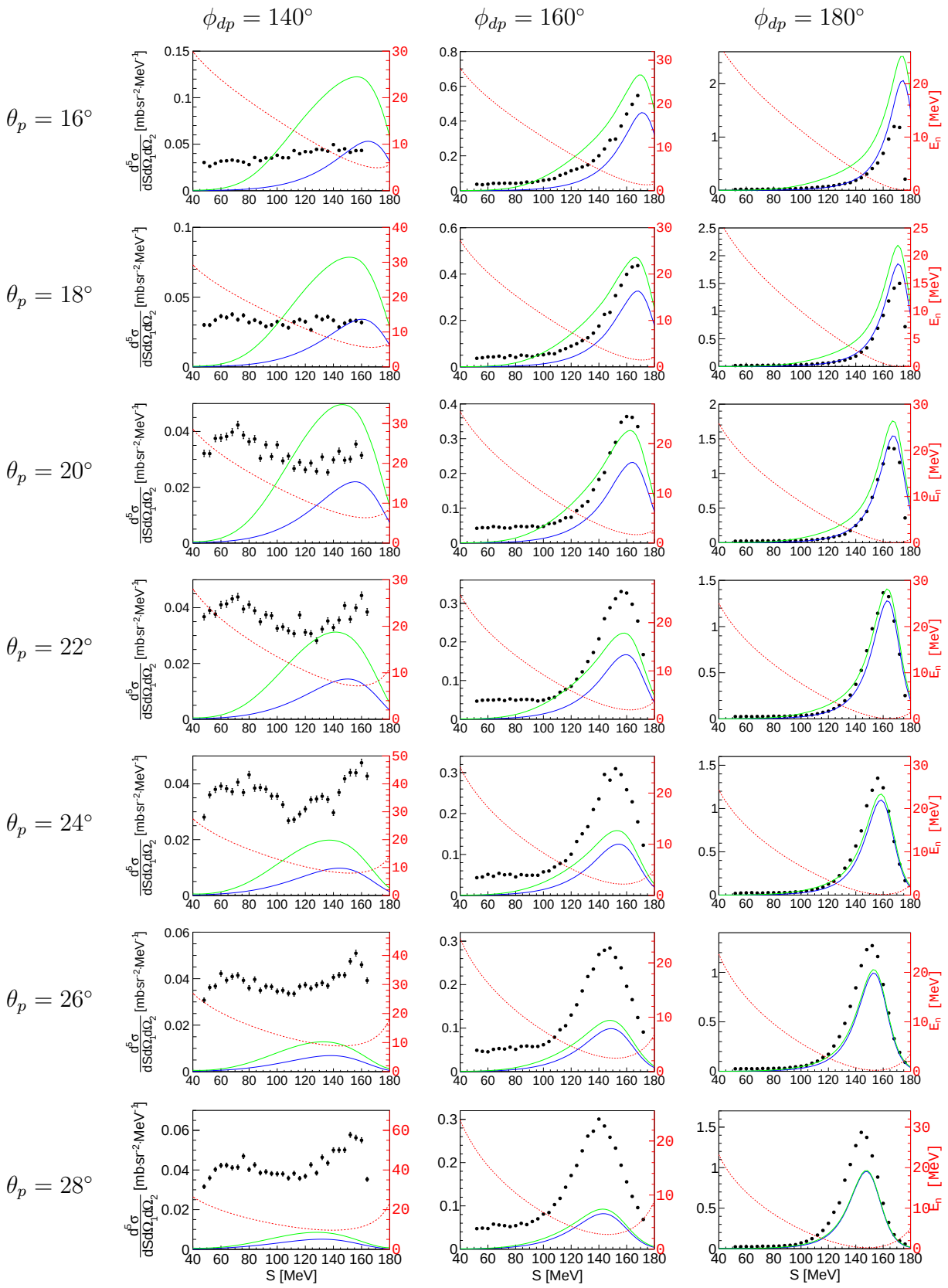

FIGURE C.6: The same as Fig.C.1, except for $\theta_d = 26°$.

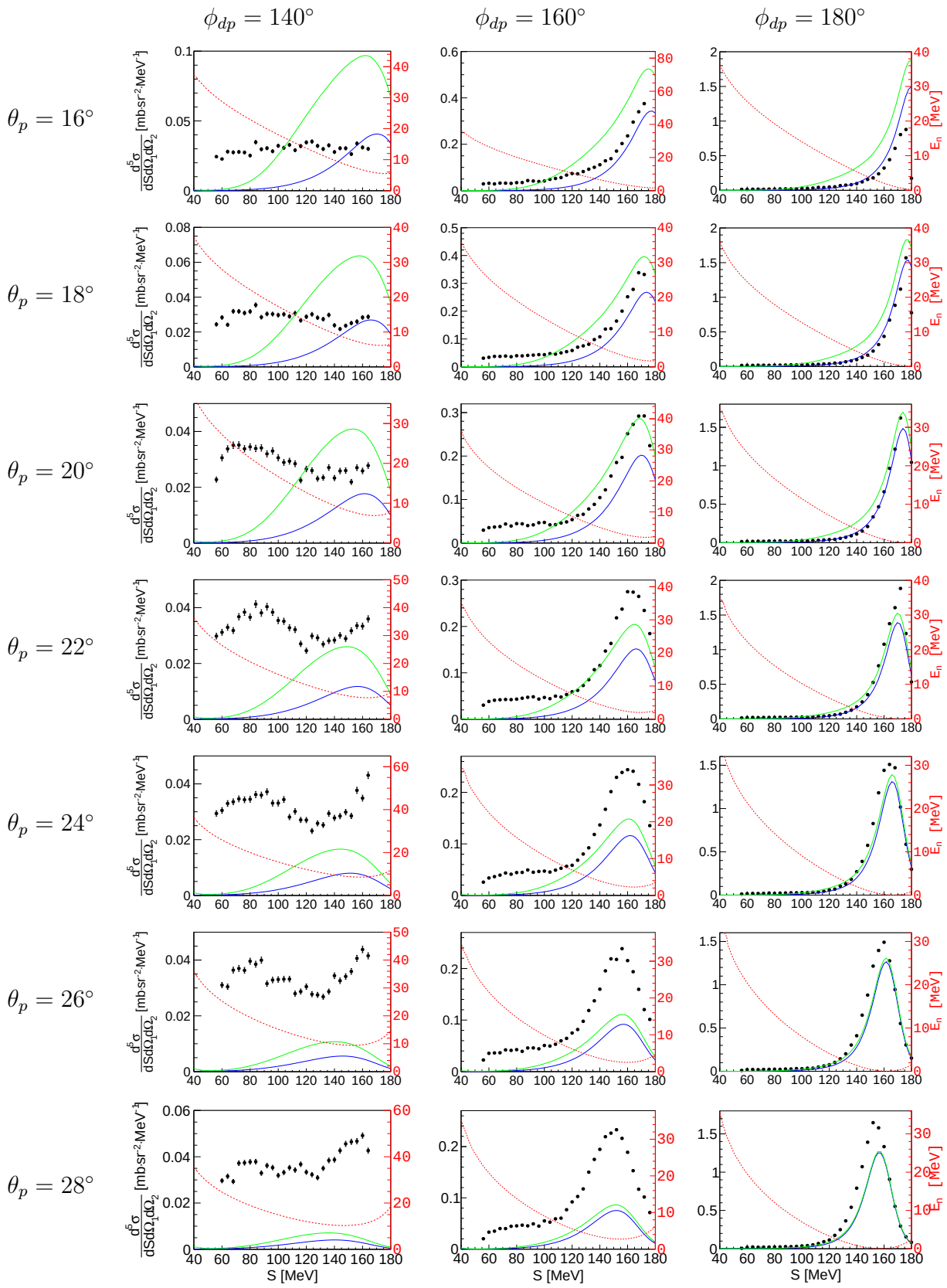

FIGURE C.7: The same as Fig.C.1, except for $\theta_d = 28°$.

Bibliography

[1] H. Yukawa, Proc. Phys. -Math. Soc. Japan **17**, 48 (1935).

[2] H. J. Bhabha, Nature **143**, 276 (1939).

[3] G. Occhialini and C. Powell, Nature (1947).

[4] M. Taketani, S. Nakamura, and M. Sasaki, Progress of Theoretical Physics **6**, (1951).

[5] V. Stoks, R. Klomp, C. Terheggen, and J. D. Swart, Physical Review C **49**, 2950 (1994).

[6] R. Wiringa, V. Stoks, and R. Schiavilla, Physical Review C **51**, 38 (1995).

[7] R. Machleidt, F. Sammarruca, and Y. Song, Physical review C: Nuclear physics **53**, R1483 (1996).

[8] H. Witala *et al.*, Physical Review Letters **81**, 11 (1998).

[9] S. Pieper, V. Pandharipande, and R. Wiringa, Physical Review C **64**, 1 (2001).

[10] E. Epelbaoum, W. Glöckle, and U.-G. Meißner, Nuclear Physics A **637**, 107 (1998).

[11] E. Epelbaoum, W. Glöckle, A. Krüger, and U.-G. Meißner, Nuclear Physics A **645**, 413 (1999).

[12] J.-I. Fujita and H. Miyazawa, Progress of Theoretical Physics **17**, 360 (1957).

[13] E. Stephenson *et al.*, Physical Review C **60**, 3 (1999).

[14] R. Bieber, Physical Review letters **84**, 606 (2000).

[15] H. Sakai, Physical Review letters **84**, 5288 (2000).

[16] K. Sekiguchi *et al.*, Physical Review C **65**, 34003 (2002).

[17] K. Ermisch, Physical Review C **68**, 1 (2003).

[18] S. Kistryn *et al.*, Physical Review C **68**, 1 (2003).

[19] K. Sekiguchi, Physical Review C **70**, 1 (2004).

[20] S. Kistryn, Physical Review C **72**, 1 (2005).

[21] K. Ermisch, Physical Review C **71**, 1 (2005).

[22] S. Kistryn, Physics Letters B **641**, 23 (2006).

[23] B. v. Przewoski *et al.*, Physical Review C **74**, 1 (2006).

[24] E. Stephan, Physical Review C **76**, 21 (2007).

[25] H. Mardanpour *et al.*, European Physical Journal A **31**, 383 (2007).

[26] H. Amir-Ahmadi, Physical Review C **75**, 1 (2007).

[27] A. Ramazani-Moghaddam-Arani, Physical Review C **78**, 014006 (2008).

[28] I. Ciepał *et al.*, Physical Review C **85**, 17001 (2012).

[29] N. Kalantar-Nayestanaki, Reports on Progress in Physics **75**, 016301 (2012).

[30] S. Kistryn and E. Stephan, Journal of Physics G: Nuclear and Particle Physics **40**, 63101 (2013).

[31] E. Stephan, S. Kistryn, and N. Kalantar-Nayestanaki, Few-Body Systems **55**, 627 (2014).

[32] J. W. Holt, N. Kaiser, and W. Weise, Progress in Particle and Nuclear Physics **73**, 35 (2013).

[33] H. Witała and W. Glöckle, Journal of Physics G: Nuclear and Particle Physics **37**, 064003 (2010).

[34] K. Sagara, Few-Body Systems **48**, 59 (2010).

[35] H. Witała, J. Golak, W. Glöckle, and H. Kamada, Physical Review C **71**, 1 (2005).

[36] H. Witała *et al.*, Physical Review C **77**, 034004 (2008).

[37] B. Kłos *et al.*, EPJ Web of Conferences **66**, 5 (2014).

[38] I. Ciepał *et al.*, Acta Physica Polonica B **46**, 459 (2015).

[39] A. Micherdzińska *et al.*, Physical Review C **75**, 54001 (2007).

[40] C. Bailey, PhD Thesis, Indiana University, U.S.A. (2009).

[41] A. Ramazani-Moghaddam-Arani, PhD Thesis, University of Groningen, The Netherlands (2009).

[42] C. Alderliesten and A. Djaloeis, Physical Review C **18**, (1978).

[43] V. Bechtold *et al.*, Nuclear Physics A **288**, 189 (1977).

[44] A. Ramazani-Moghaddam-Arani, Physical Review C **83**, 024002 (2011).

[45] W. Glöckle, The Quantum Mechanical Few-Body Problem - Texts and Monographs in Physics, Springer-Verlag, 1983.

[46] L. D. Faddeev, Sov. Phys. JETP **12**, 1014 (1961).

[47] A. M. Mukhamedzhanov, V. Eremenko, and a. I. Sattarov, Physical Review C - Nuclear Physics **86**, (2012).

[48] C. Elster, Lecture notes - chapter 1, The Nucleon-Nucleon System (Winter 1999: Phys 755: Nuclear Theory) (1999).

[49] W. Glöckle, Nuclear Physics A **41**, 620 (1970).

[50] W. Glöckle *et al.*, Physics Reports **274**, 107 (1996).

[51] B. S. Pudliner *et al.*, Physical Review C **56**, 75 (1997).

[52] R. B. Wiringa, Nucleon-Nucleon Interactions: Contemporary Nuclear Shell Models, 1997.

[53] J. Carlson and R. Schiavilla, Reviews of Modern Physics **70**, 743 (1998).

[54] E. Epelbaum, Physical Review C **66**, 1 (2002).

[55] E. Epelbaum, W. Glöckle, and U.-G. Meißner, Nuclear Physics A **747**, 362 (2005).

[56] E. Epelbaum, Progress in Particle and Nuclear Physics **57**, 654 (2006).

[57] E. Epelbaum, Reviews of Modern Physics **81**, 1773 (2009).

[58] A. Deltuva, R. Machleidt, and P. Sauer, Physical Review C **68**, 1 (2003).

[59] A. Deltuva, A. Fonseca, and P. Sauer, Physical Review C **73**, 3 (2006).

[60] O. A. Yakubovsky, Sov. J. Nucl. Phys. **5**, 937 (1967).

[61] A. Deltuva, Few-Body Systems **55**, 621 (2013).

[62] A. Deltuva and A. C. Fonseca, Physical Review Letters **113**, 102502 (2014).

[63] A. Deltuva and A. C. Fonseca, Physical Review C **90**, 044002 (2014).

[64] A. Deltuva and A. Fonseca, Physics Letters B **742**, 285 (2015).

[65] A. Deltuva, Private communication (2015).

[66] O. O. Beliuskina *et al.*, Problems of Atomic Science and Technology 162 (2013).

[67] G. Ohlsen, Nuclear Instruments and Methods **37**, 240 (1965).

[68] A. Ramazani-Moghaddam-Arani *et al.*, Physics Letters B **725**, 282 (2013).

[69] H. Mardanpour-Mollalar, PhD Thesis, University of Groningen, The Netherlands (2008).

[70] N. Kalantar-Nayestanaki *et al.*, Nuclear Instruments and Methods in Physics Research A **444**, 591 (2000).

[71] S. Gales, Proc. 11-th Conference on Cyclotrons and their Applications (lonies, Tokyo,) (1987).

[72] M. Volkerts *et al.*, Nuclear Instruments and Methods in Physics Research Section A **428**, 432 (1999).

[73] J. J. Benedetto and M. Fickus, Advances in Computational Mathematics **18**, 357 (2003).

[74] E. Stephan, Habilitation Thesis, University of Silesia, Katowice, Poland (2010).

[75] N. Kalantar-Nayestanaki, J. Mulder, and J. Zijlstra, Nuclear Instruments and Methods in Physics Research Section A **417**, 215 (1998).

[76] W. Parol *et al.*, Acta Physica Polonica B **45**, 527 (2014).

[77] A. Micherdzinska, PhD Thesis, University of Silesia, Katowice, Poland (2003).

[78] A. Biegun, PhD Thesis, University of Silesia, Katowice, Poland (2005).

[79] W. Parol, PhD Thesis, Jagiellonian University, Cracow, Poland (2015).

[80] J. B. Birks, The specific fluorescence of anthracene and other organicmaterials, 1951.

[81] Saint-gobain, Saint Gobain: Plastic Scintillators Data Sheet, 2015.

[82] C. Ryan *et al.*, Nuclear Instruments and Methods in Physics Research Section B **34**, 396 (1988).

[83] I. Ciepał, PhD Thesis, Jagiellonian University, Cracow, Poland (2010).

Acknowledgements

I would like to thank to all the people who have helped me at small and big level to complete this thesis.

Foremost, I would like to express my sincere gratitude to my promoter **Prof. Stanisław Kistryn** for giving me this opportunity. I truly appreciate the help and support I got from you even though you, being as a prorector, had bigger responsibilities. You made me capable of be an independent researcher and encouraged me to participate in various (inter)national scientific events so that I could learn more and develop my scientific career.

I am extremely thankful to my co-promotor **Dr. Izabela Ciepał**, and to my colleagues **Dr. Elżbieta Stephan** and **Dr. Adam Kozela** for their active input in every aspects of my thesis. Your guidance and help through the data analysis and writing of the thesis was truly a biggest support. Without you three folks, I wouldn't have kept my thesis well on track while maintaining a good quality, how can I ever possibly thank you. Your help means world to me.

My special thanks go to **Prof. Paweł Moskal** and his family, for the kindness and warm welcoming that you showed me. You took care of my stay in Poland so well that I felt like a home away from my home. There are no words to show you my appreciation in a true sense for so many things you did for me.

I would like to express my gratitude to the head of the Nuclear Physics Department, **Prof. Bugusław Kamys**, for his crucial support. Your wise advises saved me from many bureaucratic and administrative hurdles.

This work would not have been possible without endless support of the people and the AGOR cyclotron team at KVI, the Netherlands. Thank you so much **Prof. Nasser kalantar-Nayestanaki** and **Dr. Johan Meschendorp**. Thank you Nasser also for taking care of my stay in Groningen. I also thank to **Harry Timersma** and **Rob Kremers** for their precious and peculiar technical support. My sincere thanks also to the entire experimental team; **Prof. Kazimierz Bodek**, **Dr. Jacek Zejma**, **Dr. Barbara Kłos**, **Dr. Indranil Mazumdar**, **Dr. Izabela Skwira-Chalot**, **Dr. Alexandra Wrońska** and **Wiktor Parol**. Wiktor, thanks a lot also for your co-operation and help with analysis codes.

I would also like to thank to...

... the theory group of Lisbon, **Dr. Arnas Deltuva** and **Prof. Antonio C. Fonsceca** for taking care of my stay in Lisbon and providing me the theoretical calculations.

... the theory group at my Department; **Prof. Henryk Witała**, **Prof. Jacek Golak** and **Dr. Roman Skibiński** for their support.

... the rest of the faculty members and staff of the Nuclear Physics Department, who have been very kind and helpful to me; **Prof. Jarczyk**, **Prof. Władysław Waluś**, **Prof. Reinhard Kulessa**, **Prof. Andrzej Magiera**, **Prof. Piotr Salabura**, **Prof. Zbigniew Rudy**, **Prof. Jerzy Smyrski**. This paragraph is incomplete without mentioning administration support of **Mrs. Alicja Mysłek**, **Mrs. Agnieszka Wach** and **Mrs. Teresa Gucwa - Ryś**, thank you so much.

... my colleagues for their supports; **Eryk, Wojciech (C+++++), Marcin, Witold, Kacper, Magda, Iryna, Sushil, Jinesh, Tomek, Tomasz, Szymon, Ewelina, Anna, Ayeh, Yasir, Aladin, Jacek, Jan, Andrzej, Damian, Greg, Wiktor**.

... the team at the WASA-at-COSY facility; **Prof. James Ritman, Prof. Frank Goldenbaum** and **Dr. Volker Hejny** for taking care of my stay in Juelich. And how can I miss to thank my dear friend Slava at FZJ - Juelich.

... **Prof. Krzysztof Rusek**, **Prof. Ismael Martel** and **Prof. Kirby Kemper** for their teachings and support at various events, in particular at the HIL workshop.

... **Prof. Giuseppina Orlandini**, **Prof. Alejandro Kievsky**, **Prof. Nir Barnea**, **Dr. Andreas Nogga**, **Dr. Rimantas Lazauskas** and **Dr. Mario Gattobigio** for their fruitful discussions and teachings on theoretical aspects of few-nucleon interactions.

... people at IFJ PAN; **Prof. Adam Maj, Prof. Paweł Olko, Dr. Jan Swakon, Prof. Antoni Szczurek** and **Prof. Jan Styczek** for their friendly interactions during my presence at IFJ.

... **Prof. Edward Stephenson** and **Dr. Crystal Bailey** for sharing their results so that I could scale the elastic scattering cross-section presented in this work.

... **Mgr Krzysztof Byrski** and prorector **Prof. Andrzej Mania** for helping me with my accommodation in Krakow.

... my former college teachers **Dr. Pruthul Desai**, **Dr. Ashok Mody**, **Dr. Ashwin Patel**, **Anil Bhatt sir** and the staff of Navyug Science college, without your support I wouldn't reach to the present stage to achieve this success.

... my dear friends/colleagues from India/abroad for the their direct/indirect support, thank you **Prof. Per Brunsel, Prof. Guido van Oost, Prof. Gerard Bonhomme, Frank Janssens, Jay Mody, Divya Kurup, Alok, Bhavesh (sallu), Nilanjan, Amol, Alen, Leana, Fra, friends from Amreli's Khatri boarding**.

... my polish friends **Angelika (carla), Emi, Nadzeja, Malika**, team of **AZS AWF KRAKÓW MASTERS**, friends from **żaczek dormitory** ...(list goes on)

We acknowledge support by the **Foundation for Polish Science - MPD program, co-financed by the European Union within the European Regional Development Fund**.

Last but not least, I appreciate very much the love, support and most importantly patience of **my family**; parents Ravi and Kusum, sisters Apla and Nita, brother Dipu, and my girlfriend (now wife) Jagoda. Words are not enough to thank you **Jagoda** for the support and motivation you gave during the most crucial last year of my PhD.